DOCTOR OF PHILOSOPHY

Hydrodynamic processes and their impacts on the mud deposit in the Southern Yellow Sea, China

Zhou, Chun-Yan

Award date:
2014

DOCTOR OF PHILOSOPHY

Hydrodynamic processes and their impacts on the mud deposit in the Southern Yellow Sea, China

Chun-Yan Zhou

2014

University of Dundee

Hydrodynamic Processes and Their Impacts on the Mud Deposit in the Southern Yellow Sea, China

Chunyan Zhou

A thesis submitted for the degree of Doctor of Philosophy

Division of Civil Engineering

The University of Dundee

January 2014

TABLE OF CONTENTS

List of figures

List of table

Notation

a_0	Constant depending upon the bed properties(consolidation, bulk density,ect)
A	Amplitude of the wave oscillation on the bottom
A_H	horizontal viscosity coefficient
A_v	Vertical viscosity coefficients
b	Buoyancy
C	Suspended sediment concentration
C_D	Wind drag coefficient
C_p	Specific heat capacity constant-pressure
c_x	Wave propagation velocity in the x direction
c_y	Wave propagation velocity in the y direction
c_σ	Wave propagation velocity in spectral space σ
c_Φ	Wave propagation velocity in spectral space Φ
D	Sediment deposition flux
d_{50}	Median size of sediment
e_0	Maximum sediment porosity
E	Ekman number
E_{wave}	Wave energy density
E_{sed}	Sediment resuspension flux

E_{tot}	Sediment resuspension rate
f_{sw}	Wave skin friction coefficient
f_w	Wave friction coefficient
F_c	Friction coefficient
g	Acceleration due to gravity
G	Water column shear stress
$G_{\theta,S}^{n-1}$	Explicitly terms of the tracer at iteration of n-1
$G_{\theta,S}^{n}$	Explicitly terms of the tracer at iteration of n
$G_{\theta,S}^{(n+1/2)}$	Explicitly terms of the tracer at iteration of n+1/2
$\vec{G}_{\vec{v}}^{n-1}$	Explicitly terms of velocity at iteration of n-1
$\vec{G}_{\vec{v}}^{n}$	Explicitly terms of velocity at iteration of n
$\vec{G}_{\vec{v}}^{n+1/2}$	Explicitly terms of velocity at iteration of n+1/2
H	Wave height
h	Water depth
i	Index in the x direction
j	Index in the y direction
k	Wave number
k_b	Geometrical bottom roughness
k_{bc}	Apparent bottom roughness caused by the turbulence in the wave boundary layer
k_{bd}	Grain roughness

k_{br}	Drag roughness
k_T	Temperature diffusivity coefficient
k_{TH}	Temperature horizontal diffusivity coefficient
k_{Tv}	Temperature vertical diffusivity coefficient
K	Coefficient of different status of incipient motion
K_H	Horizonatal eddy diffusivity coefficient
K_v	Vertical eddy diffusivity coefficient
M	Non-dimensional buoyancy frequency
N	Wave action density
$\vec{n}$	The normal to a solid boundary
P	Pressure
P_{dep}	Probability of deposition
Q_S	Salinity forcing or effective salinity flux
Q_T	Temperature forcing or the net heat flux
S	Salinity
S_{tot}	Wave source/sink term that represents all physical processes
S^*	Estimated salinity
t	Time
T	Temperature
T_d	Time after deposition (days)

U	Horizontal velocity in the x direction
$\vec{u}$	velocity vector = (U,V,W)
u_{*c}	Current bottom shear velocity
u_{*cw}	Total bottom shear velocity caused by currents and waves
u_{*s}	Total skin friction shear velocity
u_{*sc}	Current skin friction velocity
u_{*sw}	Wave skin friction velocity
u_{*w}	Wave bottom shear velocity
V	Horizontal velocity in the y direction
U_M	Wave induce maximal horizontal velocity at seabed
$\vec{v}^{*}$	Estimated horizontal velocity vector
$\vec{v}^{**}$	Matrix inversion of the estimated horizontal velocity vector
W	Vertical velocity
w_s	Vertical velocity at sea surface
W_x	wind speed in the x direction
W_y	wind speed in the y direction
W_s	Sediment settling velocity
x	Spatial co-ordinate in the horizontal x direction
y	Spatial co-ordinate in the horizontal y direction
z	Spatial co-ordinate in the vertical direction

z_m	Skin friction sublayer thickness
α	The thermal expansion coefficient
α'	Coefficient in the settling speed formula of cohesive flocs
β	The haline contraction coefficient
β'	Power coefficient in the settling speed formula of cohesive flocs
σ	relative frequency
γ_0	Initial dry bulk density
γ_{0*}	steady dry bulk density
λ	Ripple spacing
ρ	Density of the water
ρ_0	The reference density
ρ_s	Sediment density
θ	Denote temperature as an tracer
θ^{n+1}	Temperature at iteration n+1
θ^*	Estimated temperature
κ	Karman constant
κ_T	Coefficient of thermal diffusivity
κ_S	Coefficient of salt diffusion
δ	Thickness of pellicular water
μ	Coefficient of dynamic viscosity

ε	Sediment resuspension potential
η	Water elevation
η^*	Estimated water elevation
ς	Ripple height
τ	Shear stress
τ_b	Seabed shear stress
τ_c	Critical shear stress for erosion
τ_d	Critical shear stress for deposition
φ	Latitude
ϕ_{hyd}^n	Hydrostatic pressure
Φ	Wave propagation directions
ω	Angular wave frequency
Ω	Rotational speed
∇	Vector differentiation operator $= \frac{\partial}{\partial x} + \frac{\partial}{\partial y} + \frac{\partial}{\partial z}$
L^{-1}	Matrix inversion
ε_{AB}	A small but finite value
ε_{fs}	Free surface factor; 1 means free-surface; 0 stands for rigid-lid.
δ_w	Wave boundary layer thickness
BYECS	Bohai Sea, Yellow Sea and East China Sea
CYSM	Central Yellow Sea Mud

SYS	Southern Yellow Sea
SSC	Suspended Sediment Concentration
SSF	Suspended Sediment Flux
YECS	Yellow Sea and East China Sea
YSCWM	Yellow Sea Cold Water Mass

Acknowledgement

I would like to take this opportunity to thank some of the people who have given me precious helps and support through my study.

Firstly, I would like to express my deepest appreciation to my supervisor, Professor Ping Dong for his guidance and inspiration during this dissertation work and throughout my studies and living at University of Dundee. His enthusiasm, professionalism and broad view on research had a great impact on me, both in the disciplines of research and about the attitude for life. He encouraged me to do interdisciplinary research to investigate the issue, and at the same time gave me constructive suggestions, guidance, and encouragement.

Lots of thanks to my colleagues Haixia Xu, Qinqin Gui, Yiqiang Chen, Chunyang Xu and Mohammad Baba Ahmadi for being together, sharing together and encouraging each other.

I gratefully acknowledge the financial support provided by the University of Dundee and Chinese Scholarship Council.

I’d like to thank my parents for their support, encouragement, patience and love.

I hereby certify that the work embodied in this dissertation is the result of original research and has not been submitted for a higher degree to any other University or Institution

_____

Chunyan Zhou

Abstract

A combined hydrodynamic and geological analysis of sedimentary and dynamical processes associated with the mud deposits on the continental shelves of Yellow Sea is carried out to synthesize a diverse set of measurements and information, and to identify dominant factors that contribute significantly to the formation of these deposits. The geological analysis makes use of available data, especially those recently collected cold water mass and deep core data while the hydrodynamic and sediment transport processes are quantified using a 3D hydrodynamics model that incorporates the effects of tides, waves and wind. The model study helps to infer from modern shelf sea processes the pathways and control mechanisms of fine sediment transport and check against the deposition rate determined from the core analysis so as to establish the links between sediment supply, accumulation, and dynamics for the deposits.

It is found that the fine sediments discharged from Huanghe River and Changjiang River and the resuspended sediments of Old Huanghe Delta are the main source for the mud deposit at the Southern Yellow Sea (SYS), which is supported by all sedimentological, mineralogical, and geochemical and fluid flow evidence. The tidal current flow is the main agent for transporting the fine sediment to the mud deposit in the central South Yellow Sea. But tidal action alone is insufficient to account for the volume of the deposit. Wind waves play an important role in maintaining suspension concentration and causing sediment resuspension, particularly from the Old Huanghe Delta where strong winter storms, mainly caused by Asian Monsoon, combined with strong current circulation can transport a large quantity of fine sediments from Old Huanghe Delta to the central SYS in winter. The existence of Yellow Sea Cold Water

Mass circulation caused by density difference at SYS provide favourable environment for suspended sediment to be trapped and deposited near the front between YSCWM and the coastal water in the Subei coast in summer.

The average deposit of Central Yellow Sea Mud (CYSM) is 3.6 $\times 10^7$t a^{-1} based on high-resolution Chirp sonar profiles combined with cores information. Under present hydrodynamic condition, the numerical model showed that approximately 16% (1.33×10^8t a^{-1}) of the Huanghe River derived sediment is transported out of Bohai Strait and nearly 7% (5.72×10^7t a^{-1}) will finally transported to the South Yellow Sea, quite close to the budget estimated by Alexander *et al.* (1991), that 9-15% of the annual Huanghe discharge is accumulating in the Yellow Sea based on ^{210}Pb sediment accumulation rate data.

The tidal fields and wave distribution in the Yellow Sea had changed significantly during the rapid sea-level rise over the 12, 000 years. The number of amphidromic points of M2 and S2 increased from 2 to 4 while that of K1 and O1 increased from 1 to 2 as the sea level rose from -60m, -30m to -15m. The amplitudes of M2 and S2 in the Yellow Sea and Bohai Sea enlarged and co-phase line rotated anti-clockwise as sea-level increased from -60m to 0m. The wave height also increased because the water depth increased with rising sea level. When the sea level was low, the shoreline and shallow region were closer to the CYSM area, therefore, the Huanghe River derived sediments and the resuspended sediments only need travel shorter distance to reach CYSM, which was favourable for the sediment deposited in the CYSM area.

Chapter 1 Introduction and thesis outline

1.1 Introduction

Research over the past decades has documented the common occurrence of fine-grained sedimentary deposits on continental shelves, mostly associated with rivers that discharge fine sediments along many coasts around the world, such as muddy deposits on the Southern Yellow Sea shelf, in the Gulf of Maine shelf off the northeastern U.S. (Piotrowicz *et al.*, 1981; Barnhardt *et al.*, 1997; Ward *et al.*, 2008), northern Irish Sea shelf (Belderson, 1964; Kershaw *et al.*, 1988; Marshall McCabe, 1997; Merino *et al.*, 2000; Macken *et al.*, 2009), North Sea shelf (De Haas *et al.*, 1997; Graham *et al.*, 2010), off amazon river (Kineke and Sternberg, 1995; Kineke *et al.*, 1996) and so on. These mud deposits contain an abundance of information about the climate including temperature changes, occurrence interval of large flood events and the possible influencing factors, which has attracted much research attention.

Over geologic time, continental shelves are repeatedly flooded and exposed by relative rises and falls in sea level. As such, shelves are shaped and reshaped by subaerial, coastal, and submarine processes. As the temporal and spatial scales over which shelf morphology and strata are created are beyond the realm of direct observation, the formation genesis has to be studied using various indirect methods involving sedimentology, oceanography and geochemistry as well as numerical models for flow and sediment transport. The incompleteness of the stratigraphic record and the records of past environments together with the inherent limitations of each of these methods complicates matters even further for it riddles geologic interpretations of strata with uncertainties about what formed when, where, why, and how. The findings from previous studies of the Yellow Sea regarding sediment origins,

budgets, accumulation rates, mineralogical, and geochemical compositions, for example, can often be inconsitent with one another, even contradictory.

The present research is concerned with the flow and sediment transport processes of the Yellow Sea, with a particular focus on the formation mechanisms of the muddy deposition patch in the central Southern Yellow Sea (Fig. 1.1). The Yellow Sea, lying between Chinese Continent and the Korean Peninsula, is an epicontinental sea. Its depth is only 44m on average with the deepest of 140 m near the south end of the Korean Peninsula. The line connecting the Changjiang (Yangtze) mouth and the Cheju Island divides the Yellow Sea from the East China Sea, and the Yellow Sea is further divided into North Yellow Sea and South Yellow Sea by the line linking Chengshanjiao (the farthest east point of Shandong Peninsula) and Changshanchuan in Korean Peninsula.

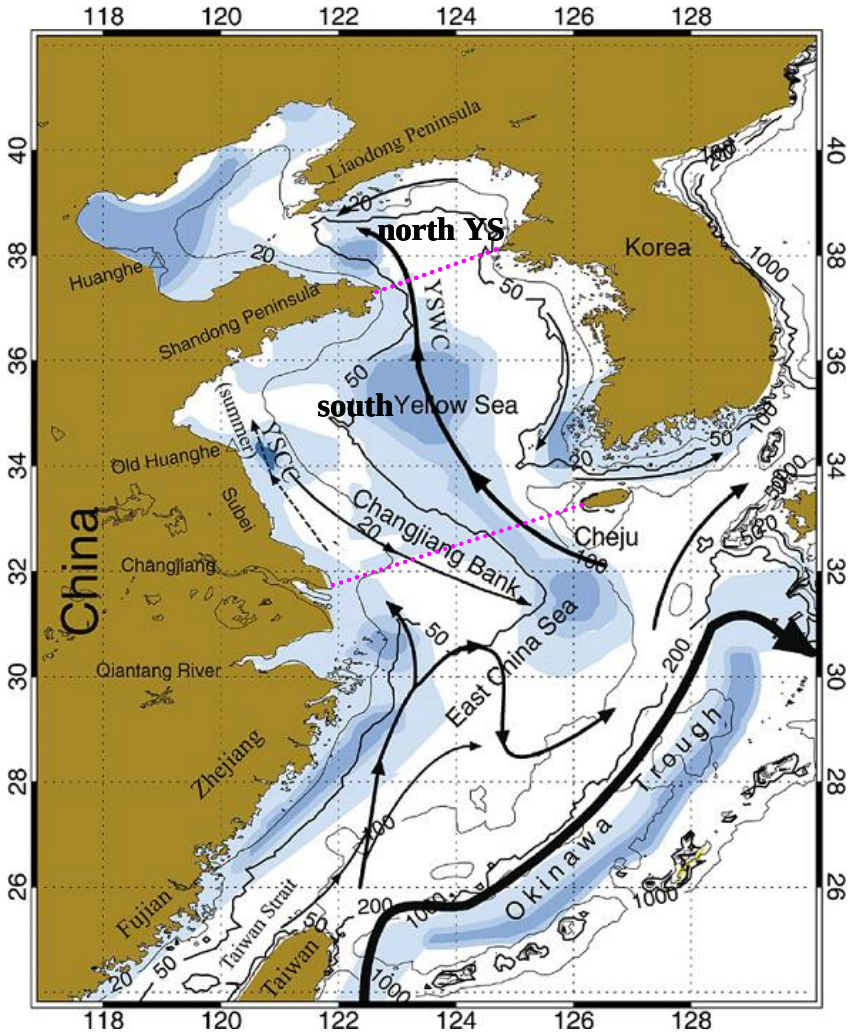

Fig. 1.1 Regional map and bed contours of the Yellow Sea.

where Contour unit is meter. Shaded areas show distribution of mud patches at the sea bed, with darker colours indicating finer grain sediments. The arrows indicate the Yellow Sea Warm Current (YSWC), the Yellow Sea Coastal Current (YSCC), the Korea Coastal Current (KCC), the Tsushima Warm Current (TSWC), and the Taiwan Warm Current (TWC) in the map. The dash arrow along the Subei coast marks the YSCC in summer(Yuan *et al.*, 2008).

There are abundant natural resources of aquatic products, offshore petroleum and gas in the Yellow Sea. The temperature or salinity change of the Yellow Sea influences the climate and marine fishery management and even marine military activities. The sediment concentration can also directly affect marine life in the ocean in several ways such as by hindering the settling of plankton (which benthic vertebrates feed on), causing a decrease in the population, and thus affecting the food chain. Highly turbid water might negatively impact fish by causing physiological

stress, reduce their ability to feed, as well as decreasing their reproduction rate. The suspended sediments also play an important role in spreading and transport of pollutants, since it affects the upper bottom sediment layer which is brought into suspension by currents and waves (Holmedal *et al.*, 2004). Thus, in the past few decades the hydrodynamic and sediment transport process in Yellow Sea has attracted considerable research attentions.

However, the ocean circulation and sediment transport patterns in the Yellow Sea are very complex. There exist many controversial opinions and even intractable problems despite the accumulation of large amount of knowledge based on sediment size and geochemical data, satellite data, circulation models, oceanographic in situ measurements, and high-resolution seismic stratigraphy (Milliman *et al.*, 1985; Lee and Chough, 1989; Martin *et al.*, 1993; Kim and Kucera, 2000; Chough *et al.*, 2002; Liu *et al.*, 2004a; Liu *et al.*, 2008b; Hu *et al.*, 2012; Hu *et al.*, 2013).

In particular, the genesis of mud patch in the central South Yellow Sea is still subject to intense debate. The most popular explanation is that flow upwelling would occur in the central part of cyclonic cold eddy and this upwelling would deposit fine grained materials so as to form mud patch (Hu, 1984; Pang and Hu, 2002; Shi *et al.*, 2002). On the other hand, others have argued that weak tidal currents are mainly responsible for the fine-grained sediment deposition and formation of the muddy patches. The simulation results described by Zhu and Chang (2000) indicate that the muddy patches (clayey sediments) in the Yellow sea can be formed in areas with weak tidal currents, even without cold eddies, which means that the existence of cold eddies is not a necessary condition for the formation of mud patches. As these studies are limited to flows predicted using hydrodynamic models the full understanding of the actual roles of cold eddies and tidal currents in the formation of the mud patch in

the Yellow Sea would require further studies drawing on information from wider sources.

1.2 **Aim and objectives of the research**

The overall aim of this study is to investigate the genesis of fine sediment deposits in the central Southern Yellow Sea and identify key factors contributing to its formation**.** No single method exists that can account fully for the complexity of the hydrodynamic and morphological processes over the large geological time scale involved in the formation of the fine sediment deposits, in other words, the long term numerical simulation can not reach the thousands of years scale, so the deposition rate, sediment budget, and the mud formation/evolution actually need the geological information, while the geological information can not reveal the processes involved in the mud deposit formation. Thus, a range of methods have been applied to achieve an improved understanding and develop a synthesis.

In order to meet these aims the following objectives have been identified:

- Investigate the provenance and mechanism of the mud deposits using geological approaches.
- Provide convincing evidence to explain the dominant processes responsible for the formation of the deposits.
- Indentify the key processes to the formation of the deposits by using a 3D hydrodynamics model and considering the effects of waves, currents and winds on the flow field and sediment transport pathways.

1.3 **Outline of the thesis**

The thesis is organized as followings:

Chapter 1 (Introduction and thesis outline) provides background information about mud deposits in the shelf worldwide, especially the mud patch in the central Southern Yellow Sea, why its formation is so important and what are the main problems regarding its genesis. It also outlines the key aims and objectives of the study as well as the structure of the thesis.

Chapter 2 (Literature Review) gives a comprehensive review on the hydrodynamic and sedimentary processes and provenance discrimination of Yellow Sea. It covers the provenance research based on sediments composition and geo-chemical approaches, hydrodynamic modeling and field measurements, geological methods such as stratigraphy, sediment cores, sedimentary facies analysis, etc.

Chapter 3 describes the geological evidence of sediment dynamics in terms of sediment characteristics, deposition rate and sediment budget mostly based on the new data in order to understand the origin and dispersal systems of the Yellow Sea sediments.

In Chapter 4, an enhanced version of the open source model (MIT General Circulation Model) is introduced in detail including the hydrodynamic module, wave module, bottom boundary layer module and sediment module.

Chapter 5 describes the scenario-based numerical experiments results and discuss the key questions identified in the introduction using the information from both

geological and modelling aspects. The limitations and uncertainties of research and results are also explored.

Chapter 6 (Conclusions) the major findings of the research are summarised and recommendations for further studies are presented.

Chapter 2 Literature review

The existing research literature on Yellow Sea covers mostly sedimentology, oceanography, and geochemistry of the Yellow Sea. A comprehensive review on sediment dispersal and provenance discrimination are therefore necessary in order to establish the current knowledge, identify knowledge gaps and set out the scope of this research.

The literature review mainly includes three aspects: the provenance research, hydrodynamic modelling and field measurements, geological methods.

2.1 **Provenance**

Due to its unique geographic location, the Yellow Sea receives abundant terrigenous sediments from neighbouring rivers, mostly from the Changjiang and Huanghe River and also from coastal erosion at the Subei, the Old Huanghe delta. Muddy sediments dominate the central part of the South Yellow Sea (represented by CYSM) while sand and muddy sand blanket the eastern and the western parts of the sea (Fig. 2.1).

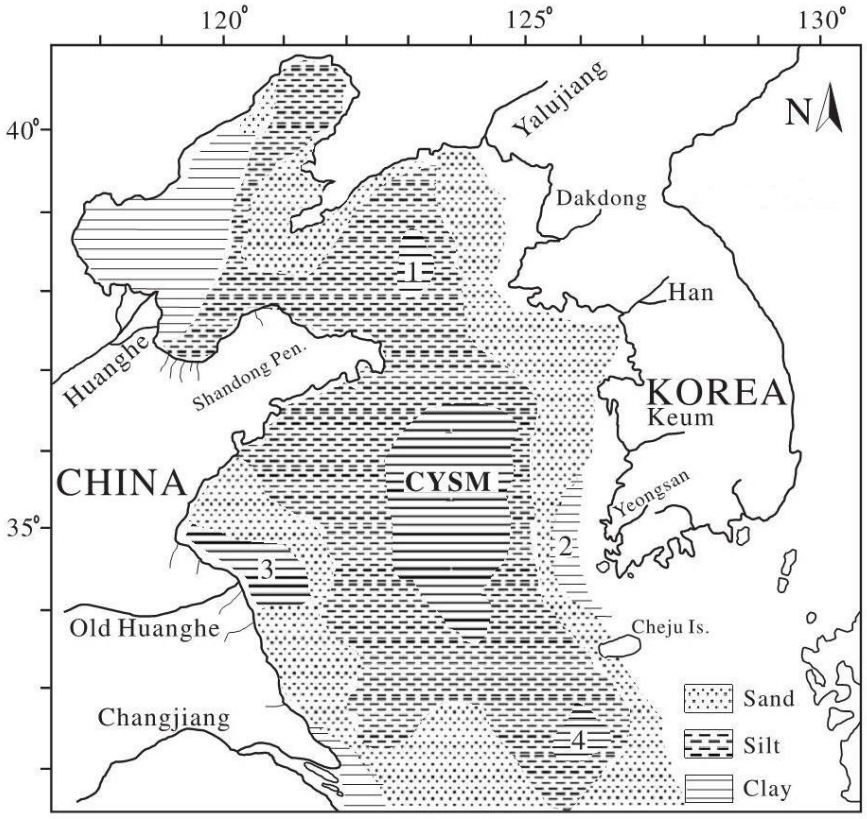

Fig. 2.1 Surface sediment distribution in the Yellow Sea and adjacent areas. where CYSM: Central Yellow Sea Mud; (1) NYSM, North Yellow Sea Mud; (2) SEYSM, Southeastern Yellow Sea Mud; (3) SWYSM, Southwestern Yellow Sea Mud; (4) SWCIM, Southwestern Cheju Island Mud (Yang *et al.*, 2003).

Extensive work has been carried out to determine its sediment origin. The clay and heavy minerals of the river sediments were analyzed using X-ray diffractgrams to investigate the geochemical characteristics of Chinese and Korean river sediments, in order to reveal their compositional differences and then establish suitable geochemical source indicators.

High $CaCO_3$ content has been widely used to distinguish the Huanghe sediment from other Chinese river sediments and particularly from the Korean river sediments which have extraordinarily low $CaCO_3$ contents. The $CaCO_3$ contents in the western muddy sediments of the CSYS are about two times higher than those in the eastern sandy sediments, indicating that most of the fine sediments in the western part of the CSYS were probably derived from the Huanghe River. However, the $CaCO_3$ content

alone cannot be used directly as a reliable provenance indicator to discriminate sediment origins of the Yellow Sea, because its content in marine sediments is influenced by grain size composition of sediment and biogenic carbonate including shell fragments, which can be difficult to discriminate from detrital components. (Yang *et al.*, 2003).

On the basis of newly compiled clay mineral synoptic maps, the depositional processes were described for four main clay minerals (illite, chlorite, kaolinite and smectite) with X-ray quantitative determinations of surface samples obtained from the south YS. The analysis revealed that the sediments in northern part of CYSM mainly come from the Huanghe River, and those in the southern part are multi-origin (Wei *et al.*, 2003).

Smectite, one of the clay minerals, whose contents are reported to be much higher in Huanghe sediments (>10%) and in Changjiang sediments (>5%) than those in Korean river sediments (< 5%) (Park and Khim, 1992; Lee and Chu, 2001), was considered for provenance discrimination in the Yellow Sea. The smectite contents distribution shows higher value in the western Yellow Sea than that in the eastern part (Park and Khim, 1992). The NYSM contains relatively higher smectite contents than that of the CYSM and SEYSM, suggesting the obvious influence of the Huanghe sediment there (Cheng, 2000). It was so suggested that the provenance of the CYSM may be closely related to the old and present-day Huanghe River system based on clay mineral (especially smectite) concentration analysis of 52 sediment samples from the Yellow Sea continental shelf (Park and Khim, 1992). However, new data and analysis show that clay mineral assemblages in Chinese or Korean river sediments may vary significantly (Yang *et al.*, 2003), depending on sample processes, analytical conditions, and calculation methods (Park and Khim, 1992; Zhao *et al.*, 2001),

resulting in higher smectite contents in Korean river sediments than previous reports, which casts doubt on the application of smectite to distinguish Chinese and Korean river sediments. Furthermore, clay mineralogy, especially smectite, may obviously change in the sea because of submarine weathering and diagenesis of clay minerals (Chamley, 1997), also suggesting smectite contents are not a reliable indicator to discriminate the sediment sources in the Sea.

Heavy minerals, which are detrital grains of minerals with high density (>2.9) such as magnetite, garnets, zircon, rutile and so on, were also adopted to discriminate sediment source of SEYSM and the CYSM (Lee and Chough, 1989; Zhao *et al.*, 1990; Li *et al.*, 2001), but suggestions from heavy minerals are not always consistent with the results from the mineralogical characters. Strong hydrodynamic regime in the Yellow Sea, especially in the eastern part, may restrict the application of heavy minerals as the indicators of sediment source because distribution patterns of heavy minerals can be easily changed by the reworking and redistribution of bottom sediments (Morton, 1991).

Alkaline earth elements (Ca, Sr, Ba, Mg) concentrations vary a lot between Chinese and Korean river sediments, resulting from remarkably different provenance compositions and weathering processes in their drainage basins. The distribution of alkaline earth elements of surface samples of the Yellow Sea also suggested the sediment of CYSM was mainly originated from Huanghe River. (Kim *et al.*, 1999). However, the application of alkaline earth elements to trace the Huanghe sediments in the Yellow Sea has been confined to limited areas because of the instability of these elements in sedimentary environments and of strong disturbance of biogenic components(Martin *et al.*, 1993; Cho *et al.*, 1999).

Most of the transition metals are enriched in detrital materials, primarily as the residual fractions (Kim *et al.*, 1998b). Cho *et al.*(1999) indicated that source of fine sediments in CYSM is Huanghe River based on the spatial distribution that the highest V/Al (Vanadium / Aluminum)values occur in mud samples from the central Yellow Sea, because only silt sediments discharged from Huanghe River are characterized by high V/Al value, other than Changjiang River and other rivers in Korean coast.

The granulometric characters of sediments can have considerable influences on elemental concentrations. For example, alkaline earth elements are enriched in sandy sediments, while transition metals (Co, V, Cr, Mn, Zn, Cu, Pb and Ni) are concentrated in clay and silt fractions in the Yellow Sea (Fig. 2.2). Thus, the spatial distribution patterns of most elemental concentrations are similar with grain size variations.

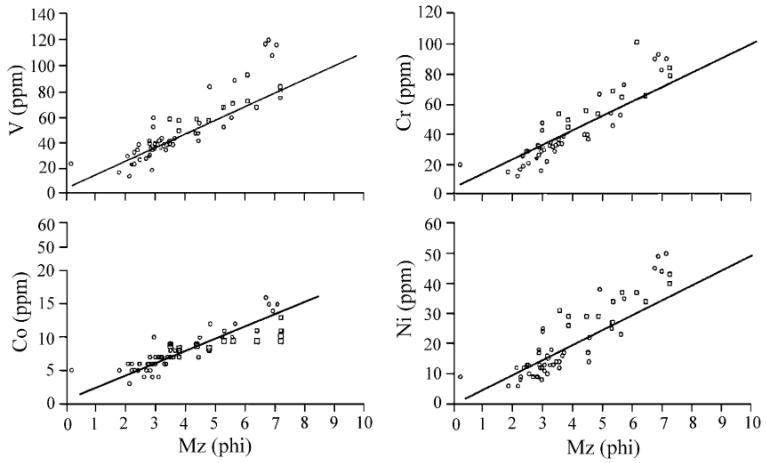

Fig. 2.2 Relationships between the content of transition metals and the mean grain size (Mz) in the sediments of the around the Keum Estuary (square) and Yellow Sea (circle). Lines are best-fit regression lines (Cho *et al.*, 1999).

The trace metals were considered to differentiate Chinese and Korean river sediments. For example, the concentrations of Ca and Sr in Chinese river sediments,

especially the Huanghe sediments, are significantly higher than those in Korean river sediments. However, the dramatically variable concentrations between the rivers are possibly caused by severe pollution in rivers, rather than by the difference in source rock compositions(Cho *et al.*, 1999).

Zhao *et al.* (1990) reveals that the CYSM is multi-sourced rather than from a large single source according to geochemical characteristic of surface sediments. Fine-grained suspended materials tended to be deposited slowly under cyclonic gyres of the flow to form the modern muddy patches.

Rare earth elements (REE) are widely used sediment source indicators (Rollinson and Data, 1993; Allègre *et al.*, 1996; Derry and France-Lanord, 1996; Revel *et al.*, 1996; Ahmad *et al.*, 2005) because they generally behave conservatively in hypergene environment and reside mostly in mineral lattices (Taylor and McLennan, 1985; Fralick and Kronberg, 1997). However, they have only been occasionally used to identify the sediment origin in the Yellow Sea (Wang *et al.*, 1983; Asahara *et al.*, 1995; Yang *et al.*, 2007; Mao *et al.*, 2011). REE concentration in the Yellow Sea sediment ranges from 64 to 256μg/g with an average of 175μg/g, concentrating in the clay component and depleting in sands(Wang, 1990). REE composition of the Yellow Sea sediment has relatively Light Rare Earth Element (LREE)-enriched pattern with negative Europium (Eu) anomaly. Heavy minerals have a significant control on REE concentration, and major part of REE resides in residual fraction (Wang, 1990; Zhao *et al.*, 1995). It is suggested that the provenance of the Yellow Sea sediment could not be easily differentiated according to uniform REE patterns and similar fractionations (Nohara *et al.*, 1999). Recent investigation, however, indicated that REE concentrations and fractionation patterns of the Changjiang and Huanghe sediments are different (Yang *et al.*, 2002), and also different from those of Korean river

sediments, suggesting the potential application of REE for provenance discrimination of the Yellow Sea sediment.

Isotopic approach has rarely been applied to identify the sediment origin in the Yellow Sea, except for a few attempts in recent years (Nohara *et al.*, 1999; Meng *et al.*, 2000). The different source rock compositions and weathering degrees between Huanghe and Changjiang drainage basins account for the different $^{87}Sr/^{86}Sr$ ratios of sediments discharged into the sea. It is reported that Huanghe sediments have lower $^{87}Sr/^{86}Sr$ ratio (0.7120 or 0.7193) than the Changjiang sediments (0.7250 or 0.7243), probably implying a new tracer for discriminating both river sediments in the sea.

Generally speaking, more elements are required to be studied in detail in aspect of regional distribution patterns in the Yellow Sea, besides the alkaline earth elements (Ca, Sr, Ba) and some transition metals (Mn, Pb). Especially the elements (REE, Sc, Li, Zr, Hf, Nb, and Be), which generally behave conservatively, should be adopted more widely for provenance discriminations of river and marine sediments. The rather limited report of these elements (REE, Ti) for source identification of the Yellow Sea sediment is clearly insufficient to reveal the distribution patterns of these elements in the Yellow Sea yet.

Similarly, study on stable and radioactive isotopes of the Yellow Sea sediments need to be strengthened because recent advances in the field of analytical instrumentation make the particular analysis of isotopes easier and more important. This approach has been proved to be very powerful in provenance study.

2.2 **Hydrodynamic processes**

Sediment transport in the Yellow Sea is affected by sediment properties, tidal currents, shelf circulation, density driven circulation and wind waves (Lim *et al.*,

2007). The transport and deposition of these sediments have resulted in the formation of a large muddy patch in the central part of southern Yellow Sea (Park and Khim, 1992; Kim *et al.*, 1998a; Yang *et al.*, 2003). These processes, and particularly how they influence mud distributions in Yellow Sea, are reviewed as follows.

It has been observed that circulation in the Yellow Sea shows considerable seasonal variations. Generally speaking, the circulation pattern in winter is characterized by the northward flowing YSWC in the trough of the Yellow Sea and the southward flowing coastal currents along the coasts of China and Korea, including the Yellow Sea Coastal Current (YSCC), the Korea Coastal Current and the Liaonan coastal current. The YSWC, which is the main component of the Yellow Sea circulation in winter, transports warm and saline water of the open ocean into the Yellow Sea. The YSWC is highly time dependent and is an episodic current forced by southward pressure gradient during the relaxation of the northerly wind burst (Mask *et al.*, 1998; Isobe, 2008). In summer, observations show that the YSWC turns eastward into the Cheju Strait between Cheju and the Korea Peninsula instead of intruding into the Yellow Sea. Instead, the deeper region of South Yellow Sea is occupied by the Yellow Sea Cold Water Mass (YSCWM) beneath the thermocline. The coastal currents, on the other hand, have not been sufficiently measured. Early observations show southward movement around the Shandong Peninsula and along approximately the 40–50 m isobaths in the area of 33 °–34 ° N. Recent direct current measurements near the coast of China in the southern Yellow Sea suggest that the currents in the area shallower than 30 m are to the north (Liu *et al.*, 2008b).

The strong northwest monsoonal wind prevails in the winter with average speed of 8-9m/s while southeast in summer with mean speed of 4-6m/s. The mean wave height, wave length and wave period are 1-1.5m, 30-50m, 4-5s respectively. But the wave

height can frequently reach 2-5 m in the autumn and winter seasons. The wind wave is expected to play a very important role in the transport and sedimentation processes of suspended matter in the shallow Yellow especially during winter (Yanagi and Inoue, 1995).

Eight survey cruises in different seasons, conducted in the Yellow Sea during the period from 2000 to 2008 (Dong *et al.*, 2011), demonstrated that highly turbid waters were found in the shallow waters of the Subei coast with seasonal variations and suggested that suspended sediments were transported from the Subei coast and the southern entrance of the Yellow Sea Trough to the central YS. It is inferred that the front between the Yellow Sea Cold Water and the coastal water in the Subei coast appeared to trap the high Suspended Sediment Concentration (SSC) sediments on the shallow water side of the front. The mud patch in central South Yellow Sea is believed to form when tidal currents were too weak to erode the bottom sediments and water column stratification and eddies provided favourable conditions for trapping the fine-grained suspended sediments.

Many numerical simulations of Yellow Sea also have been carried out. Park and Chu (2006) investigated seasonal variability of surface and subsurface thermal/saline fronts in the Yellow based on three-dimensional monthly-mean temperature and salinity data from U.S. Navy's Generalized Digital Environmental Model. A wave-tide-circulation coupled numerical model simulated the temperature structure in the Yellow Sea and compared with the observations (Xia *et al.*, 2004). Three-dimensional circulation has been computed to exhibit the two distinct circulation modes for winter and summer based on seasonal hydrography, mean winds, mean discharge from the Changjiang River, and invariant oceanic tides without consideration of the waves (Naimie *et al.*, 2001). A general ocean circulation model results show that the shelf

circulation of Yellow Sea and East Sea in winter is induced primarily by the northerly monsoonal winds (Yuan and Hsueh, 2010). Yang et al (2004) calculated wave-induced mixing effect and showed that it is strongest in winter due to winter monsoon while weakest in spring. It can affect temperature distribution even to 40-50m below the surface in summer. The wave in shallow water area is shown to have a great impact on the bottom shear stress and the net sediment transport process (Holmedal and Myrhaug, 2006; Xing *et al.*, 2011). The velocity components across tidal fronts, examined using a 3D nonlinear numerical coastal circulation model, indicated that upwelling motion appears around all the fronts with different velocity structures, accounting for surface cold water around the fronts. The numerical experiments also suggest that the location and formation of fronts are closely related to topography and tidal mixing, as is the velocity structure around the front (Liu *et al.*, 2003).

A three-dimensional suspended sediment model (SED) is combined with the coupled 3-D hydrodynamic model (COHERENS) and a third-generation wave model (SWAN) in order to simulate three-dimensional suspended sediment transport near the Huanghe River mouth with wave-current co-existing (Liang *et al.*, 2007). The simulated significant wave height and wave period for a case with current's effects was shown to give better agreement with measurement data than without the current.

Lu *et al.* (2011) embedded a sediment numerical model into a wave-tide-circulation coupled model to simulate the transport processes of the Huanghe River-derived sediment, and suggested that the main stream of the Huanghe River derived sediment moves first eastward off the northern Shandong Peninsula and then southward into the South Yellow Sea all year round.

Lu *et al.* (2013) then calculated the Suspend Sediment Flux (SSF) of three different section in the Bohai Sea and Yellow Sea based on numerical model results. The SSF

across the Bohai Strait is about 30 % of the Yellow River discharge, while across the 37 ° N section it is 15.8 %, which means that about 70 % of the total discharged Yellow River sediments are deposited in the Bohai Sea, 14.1 % in the North Yellow Sea, and 13.9 % in the South Yellow Sea. The model results depict two deposition branches in the Yellow Sea. The primary one is situated off the eastern tip of the Shandong Peninsula and extends to the southwest off the coastline, matching well with the observed "Ω"-shape deposition pattern. The secondary branch extends to the middle of the South Yellow Sea and has been strengthened by resuspension process. These two deposition branches are separated by the wintertime Yellow Sea Warm Current in the bottom layer.

Furthermore, Yuan *et al.* (2008) calculated the speeds of cross-shelf sediment transport and vertical descending of the suspended sediments in the Yellow Sea based on MODIS satellite observations, much faster than those simulated by Yanagi and Inoue (1995). Therefore, it is necassary to improve the sedimentation dynamics and parameterizations in the numerical model in order to simulate the sediment transport more accurately.

However, due to the complexity of hydrodynamic and sediment transport patterns and processes in the Yellow Sea, there are still many controversial opinions of the hydrodynamic and sediment transport mechanism of Yellow Sea and there are often lack of detailed data to support the various hypothesis proposed.

In particular, the Yellow Sea Cold Water Mass (YSCWM) has drawn extraordinary attention from scientists in terms of circulation related to the genesis of the mud patch in the central SYS. Because it is inferred that upwelling exists at the central part of a cyclonic eddy and wherever upwelling occurs on continental shelf, mud should be formed, on the contrary, wherever downwelling exists, coarse sediment should be

deposited (Hu, 1984; Pang and Hu, 2002; Shi *et al.*, 2002). However, some important aspects of the YSCWM circulation remain controversial.

The Yellow Sea Cold Water Mass (YSCWM) is a bulk of cold water below seasonal thermocline from spring through autumn in the Southern Yellow Sea (Hu and Wang, 2004). It is considered as a remnant of winter cooling and mixing and observed clearly in the deeper locations during summer. The CTD data showed salinity was almost vertically homogeneous ranging from 30.7 to 32.8psu. A thermocline appears at the middle depth of the water column. Temperatures were almost homogeneous above and below the thermocline. The upper layer was 26-28 m thick with a temperature of 23.5°C, while the lower layer was 33 m thick with a temperature of 9.8°C. And there are thermal front in the coastal area, which is a zone with a pronounced horizontal temperature gradient (Fig. 2.3).

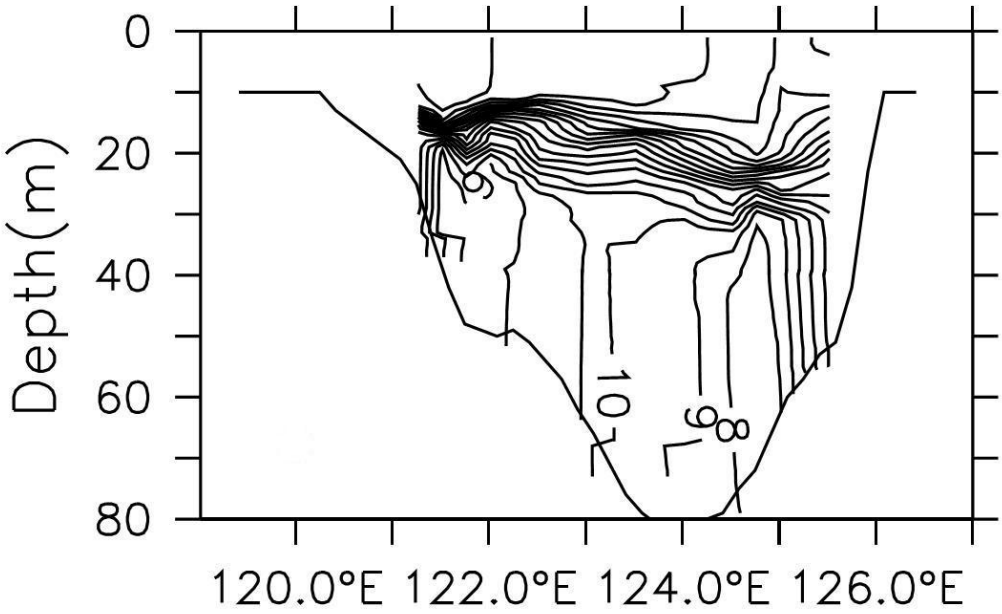

Fig. 2.3 Observed vertical temperature structure along 35 ^{o} N section in July (Xu *et al.*, 2003)

Temperature and salinity stratification can cause internal wave under tide force. In the southern Yellow Sea, internal waves are observed mainly at the west coast of Korea in summer (Alpers *et al.*, 2005). Interaction between the semi-diurnal tidal

current with shallow topography near the Korean coast with strong stratification in the water column, are considered as the internal wave generation mechanism(Teixeira *et al.*, 2006). It is showed that the internal wave-generated bottom layer shear stresses are large enough to re-suspend sediment at Australian North West Shelf (Ribbe and Holloway, 2001).

Furthermore, when the thermocline intersected with the sea bottom, a front formed. Previous studies in the Yellow Sea show that this is a tidal front that tends to occur in the period from later spring to autumn (Xu *et al.*, 2003; Huang *et al.*, 2010). It is well known that the front inhibits the mass exchanges between its two sides. High Suspended Sediment Concentration (SSC) can often be observed in many estuary plume front zone (Kineke and Sternberg, 1995; Geyer *et al.*, 2004). As shown in Fig. 2.3, this front is where the shallow coastal water meets the Yellow Sea Cold Water in the Yellow Sea Trough. There is a strong coastal current on the shallow side of the front (Yuan *et al.*, 1982; Su, 1998) and it passes through the high SSC Subei coast and carries a huge amount of suspended sediments to the north of East China Sea (ECS). The suspended sediments are trapped in the bottom of the front and a high SSC layer is formed.

As for the lateral circulation of YSCWM, both observational and numerical studies have revealed different patterns.

Track of ARGOS satellite drifter buoys taken in summer 1986 showed a anticlockwise (cyclonic) circulation in the upper layer of central part of the YS (Choi and Lie, 1992). The trajectories of the five satellite-tracked drifters launched in the YS indicated a weak basin-scale cyclonic gyre in the surface waters in summer (Beardsley *et al.*, 1992). Tang *et al.* (2000) revealed that the summertime circulation is basically a basin scale anticlockwise flow in both the surface and bottom layers

based on the observations of the China-Korea Joint Investigation of Ocean Circulation Dynamics in the South YS.

However, the above float trajectory data are either short period coverage or low resolution, which make it difficult to investigate the circulation pattern adequately.

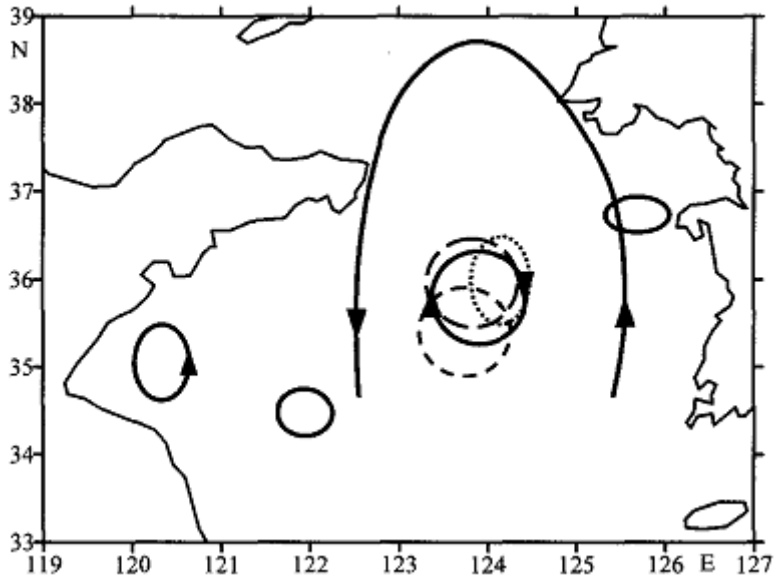

Fig. 2.4 General pattern of the upper circulation in the Yellow Sea in summer. (dotted line:2001; short-dashed line:2002; long-dashed line:2003) (Pang *et al.*, 2004)

Pang *et al.* (2004) revealed an mesoscale anticyclonic eddy (clockwise) with a mean speed and radius of 0.063 m/s and 50km exists in the upper layer of central southern based on the trajectories and drift velocities of 23 drifters, launched in summer of 2001, 2002 and 2003, which is not observed before (Fig. 2.4). A basin-scale elliptic cyclonic (anticlockwise) gyre with a mean speed of 0.114 m/s, long and short radius of 250 and 200 km respectively, situated outside of the above-mentioned anti-cyclonic eddy. This cyclonic gyre, also observed by other satellite-tracked drifters mentioned earlier, is widely accepted.

In terms of numerical model, Yanagi and Takahashi (1993), using a diagnostic model, revealed that an anticlockwise (cyclonic) circulation is developed at the upper layer and a clockwise one at the lower layer of the YS in summer. Thereafter, Takahashi and Yanagi (1995) suggested that these circulations are mainly induced by the topographic heat accumulation effect (THAE) with simple idealized topography basin.

Lee and Beardsley (1999) studied the influence of stratification on residual currents in the YS using estuarine, coastal and ocean model (ECOM) and indicated that the stratified tidal rectification intensifies the residual current at the front and at the top of the bottom layer over the sloping bottom. The residual current in the surface layer can reach 40% of the mean currents observed by Beardsley *et al.* (1992).

On the vertical circulation (or the cross frontal circulation) of the YS, three types of models for the YSCWM circulation have been proposed previously.

The first one is a cyclonic gyre with upwelling getting through the thermocline near the centre of the YSCWM and downwelling on the edges (Li and Yuan, 1992). The second is a conceptual double-cell circulation pattern in which downwelling in the upper layer and upwelling in the lower layer and no vertical flow through the thermocline at the centre of YCWM, based on the existence of dissolved oxygen maxima near the thermocline (Hu *et al.*, 1991; Feng *et al.*, 1992), which is also an indirect indication of the inhibiting effects of the thermocline on the vertical turbulence and advection, indicating that the water near the thermocline is stable and conservative.

However, others argued that the upper layer gyre consists of an upwelling branch in the centre of the YSCWM and downwelling within the frontal zone while, a reverse and much larger gyre occurs with upwelling in lower layer below the thermocline (Su

and Huang, 1995), which is contrary to that of the second type, though compatible to the second one in the sense of no vertical flow through the thermocline.

It is worth noticing that most of the simulated patterns have not been validated rigorously with direct measurements especially the vertical circulation because the vertical velocity is generally too small to measure.

2.3 **Geological methods**

The dynamic and sediment transport process of the south Yellow Sea is also studied extensively using geological methods such as stratigraphy, sediment cores, sedimentary facies analysis and so on.

Xiang *et al.*(2008) deciphered 3 stages of environmental development of southern Yellow Sea: 1. A low salinity estuarine environment stage, at 8.4–6.9 cal. kyr BP, 2. A low salinity shallow sea environment stage at 6.9 to about 6–5 cal. kyr BP and 3. A modern marine shelf environment stage after about 6-5 cal. kyr BP, based on the benthic foraminiferal, stable isotopic and grain-size data from an AMS ^{14}C dated Core YE-2 (123 °20'E; 35 °30'N) from the muddy southern Yellow Sea. It is indicated that major environmental changes occurred during the last 8400 years in the southern Yellow Sea, suggesting that the modern circulation was probably established at 6-5 cal. kyr BP.

The marine and terrestrial biomarkers of Core YE-2 were then analysed in detail (Xing *et al.*, 2012). The contents of three individual phytoplankton biomarkers (alkenones, brassicasterol and dinosterol) show an increasing trend during the last 8 200 years, while contents of terrestrial biomarkers (C_{27}+C_{29}+C_{31}*n*-alkanes) during the early Holocene (1661 ng/g) were about three times higher than those during the mid-late Holocene (499 ng/g). Biomarker results suggested that the modern circulation and

environments in the Yellow Sea were established around 6-5 cal. kyr, and resulted in higher marine productivity and lower terrestrial organic matter inputs, which is in agreement with previous results.

The abrupt change in carbon and oxygen stable isotopes of Core M5-5(119 °45.66'E, 38 °41.4'N) was recognized at about 6400 yr BP, indicating the intrusion of the Yellow Sea Warm Current (YSWC) extension into the Bohai Sea (Liu *et al.*, 2008a).

Based on stable isotope data and carbon and sulfur elemental analyses of core CC02 (123 °49.2'E, 36 °7.72'N) in the central part of the South Yellow Sea, the sedimentary environment of the Yellow Sea was significantly influenced by the sea level changes during the late Quaternary. The sedimentation rate in the central part of the Yellow Sea when the sea level was lower by 56 m (about 11,500 yr BP), was three times higher than the present rate (Kim *et al.*, 1998a).

Liu and his co-authors (Liu *et al.*, 2002; Liu *et al.*, 2007a) examined newly acquired high-resolution Chirp sonar profiles and revealed a unique Huanghe River-derived, subaqueous deltaic lobe deposited around the eastern tip of the Shandong Peninsula in the Yellow Sea and even extend to the center south Yellow Sea. Thickness of Holocene sediment generally decreases southward and towards the central part, from above 10 m near the tip of Shandong Peninsula (maximum 40 m), and along the Jiangsu Coast (maximum 30m) to less than 5 m in the CYSM. Radiocarbon-14 dates indicate this distal lobe has formed under a relatively stable sea level in recent 7000 years.

Modern (last 100 years) accumulation rates of shelf mud deposits derived from excess ^{210}Pb in sediment core samples, revealed a general cross-shelf decreasing trend along the sediment dispersal system away from the rivers in Yellow Sea and provided

findings on the sediment budget, origin, and transport pathway of the mud deposits (Lim *et al.*, 2007). Sediment accumulation rates on the 100-year timescale, estimated by ^{210}Pb geochronology, were very high in the SEYSM (up to 18.4mm/year) and the south of Shandong Peninsula (up to 8.6mm/year), while low in the CYSM, NYSM, and SWCIM (about 1-3mm/year) (Lee and Chough, 1989; Zhao *et al.*, 1990; Alexander *et al.*, 1991; Liu *et al.*, 2004a). However, on the 1000-year scale, more recent researches reveal that average sedimentation rates in the SEYSM and CYSM are quite low: 1-5 and 0.18mm/year, respectively (Park *et al.*, 2000). The recent study based on the trend analysis of sediment grain size, has demonstrated that the central Yellow Sea is a sedimentation center (123.4°E, 35.1°N) under the control of cyclonic circulation and cold water gyre, and the neighboring sediments are concentrated in there (Shi et al., 2002).

2.4 **Climate changes**

The Yellow Sea experienced dramatic sea level fluctuations during the late Quaternary (Fig. 2.5), which made itself as a natural laboratory to study the land-sea interaction. The Yellow Sea was exposed during the last sea-level low stand (16 kyr BP) with the lowest sea level of 130m below the present level. The sea level rose rapidly in the early stage of postglacial transgression (prior to 9000 year BP) and coastline advanced quickly towards the continent at a horizontal rate approaching 80 m/yr, because of the very shallow gradient in the Yellow Sea basin (<lm/km), and reached 4～5m higher than today around 7kyr BP (Liu *et al.*, 2004b), afterwards the sea level fell to the present level and stayed stabilization with minor oscillations (Alexander *et al.*, 1991).

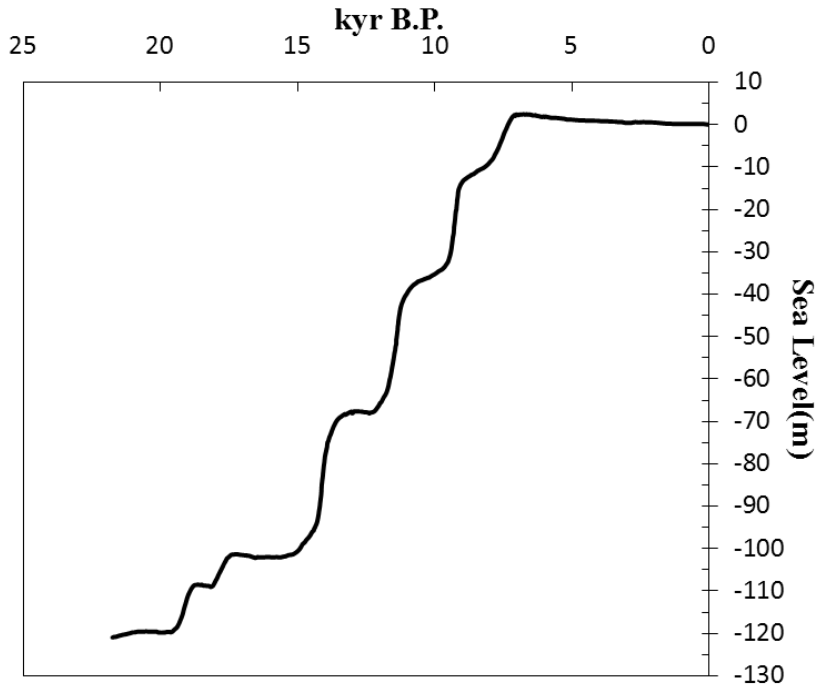

Fig. 2.5 Sea lever change during the last 22,000yr in the Yellow Sea (Park and Khim, 1992; Liu *et al.*, 2004b; Liu *et al.*, 2007a)

Previous studies also show that a major transition occurred between 8.47 and 6.63 kyr, suggesting the establishment of modern circulation patterns in the South Yellow Sea (SYS)(Kim and Kucera, 2000). The benthic foraminiferal, U^{k}_{37} SST, oxygen and carbon isotopic data from the cores revealed three stages of paleoenvironmental development: a low salinity estuarine environment during 8.4-6.9 kyr, a low salinity shallow sea environment at 6.9 to approximately 6-5 kyr, and a modern marine environment after approximately 6-5 kyr (Kim and Kucera, 2000; Xiang *et al.*, 2008).

Though there are many indicators for the paleoenvironment, such as benthic foraminiferal, U^{k}_{37} SST, oxygen and carbon isotopic data, related to the temperature and salinity and oxygen content in the ocean water, but there is no data about the bathymetry and tide evolution over the last 20, 000 years.

Chapter 3 Geological evidence of sediment dynamics

As with many other basin settings, the first-order controls on the formation of the continental shelf as well as the mud deposits are sediment supply and sea level changes over geological time scale. Once sediments are carried past the shoreline, they have the potential of being moved even farther seaward by a combination of marine processes. These range from river plumes, waves, and currents to submarine gravity flows. All of these processes are active in the Yellow Sea and all may have left discernible imprints on the shelf morphology and strata. Therefore, a large number of research have been carried out to understand the origin and dispersal patterns of the Yellow Sea sediments through sedimentological, mineralogical, and geochemical approaches(Shi *et al.*, 2002; Lim *et al.*, 2007; Guo *et al.*, 2010). The published results about the sediment origins, budgets, sediment accumulation rates are abundant but they are not always consistent to each other and sometimes even contradictory (Yang *et al.*, 2003). This chapter will analyse the geological evidence in terms of deposition rate and sediment budget mostly based on the newly available data in order to understand the origin and dispersal systems of the Yellow Sea sediments.

3.1 Depositional rate

The CYSM deposits are considered to have formed under conditions of small changes in sea level, a stable sedimentary environment and continued sediment supply. The geological results indicated that the mud deposits of the CYSM began to accumulate since 10-7 kyr (Liu *et al.*, 2004a; Liu *et al.*, 2007a; Liu *et al.*, 2010).

Table 3.1 Statistics of sedimentation rates for the mid-late Holocene mud deposits (^{14}C dating method). Here, column of mud thickness refers to the deposit since Holocene.

drilling time	*Core name*	*latitude*	*longitude*	*Water depth/m*	*Core length/m*	*Calendar year*	*Dating depth/m*	*Deposition rate(mm/a)*	*Source*
1993	M9-2	38 ?48'	118 ?7'	16.9	4.53	6,105	2.42	0.396	(Liu *et al.*, 2010)
1993	M9-4	38 ?34'	118 ?30'	18.6	6.3	4,312	2.25	0.522	(Liu *et al.*, 2010)
1993	M7-4	38 ?37.92'	119 ?8.02'	27.9	5.5	6,449	2.92	0.453	(Liu et al., 2008a)
1993	M7-6	38 ?24.48'	119 ?29.16'	24.8	4.2	7,989	2.05	0.257	(Liu *et al.*, 2010)
1993	M5-5	38 ?41.4'	119 ?45.66'	22.0	4.3	6,342	2.95	0.465	(Liu et al., 2008a)
1993	M3-3	39 ?12'	119 ?42'	27	3.3	8,747	2.95	0.337	(Liu *et al.*, 2010)
1993	M1-3	39 ?28'	119 ?58'	27.8	4.92	8,134	2.58	0.317	(Liu *et al.*, 2010)
1993	B80	39 ?39'	120 ?23'	30	6.1	7,879	1.85	0.235	(Liu *et al.*, 2010)
1993	B79	39 ?48'	120 ?12'	24	7	6,879	2.95	0.429	(Liu *et al.*, 2010)
2001	HB-1	38 °15'	118 ?55.8'	4.5	61.01	8,838	18.5	2.089	(Liu *et al.*, 2009)
1993	CC02	36 ?7.72'	123 ?49.2'	78	2.78	5,400	0.95	0.176	(Kim *et al.*, 1998a)
1993	CC04	36 ?18'	124 ?30'	83	2.25	10,330	1.1	0.106	(Kim and Kucera, 2000)
1998	B10	35 ?59.7'	123 ?59.6'	80	5.5	10,140	1.8	0.182	(Chen *et al.*, 2003)
2000	EY02-2	34 ?30'	123 ?30'	79	60.415	10,160	2.0	0.133	(Zhuang *et al.*, 2002)
2000	EY02-1	30 ?44'	126 ?34'	90	70.2	8210	8.09	0.99	(Zhuang *et al.*, 2002)
2003	YE-2	35 ?30'	123 ?20'	75	18	8,400	6.1	0.752	(Xiang *et al.*, 2008)
2002	NT1	35 ?26.60'	123 ?24.29'	74.6	70.25	15,600	16.58	1.064	(Wang *et al.*, 2007b)
2002	NT2	33 ?27.54'	122 ?15.5'	35.4	70.45	9,750	2.14	0.466	(Lan *et al.*, 2010)
1995	YSDP102	33 ?49.50'	125 ?45.01'	62	60.6	6400	51.7	8.078	(Park *et al.*, 2000)
1995	YSDP103	34 ?29.24'	125 ?29.2'	53	34.5	13,830	30.0	2.169	(Park *et al.*, 2000)
2006	ZY1	35 ?31'	122 ?55'	70.3	3.95	5,270	3.75	0.67	(Hu *et al.*, 2012)
2006	ZY2	35 ?31'	122 ?39'	69	3.42	5,555	3.295	0.593	(Smith and McLean, 1977)
2006	ZY3	35 ?31'	122 ?27'	56	3.78	6,500	3.59	0.51	(Hu *et al.*, 2012)

drilling time	*Core name*	*latitude*	*longitude*	*Water depth/m*	*Core length/m*	*Calendar year*	*Dating depth/m*	*Deposition rate(mm/a)*	*Source*
1998	YA131	36 °15.0'	123 °55 '	77	3.55	12,520	1.74	0.139	(Liu *et al.*, 2004a)
1998	YA111	36 °17.97'	123 °22.48'	77	3.2	10,540	1.69	0.160	(Liu *et al.*, 2004a)
1998	YA086	36 °52.47'	123 °55.01'	79	3.25	10,170	0.15	0.015	(Liu *et al.*, 2004a)
2006	YS01A	35 °31.2'	122 °29.26'	58.5	30.1	7,383	11	1.49	(Wang *et al.*, 2013)
1993	QC2	34 °18'	122 °16'	49	106.0	9,910	15.05	1.5	(Yang, 1993)
2003	NYS-101	37 °42.23'	122 °48.25'	49	70.2	6,459	4.06	0.628	(Liu *et al.*, 2007a)
2003	NYS-102	37 °55.68'	121 °43.84'	34	70.1	6,747	6.95	1.03	(Liu *et al.*, 2007a)
	G8024	36 °56.3'	123 °3.48'			6,942	1.1	0.2	(Alexander *et al.*, 1991)
	YK07	35 °1'	123 °22.14'	30		6,848	2.5	0.365	(Alexander *et al.*, 1991)
	PK48	31 °46.9'	126 °59.6'			9,447	1.95	0.206	(Alexander *et al.*, 1991)
1996	CY96010	37 °0.6'	123 °45.4'		0.45	66	0.45	6.8	(Yang and Youn, 2007)
1996	CY96008	35 °56.8'	124 °6.12'		0.4	190	0.4	2.1	(Yang and Youn, 2007)
1996	CY96002	34 °55.1'	124 °11.5'		0.39	170	0.39	2.3	(Yang and Youn, 2007)
	EY02-1	30 °44'	126 °34'	90	70.2	8210	8.09	0.99	(Xing *et al.*, 2012)

Sedimentation rates of Holocene deposits were calculated from the slopes of the AMS ^{14}C dating data and sediment depths and listed in Table 3.1.

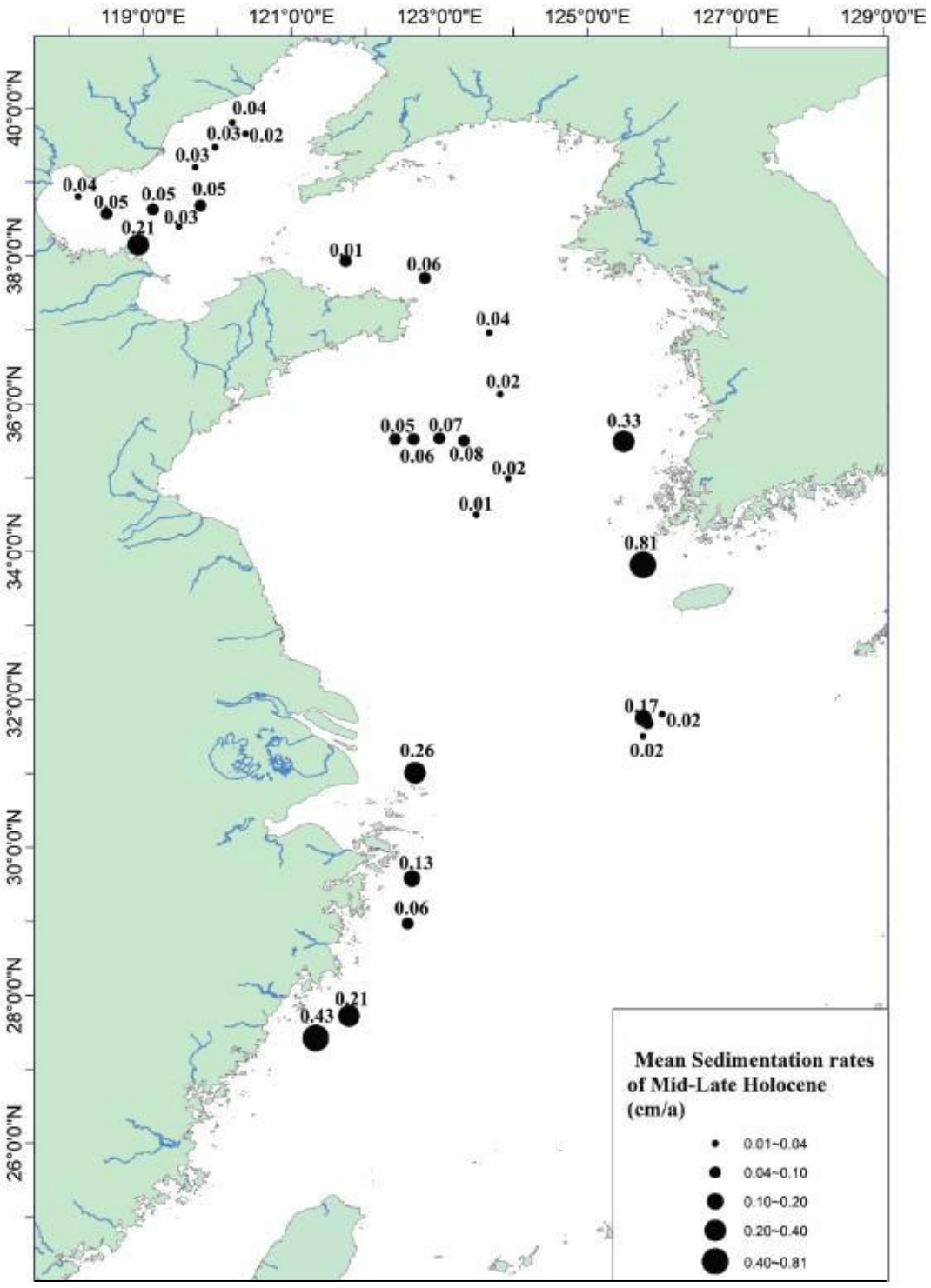

Fig. 3.1 Average sedimentation rates of Holocene

Fig. 3.1 showed that in 1000 years scale (derived from AMS ^{14}C dating data). It is distinctive that the sedimentation rates are relatively lower in the central part than in

the western region of the CSYS(Yang and Youn, 2007). The average rate Holocene sedimentation is 0.01-0.08cm/a and slightly decreased from the northwest to southeast with minimum sedimentation rate in the central SYS mud area. The central southern yellow sea mud deposition rate is less than 1mm/yr, much lower than the southeastern yellow sea mud (8mm/yr).

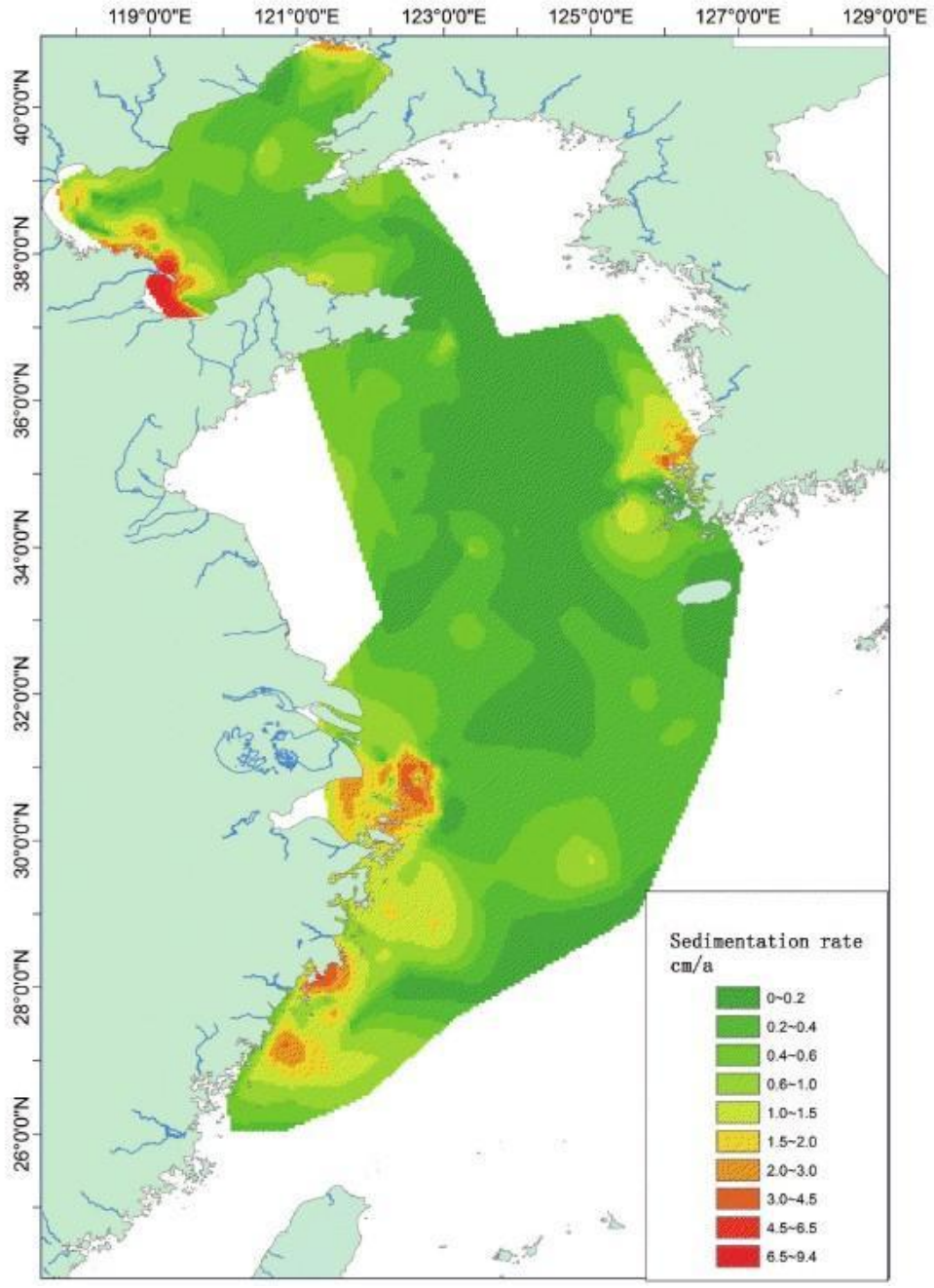

Fig. 3.2 Modern (<100a) depositional rate distribution in the BYECS

This sedimentation rate is much lower than those estimated in the nearby mud

deposits derived from the ^{210}Pb method (in 100 years scale) for sedimentation rate estimation (Fig. 3.2). ^{210}Pb date suggested that the modern sedimentation rate at the center of SYS is about 0.2cm/yr whereas the ^{14}C method showed the sedimentation rate of Holocene is 0.0176cm/yr.

It is suggested that radiocarbon measurements are more accurate for determining sedimentation rates than the ^{210}Pb method because the ^{210}Pb method can only reflect the surface sedimentation rate over the recent 100 years and is influenced predominantly by biological deep mixing (Harden *et al.*, 1992). Therefore, the sedimentation rates determined by ^{210}Pb are more likely to be an overestimation.

3.2 **Sediment budget**

The Central Yellow Sea Mud (CYSM) deposit located in the in the centre of the South Yellow Sea, where water depth locally exceeds 70m, is about 6.1×10^4 km^2 in area (Fig. 3.3). Fig. 3.3 shows different sediment budgets results from previous studies on 100-year time scale. The significant difference of annual CYSM deposition amount (3.0×10^8tons/year ~<0.6×10^8tons/year) is mainly caused by different scopes of CYSM chosen by different researchers. Furthermore, on a larger time scale (1000years), the CYSM deposition rate would be different, and so is the sediment budget such as river discharges.

Fig. 3.3 A schematic map of sediment budgets.
including the sediment discharges from major rivers in China and Korea, their dispersal directions, and annual sediment budgets of the major sedimentary bodies in the Yellow Sea. Question marks in the map mean that there are uncertainties or arguments for the meaning of the arrows. The numbers in the ellipses indicate sediment discharges of rivers and sediment yields or transports while the paned numbers represent different opinions on sediment deposition rate (on 100-year time scale). Unit of the numbers is 10^8tons/year (Yang *et al.*, 2003)

In this study, the scope of CYSM is bounded based on the sediment grain size distribution in the Yellow Sea, shown as the area with red line boundary in Fig. 3.6 .

The volume of CSYM mud deposit is calculated mainly based on the high-resolution Chirp sonar profiles, which were acquired using Edgetech 512i in 2005, as shown in Fig. 3.4 and Fig. 3.5 for instance.

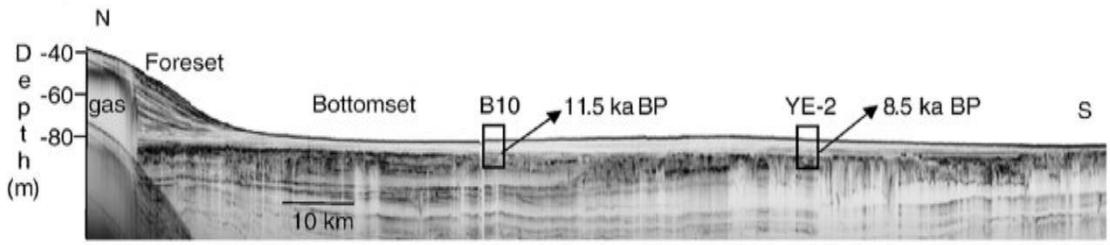

Fig. 3.4 Chirp sonar profiles along 123 ℉, the vertical green line in Fig. 3.6(Yang and Liu, 2007)

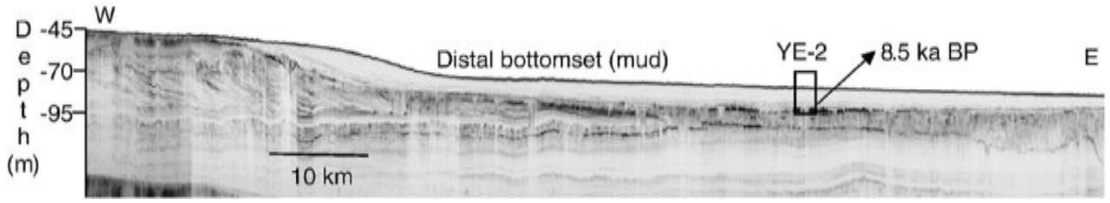

Fig. 3.5 Chirp sonar profiles along 35 ℉27'N, the horizontal green line in Fig. 3.6(Yang and Liu, 2007)

The approximately 1600 km of high-resolution seismic profiles revealed sediment depth of a unique Huanghe River-derived, subaqueous deltaic lobe deposited around the eastern tip of the Shandong Peninsula with 40m thick in the centre (Fig. 3.6) (Yang and Liu, 2007), indicating that the Huanghe River discharged sediments could reach 80 m water depth in the centre of the South Yellow Sea, 700 km away from the river mouth. And the isolines of the Holocene mud thickness were then adjusted by the cores (blue dots in Fig. 3.6) Holocene depth from Table 3.1. If the age at the core bottom is less than 9,000 years, the Holocene depth is calculated by multiplying the deposition rate by 9,000 years.

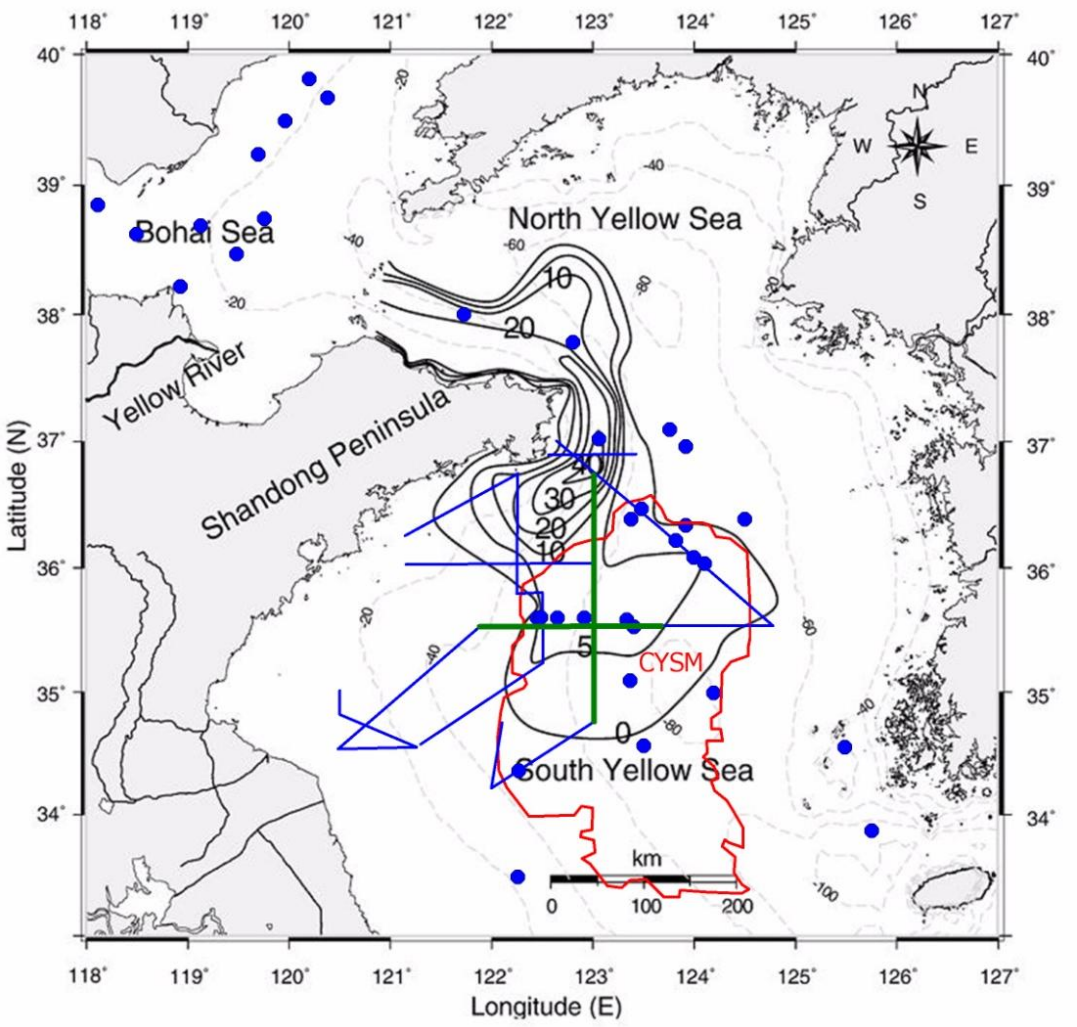

Fig. 3.6 Isopachmap of the Holocene mud in the North and South Yellow Sea, modified from (Yang and Liu, 2007)

The volume is then roughly calculated according to the modified sediment thickness of the mud distribution. The total sediment volume of the CYSM is about 2.7×10^{11} m^3, assuming the dry bulk density was 1200 kg/m^3. The total accumulation in mud deposit since 9.0 ka can be estimated as 3.26×10^{11} t with average deposit of 3.6×10^{7} t a^{-1}.

There are mainly three origins of the silt-clay sediment of the CYCM, which are: the present river mouths of the Huanghe and the Changjiang and the old river mouth of the Huanghe off the Seibei coast.

3.2.1 **Huanghe River sediment discharge**

Huanghe River, regarded as the second largest river of the world in terms of sediment loads, has discharged sediments up to 7.78×10^8 tons (Chinese Rivers Sediment Bulletin) or 1.08×10^9 tons (1950-1980)(Milliman and Meade, 1983) annually, about one third of which is deposited at the onshore delta, while the other two thirds is transported to coastal areas and the Bohai Sea (Pang and Si, 1980; Wu *et al.*, 1994). Approximately 70% of sediment transported to coastal areas is deposited in the subaqueous delta region (Qin and Li, 1983).

The Huanghe River changed path frequently and produced many superlobe (Fig. 3.7). The Huanghe River discharged directly into the South Yellow Sea during 9.5-7 ka B.P and form superlobe 1 offshore the Jiangsu with volume of 200 km^3, corresponding to 240 $\times10^9$ t (sediment density of 1,200 kg/m^3). The annual mass accumulation rate would be 0.16×10^9t/year, assuming superlobe 1 represents 1,500 years of deltaic sedimentation from the Huanghe River, which agrees closely with inferred Huanghe River sedments fluxes prior to agricultural activity on the loess plateau of northern China (Milliman *et al.*, 1987).

Since its northward shift around 7.5-7 ka, the Huanghe River had been discharging into Bohai Sea until 1,128 A.D and formed at least eight superlobes (lobes 2-9) with total sediment volume/mass of 500 km^3/600×10^9t, corresponding to a minimum annual accumulation rate of 0.1×10^9 t/year (Table 3.2).

The Huanghe River shifted its path completely south of the Shandong Peninsula into the Southern Yellow Sea in 1128AD and stayed there for 728 years. The corresponding lobe 10 deposited about 250 km^3 sediments along the Jiangsu Coast, which equates to an annual sediment load of 0.43×10^9 t/year, indicating enhanced erosion form agricultural activity in the loess hills of northern china. The last shift

back to the Bohai Sea occurred in 1, 855 A.D and formed lobe 11 with sediment volume/mass of 108 km^3/130×10^9 t.

Table 3.2 Huanghe derived superlobe sediment volume, mass and accumaltion in the Bohai and Yellow Sea during Holocene

	9-7.5 ka BP South Y.S (lobe1)	7.5-1 ka BP Bohai Sea (lobe2-9)	1128-1855AD Soth Y.S. (lobe 10)	1855AD-present Bohai Sea (lobe 11)
Volume(km^3)	200	500	250	108
Mass (t)	240×10^9	600×10^9	300×10^9	130×10^9
Accumulation rate(t/year)	0.16×10^9	0.1×10^9	0.43×10^9	0.9×10^9

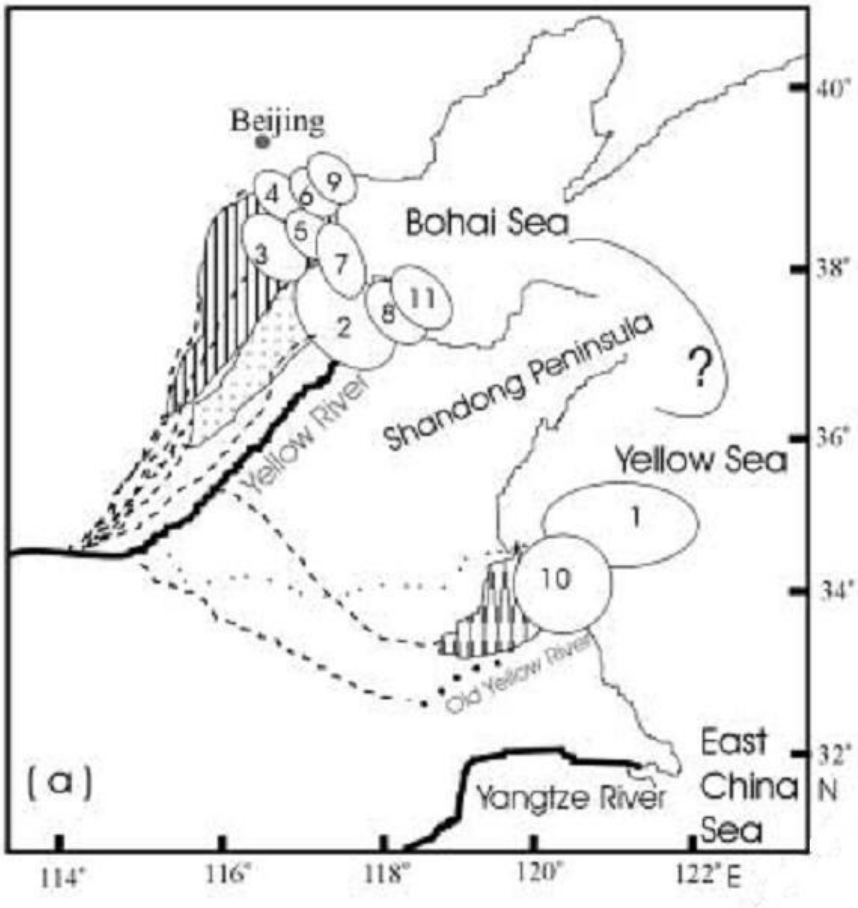

Fig. 3.7 Historic N-S shifts of the Huanghe River's course.
Where the question mask (?) represents the Shandong Mud Wedge. Superlobe age (1) 9.0-7.5 ka B.P (2) 7.0-5.0 ka B.P (3) 5.0-4.5 ka B.P (4) 4.5-3.4 ka B.P (5) 3.4-3.0 ka

B.P (6) 3.0-2.5 ka B.P (7) 602 B.C.-11A.D. (8) 11A.D.-1048A.D. (9) 1048 A.D.-1128A.D. (10) 1128 A.D.-1855A.D. (11) 1855 A.D.-Present (Liu *et al.*, 2002).

The estimated sediment load at Sanmenxia station in the middle reach of Huanghe was 2.7–4.0 $\times 10^8$ tons/year 1000 years ago, about 20% (15–25%) of the recent high level (10×10^8 tons/year during 1000-1900 AD.). The sediment discharge of Huanghe before 1000 years ago is estimated to have been 1×10^8 tons/year, as little as 1/10 of the recent high level, based on the sediment volume of prograding deltaic sediments over the last 6000 years (Saito *et al.*, 2001; Liu *et al.*, 2002). An abrupt increase occurred at ca. 1000 years ago as a consequence of human activities, especially involving cultivation and deforestation (Table 3.2& Fig. 3.8).

The up-to-date dataset (1950–2005) recorded at four gauging stations in the upper, middle, and lower reaches of the Huanghe River revealed that the annual sediment load reaching the sea is only 3.0×10^8 tons/yr during 1990-2005 (Liu *et al.*, 2011), less than one-third of that estimated by Milliman and Meade (1983). Particularly, in the most recent years (2000–2005), the Huanghe discharged only 1.5×10^8 tons/yr of sediment loading to the Bohai Sea, reverting to its pristine levels of the middle Holocene, prior to human intervention (Milliman *et al.*, 1987; Saito *et al.*, 2001; Wang *et al.*, 2007a).

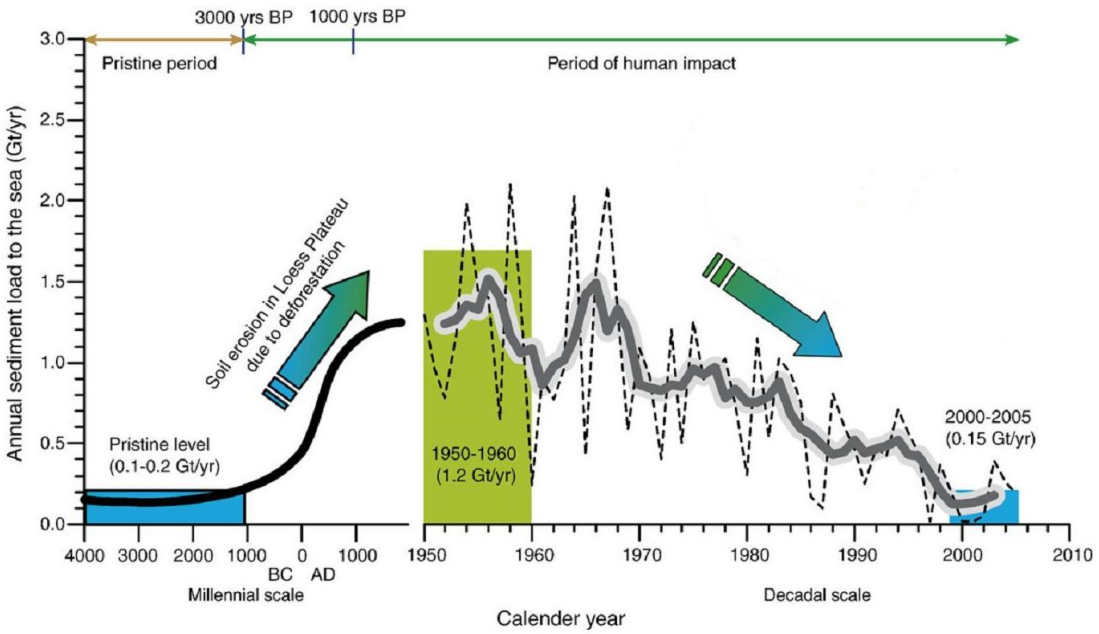

Fig. 3.8 Past and present sediment load discharged from the Huanghe River to the sea (Wang *et al.*, 2007a).

The budget of Huanghe River discharged sediment transported out of Bohai Sea is also controversial (Table 3.3).

Table 3.3 Yellow River discharged sediments transported into the Yellow Sea

author	Yellow sea sediment	method
(Alexander *et al.*, 1991)	9-15%	^{210}Pb sediment rate &sonar data
(Martin *et al.*, 1993)	1%	Field SSC in 8 cruises
(Liu *et al.*, 2004a)	30%	Core ^{14}C & sonar profile data
(Bi *et al.*, 2011)	4%	Filed SSC 2 cruises& MODIS
(Lu *et al.*, 2013)	30%	Numerical result

The sediment budget, calculated by Alexander *et al*. (1991), demonstrates that 9-15% of the annual Huanghe discharge is accumulating in the Yellow Sea on the basis of ^{210}Pb sediment accumulation rate data. About two-thirds of this sediment is accumulating in the topset, foreset and proximal bottomset deposits of the Shandong

subaqueous delta, with the remaining third transported further southward and deposited in the central Yellow Sea.

Whereas Martin *et al.*(1993) indicated that more than 90% of the Huanghe sediment load is deposited in the lower reaches of the river and within the shallow estuarine area. Additional sedimentation occurs in the southern part of Bohai so that the actual sediment flux dispersed into the Yellow Sea was very limited. It is showed that this flux takes place via a nepheloid layer across the Bohai Sea strait, transporting about 6×10^6 tons/year, less than 1% of the Huanghe sediment discharge, based on measurements from 8 cruises during 1985-1991. However, the cruises only had nine stations, about three in each section in the Bohai Sea. Moreover, each cruise lasted for about 2 days, mostly under very calm weather. Therefore, the representativeness of these 8 cruise measurements for the whole year is questionable.

Bi *et al*.(2011) investigated the seasonal variation of suspended-sediment transport in the southern Bohai Strait, based on field observations made in winter 2006 and summer 2007 and on multiscene MODerate resolution Imaging Spectrometer (MODIS) imagery. The field observations in two different seasons established an exponential empirical model to retrieve suspended-sediment concentration (SSC) from MODIS imagery. Both the field-survey data and the MODIS-derived SSC showed that the sediment transport in the southern Bohai Strait has a significant seasonal variation. The SSC in winter is approximately 3-10 times higher than in summer. The annual suspended sediment flux (SSF) through the southern Bohai Strait is estimated to be approximately 40×10^6 tons/year, considering the seasonal SSC variation (4% of the Huanghe sediment annual discharge), about 4-8 times previous estimates, which did not take into account seasonal variation. The strong seasonal variability of SSF through the southern Bohai Strait indicates that strong resuspension

along the coast of the Huanghe delta in winter and enhanced longshore transport by coastal currents due to winter monsoon activity.

Though most of Huanghe River derived sediment (>90%) appears to temporarily remain trapped within the modern deltaic system as mentioned above, yet extensive geological and geophysical surveys conducted in the North and South Yellow Sea reveal a prominent mud wedge that extends southward from the eastern tip of the Shandong Peninsula (Alexander *et al.*, 1991; Liu *et al.*, 2004a), which has been deposited mainly by the resuspended Huanghe River sediments carried down by the coastal current (Fig. 3.9).

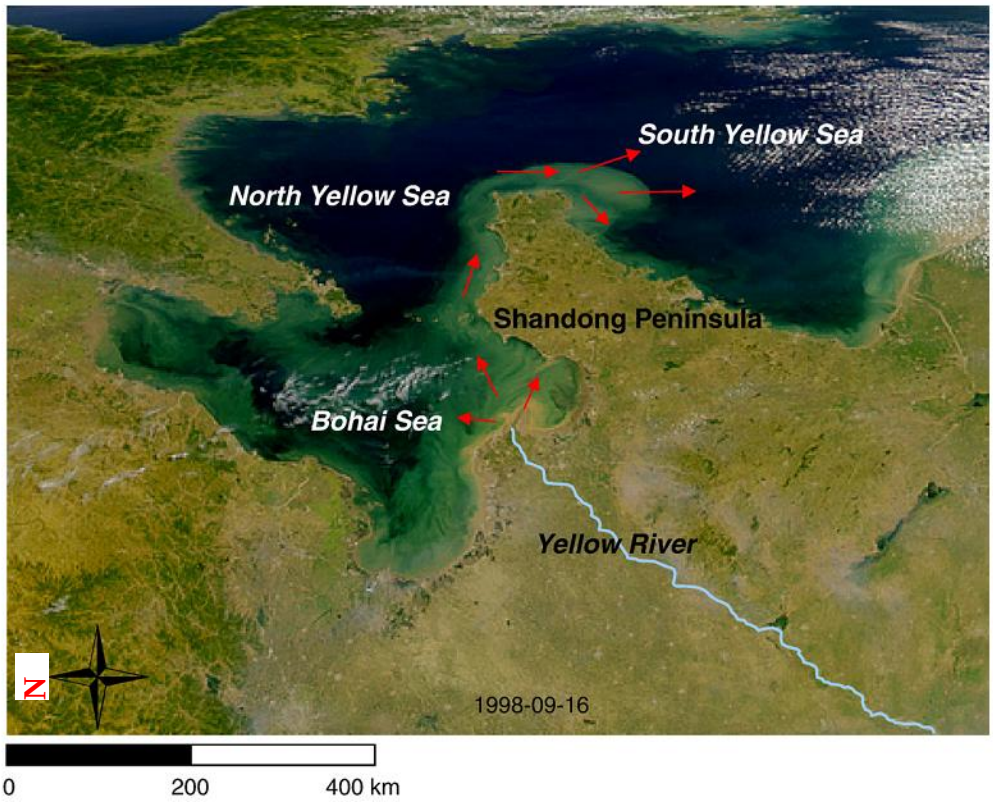

Fig. 3.9 A NASA satellite image (06 Sep 1998) shows the Huanghe river- derived sediment plume transports into the North and South Yellow Sea along the Shandong Peninsula coast

Radiocarbon 14 dates from the underlain pre-Holocene and transgressive sediments indicate this distal lobe has formed since the middle-Holocene highstand under a relatively stable sea level. The quantitatively analysed sediment distribution in

the Yellow seas indicate that nearly 30% of the Huanghe River derived sediment has been resuspended and transported out of the Bohai Sea into the Yellow Sea over the past 7000 years (Liu *et al.*, 2002; Liu *et al.*, 2004a), which is significantly larger than the 1% given by Martin *et al*.(1993).

The suspended sediment fluxes (SSF) and distribution in different areas for the Huanghe River derived sediment was estimated quantitatively by a numerical sediment transport model, embedded into a coupled wave-tide-circulation model (Lu *et al.*, 2013). The SSF results across the Bohai Strait and the 37° N section demonstrated that about 70 % of the total discharged Yellow River sediments are deposited in the Bohai Sea, 14.1 % in the North Yellow Sea, and 13.9 % in the South Yellow Sea. There are two deposition branches in the Yellow Sea. The primary one is located off the eastern tip of the Shandong Peninsula and extends to the southwest off the coastline, which is consistent with the observed "Ω"-shape deposition pattern. This simulated tongue shape deposition pattern is isolated from the north by the strong resuspension off the eastern tip of Shandong Peninsula. The secondary branch extends to the middle of the South Yellow Sea.

3.2.2 **Old Huanghe River delta**

The abandoned Huanghe subaqueous delta off the Subei coast is also an important source of the fine-grained sediment in the mud deposit area. Especially in winter storm, much sediment was eroded and then transported southward by the tide and by currents in the Yellow Sea and East China Sea to the mud deposit area (Fig. 3.10). Its load is nearly the same as that from the Changjiang (Milliman *et al.*, 1985). However, most of Changjiang sediment is trapped and transport southward, only a very small proportion can be transported into the Southern Yellow Sea mud area. Thus the sediment resuspension of the Old Huanghe River delta in winter is far more important

than that discharged from Changjiang River in terms of the contribution to the SYS mud formation.

It has been shown that only 0.2×10^{8}~0.3×10^{8} t/year suspended particles are carried to the East China Sea. They are chiefly resuspended sediment from erosion of the coast and subaqueous delta of the abandoned Huanghe River.

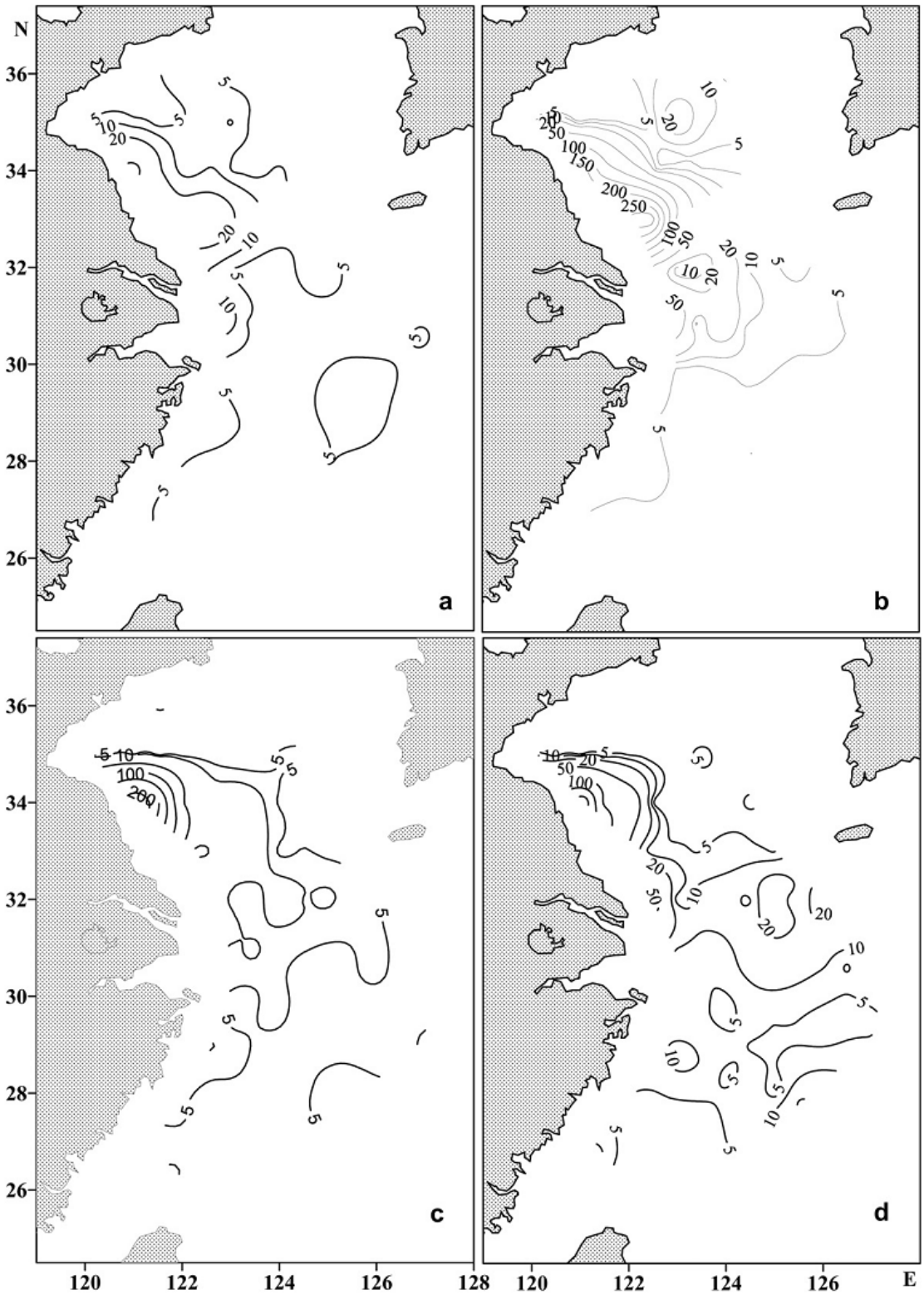

Fig. 3.10 SSC distribution in the Yellow Sea and East China Sea (mg/l).

(a) SSC in the surface layer during 19/10/2000-29 /10/ 2000, (b) SSC in the bottom layer during 19/10/2000-29 /10/ 2000, (c) SSC in the surface layer during Cruise no.2 (26 Mache23 April 2001), (d) SSC in the bottom layer during Cruise no.2(Dong *et al.*, 2011)

However, there are still no field time-series hydrodynamic observations related to winter storms that have been reported, even though they are considered essential for understanding sediment dynamic processes in the study area.

3.2.3 **Changjiang River sediment discharge**

Historically the Changjiang River discharged 5 x 10^8 tons/year of sediment to the East China Sea based on data collected at the Datong Hydrological Gauging Station over the recent 100 years.

Multiple geological and geophysical studies have been carried out at the Changjiang river mouth and adjacent inner shelf to examine the sediment transport patterns. Recent high-resolution seismic profiling and coring in the inner shelf of the East China Sea has revealed an elongated (~800 km) subaqueous deltaic deposit extending from the modern Yangtze River mouth south toward the Taiwan Strait. The centre of this remote deposition has been located on the inner shelf about 400 km south of the river mouth (Fig. 3.11).

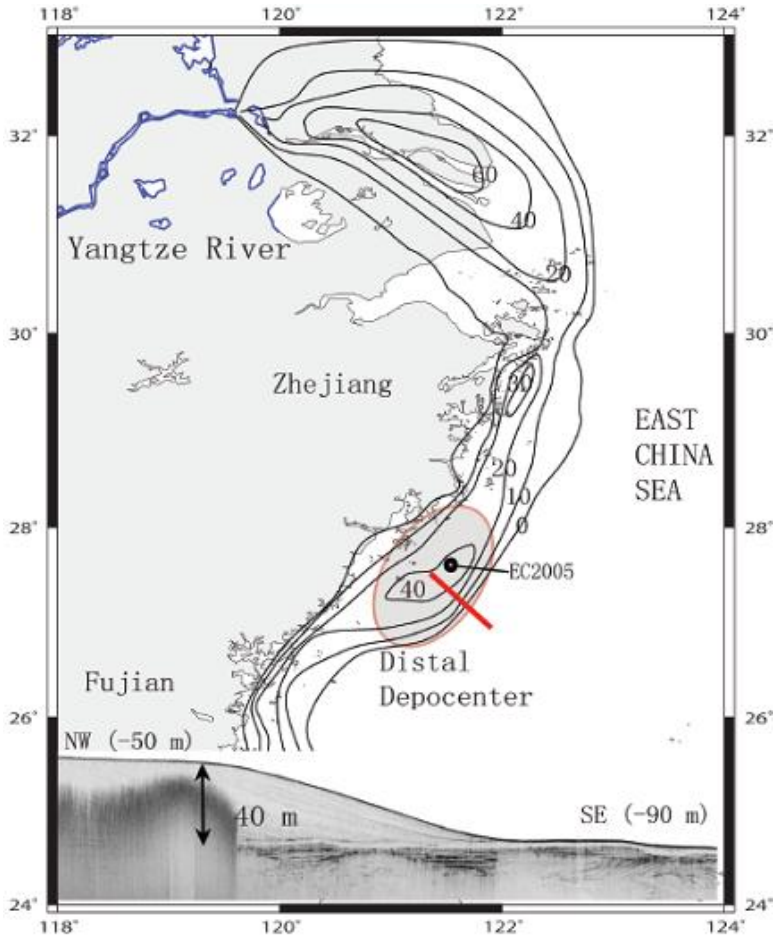

Fig. 3.11 Isopach (in meters) map of Changjiang River-derived sediment discharged to the sea.
A select seismic profile (red line) across the remote nearshore depocenter is also shown (Liu *et al.*, 2007b). A deep sediment core (EC2005) drilled in 2005 has verified the mud's thickness and age (Xu *et al.*, 2009).

The annual fresh water discharged into the East China Sea is as high as $9\times10^{11}m^3$, which is only 1/10 of the annual tidal prism ($84\times10^{11}m^3$) from the sea into the estuary (Chen *et al.*, 2001). Thus the dispersal pattern of the Changjiang derived sediment has been influenced significantly by the local semi-diurnal tidal cycles.

Under the effects of strong tides, waves, winter storms, coastal currents such as the southward-flowing China Coastal Current, the northward-flowing Taiwan Warm Current, and the Kuroshio Current, most of the Changjiang derived sediment is trapped in the inner shelf and transported southward.

AMS^{14}C dates suggest that the Changjiang derived sediment began to be

transported southward after the middle Holocene sea-level highstand, around 7000 yrs BP when the East China Sea current circulation was formed.

It is suggested that sediment distribution is associated with the coastal upwelling system. Especially in winter, monsoon-driven coastal currents flow southward and cause downwelling in nearshore, while the northward Taiwan Warm Current causes upwelling. With the two vertical circulation cells (downwelling near the coast and upwelling offshore) fine sediment transport is constrained under the upwelling (Fig. 3.12).

It is estimated that the sediment discharge of Changjiang before 2000 years BP was about 2.4×10^8 tons/year, only 50% of present level.

The Changjiang River derived sediment contribute little in terms of Southern Yellow Sea Mud formation, as most of them are trapped and transport southward, only a very small proportion can be transported to the Southern Yellow Sea mud area.

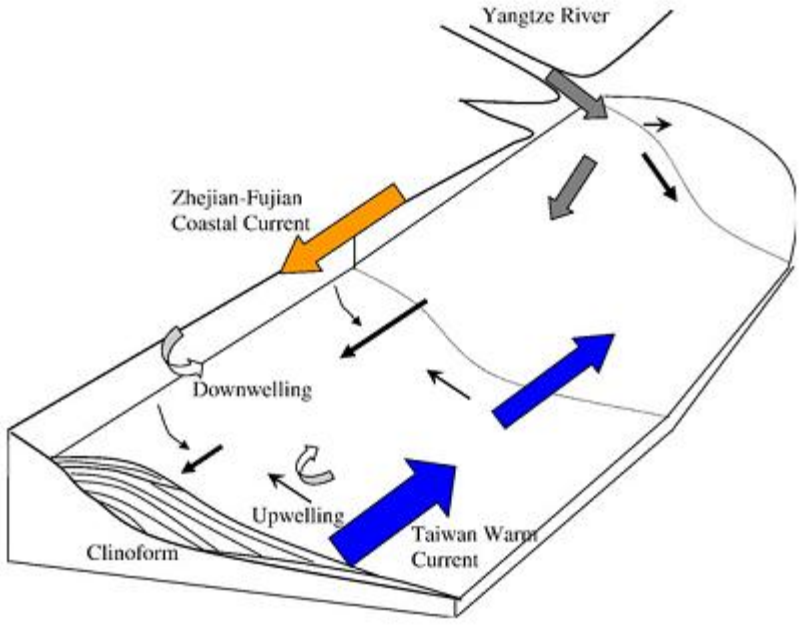

Fig. 3.12 Oceanographic processes affecting the Changjiang-derived sediment dispersal at both across and along self dierctions (Liu *et al.*, 2007b)

Summary: The fine sediments discharged from Huanghe River, the resuspended sediments of Old Huanghe Delta and the Changjiang River derived sediments are the main sources for the mud deposit at the Southern Yellow Sea, a conclusion that appears to be supported by all sedimentological, mineralogical, and geochemical and hydrodynamic modelling evidence. Among the three main sources, the relative contribution to the sediment loading are about 60-70%, 30-25%,10-5% respectively based on the provenance literature results. The average deposition rate at the Central Yellow Sea mud patch from the three sources is calculated to be about $3.6 \times 10^{7} t\ a^{-1}$, based on high-resolution Chirp sonar profiles combined with analysis of the available cores samples. The geological method only shows the present state resulted from thousands of the years, but can not tell much about how to evolve over the geological time and the process to affect its evolution, which can be investigated by numerical approach.

Chapter 4 Numerical model development

The fate of sediment dispersed from the river into the coastal ocean involves at least four processes: supply via plumes, initial deposition, re-suspension and transport by marine processes, and long-term net accumulation (Wright and Nittrouer, 1995). The Yellow River-derived suspended sediment plume, whose sediment is carried down the dispersal system by several cycles of transport, deposition and re-suspension under intense tidal, wave and coastal conditions. Important mechanisms that influence across-shelf transport include tidal flows, wind-driven flows, surface waves, internal waves, infragravity phenomena, buoyant plumes, and surf zone processes (Nittrouer and Wright, 1994). The complex and highly variable marine environment makes it difficult to quantify these parameters. In most coastal seas, tide-induced and wave-induced bottom stresses, as well as stratification, act as the main physical factors to control sediment resuspension either one or together (Scully and Friedrichs, 2003). Bottom boundary layer dynamics is one of the most critical small-scale processes controlling sediment transport. Successful modelling of sediment transport patterns mainly depends on some critical parameters such as bottom stress and settling velocity(Guillén *et al.*, 2001; Curran *et al.*, 2007). However, it is very challenging as highly small scale nonlinear turbulent flow phenomenon are involved (Ozdemir *et al.*, 2010).

The influencing factors mentioned above will be investigated individually by an open source numerical model MITgcm (MIT General Circulation Model). Considering the important role of wave in sediment transport in the shallow Yellow Sea especially during winter, it is necessary to couple it with a wave model (SWAN). The model needs to be modified in order to study the sediment transport. Thus, a

wave module, a bottom boundary layer module and a sediment module will be embedded into the MITgcm (Fig. 4.1).

Scenario-based numerical experiments will be carried out to investigate the hydrodynamic and sediment transport in the southern Yellow Sea.

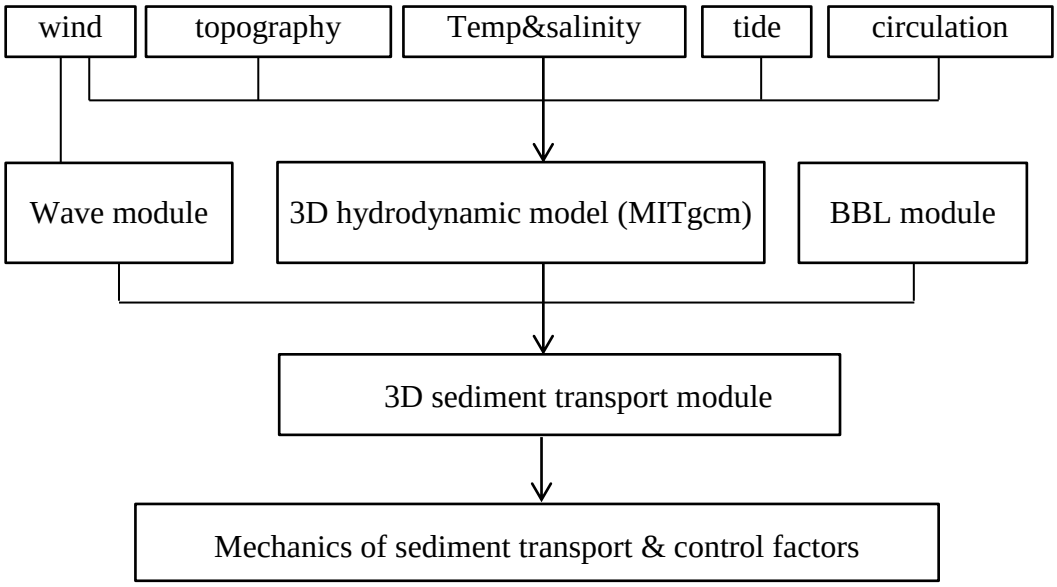

Fig. 4.1 Schematic outline of the model.

4.1 **MIT General Circulation Model (MITgcm)**

The coordinate system applied here is shown in Fig. 4.2. The x direction is from west to east, the U velocity is positive eastwards, y direction is from south to north, the V velocity is positive northwards, and vertical z is upwards, the W velocity is positive upwards, and the still water level is 0m.

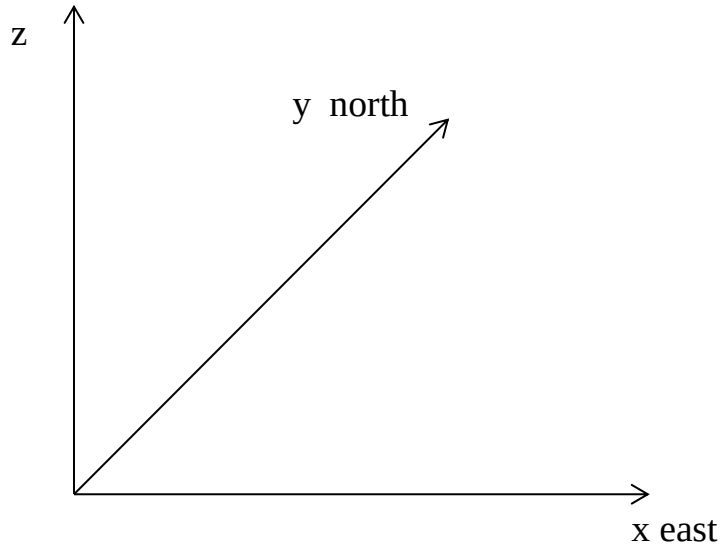

Fig. 4.2 Sketch of coordinate system

4.1.1 **Equations of motion**

Applying the laws of classical mechanics and thermodynamics to a Boussinesq, Navier-Stokes fluid, the governing equations are obtained as follows.

$$\rho\frac{D\vec{u}}{Dt}+\rho 2\overline{\Omega}\times\vec{u}=-\nabla p+\rho\vec{g}+\mu\nabla^2\vec{u} \qquad \text{momentum} \qquad (4.1)$$

$$\frac{1}{\rho}\frac{D\rho}{Dt}+\vec{\nabla}\cdot\vec{u}=0 \qquad \text{continuity} \qquad (4.2)$$

$$\frac{DT}{Dt}=k_T\nabla^2T+Q_T \qquad \text{temperature} \qquad (4.3)$$

$$\frac{DS}{Dt}=k_S\nabla^2S+Q_S \qquad \text{salinity} \qquad (4.4)$$

$$\rho=\rho(S,T) \qquad \text{equation of state} \qquad (4.5)$$

where $\vec{u}(x,y,z,t)=(U,V,W)$ is the velocity field, ρ is the density, $\vec{\Omega}=(0,\Omega\cos\varphi,\Omega\sin\varphi)$ is the forces due to earth rotation, where φ is latitude, p is the pressure, $\vec{g}=(0,0,-g)$ is the gravitational acceleration constant; μ is the coefficient of

dynamic viscosity, T is the temperature, κ_T is the thermal diffusivity, Q_T is temperature source, S is the salinity, κ_S is the coefficient of salt diffusion, Q_S is salinity source.

$\nabla = \frac{\partial}{\partial x} + \frac{\partial}{\partial y} + \frac{\partial}{\partial z}$ is the vector differentiation operator .

and $\frac{D}{Dt} = \frac{\partial}{\partial t} + \vec{u} \cdot \vec{\nabla}$ is the material derivative.

Equation (4.1) is the momentum equation. The first term on the left hand side is the rate of change of velocity of a fluid particle; the second term is the Coriolis force that accounts for the effects of rotation. On the earth, corresponding to one rotation every 24 hours

$$\vec{\Omega} = \frac{2\pi}{24 \times 60 \times 60} \approx 0.727 \times 10^{-4} \text{rad } s^{-1}$$

On the right hand side, the first term is the pressure gradient, a vector field resulting from the gradient operator acting on the scalar pressure field. The second term is gravitational acceleration and only acts in the vertical direction while the third accounts for viscosity that acts to dissipate small scale motion at molecular length scales.

Equation (4.2) is the continuity equation meaning mass conservation. A net flow of fluid into or out of a fixed volume must be associated with a corresponding change in density, in the absence of any mass sources or sinks.

Equation (4.3) states the energy equation. The first term of right side is temperature dissipation and the second is heat source.

Equation (4.4) is the salt conservation equation. Similarly, the first term of right side is salt dissipation and the second is salinity source.

Equation (4.5) is the equation of state that relates density ρ to the active tracers T and S. The linear equation of state is applied here.

$$\rho(T,S) = \rho_0(1-\alpha(T-T_0)+\beta(S-S_0)) \tag{4.6}$$

The reference density ρ_0 = 1028 kg m^{-3}, corresponding T_0= 10°C and S_0 = 35 psu, α =1.7 × 10^{-4} °$C^{-1}$is the thermal expansion coefficient and β = 7.6 × $10^{-4}$$psu^{-1}$is the haline contraction coefficient.

4.1.2 **Kinematic boundary condition**

At the sea surface z=η, the vertical velocity *w* is the time derivative of sea surface height.

$$W_s = \frac{d\eta}{dt} = \frac{\partial\eta}{\partial t} + (U\frac{\partial\eta}{\partial x} + V\frac{\partial\eta}{\partial y})_s \tag{4.7}$$

Then

$$\frac{\partial\eta}{\partial t} = w_s - (u_s\frac{\partial\eta}{\partial x} + v_s\frac{\partial\eta}{\partial y}) \tag{4.8}$$

In which η is water elevation and subscript *s* represents sea surface

At ocean bottom, the vertical velocity W=0.

4.1.2.2 Horizontal

$$\vec{u}\cdot\vec{n} = 0 \tag{4.9}$$

Here $\vec{n}$ is the normal to a solid boundary.

The MITgcm provides several choices of boundary conditions. At the surface boundary, one can choose between a rigid lid condition and an implicit free surface condition. At solid boundaries (bottom and walls), one can choose between free-slip and 'no-slip' conditions. The 'no-slip' condition is not literally no-slip; it is

implemented via a drag force imposed on the flow. It is also possible to use quadratic bottom friction as Equation (4.10) shows. It has possibility for more sophisticated open boundary conditions.

$$A_v(\frac{\partial u}{\partial z})_b = \tau_b^x = F_c u_b \sqrt{u_b^2 + v_b^2}$$
$$A_v(\frac{\partial v}{\partial z})_b = \tau_b^y = F_c v_b \sqrt{u_b^2 + v_b^2} \quad (4.10)$$

A_v is vertical viscosity coefficients. Here at ocean bottom, the drag force on unit square meter is equal to the shear stress τ**,** subscript *b* represents ocean bottom. F_c is the friction coefficient.

4.1.3 **Forcing**

The ocean model can be forced by, for example, a prescribed wind field or heat flux at the surface, via open boundaries or through a coupling with an atmosphere simulation.

At the sea surface z= η, the wind stress provides force as below

$$A_v(\frac{\partial u}{\partial z})_s = \tau_s^x = \rho_a C_D W_x \sqrt{W_x^2 + W_y^2} / \rho_s$$
$$A_v(\frac{\partial v}{\partial z})_s = \tau_s^y = \rho_a C_D W y_x \sqrt{W_x^2 + W_y^2} / \rho_s \quad (4.11)$$

in which subscript *a* represents air, C_D is the wind drag coefficient. W_x, W_y are wind vector in the x and y direction.

At the sea surface z=η, the temperature change is ascribed to the heat flux between the sea surface and air as

$$\rho C_p \left(\frac{\partial T}{\partial z}\right)_s = Q \quad (4.12)$$

in which C_p is specific heat capacity constant-pressure, Q is the net heat flux (positive when ocean losing heat), and sea surface salinity change is caused by precipitation and evaporation, as shown in Equation (4.13)

$$\rho\left(\frac{\partial S}{\partial z}\right)_s = Q_s \tag{4.13}$$

where Q_s is effective salinity flux.

4.1.4 **Spatial Discretization**

Spatial discretization is carried out using the finite volume method (Marshall *et al.*, 1997a). It can have embedded or intersecting boundaries (shaved or lopped cells). This amounts to a grid-point method (namely second-order central finite difference) in the fluid interior but allows boundaries to intersect a regular grid allowing a more accurate representation of the position of the boundary.

The basic algorithm applied for stepping forward the momentum equations is based on retaining non-divergence of the flow at all times. This is most naturally done if the components of flow are staggered in space in the form of an Arakawa C grid (Arakawa and Lamb, 1977). And, spherical, orthogonal and curvilinear coordinates are supported.

Fig. 4.3 shows the components of flow (U,V,W) staggered in space (Arakawa C grid) such that the zonal component falls on the interface between continuity cells in the zonal direction, similarly for the meridional and vertical directions. The continuity cell is synonymous with tracer cells (they are one and the same), and temperature (T), salinity (S), density (ρ), pressure (P) are defined in the centre of grid cell.

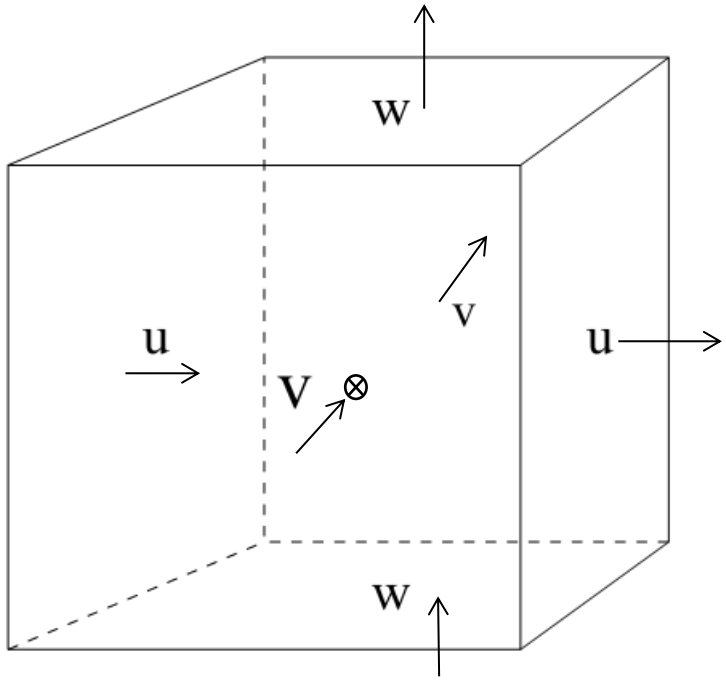

Fig. 4.3 Three dimensional staggering of velocity components. This facilitates the natural discretization of the continuity and tracer equations.

Fig. 4.4 shows the horizontal grid distribution. The symbol P represents temperature (T), salinity (S), density (ρ), pressure (P), i and j are index of x and y direction, i increases from west to the east and j increases northwards. The U and V velocities are defined on the west and south of P with the same index respectively.

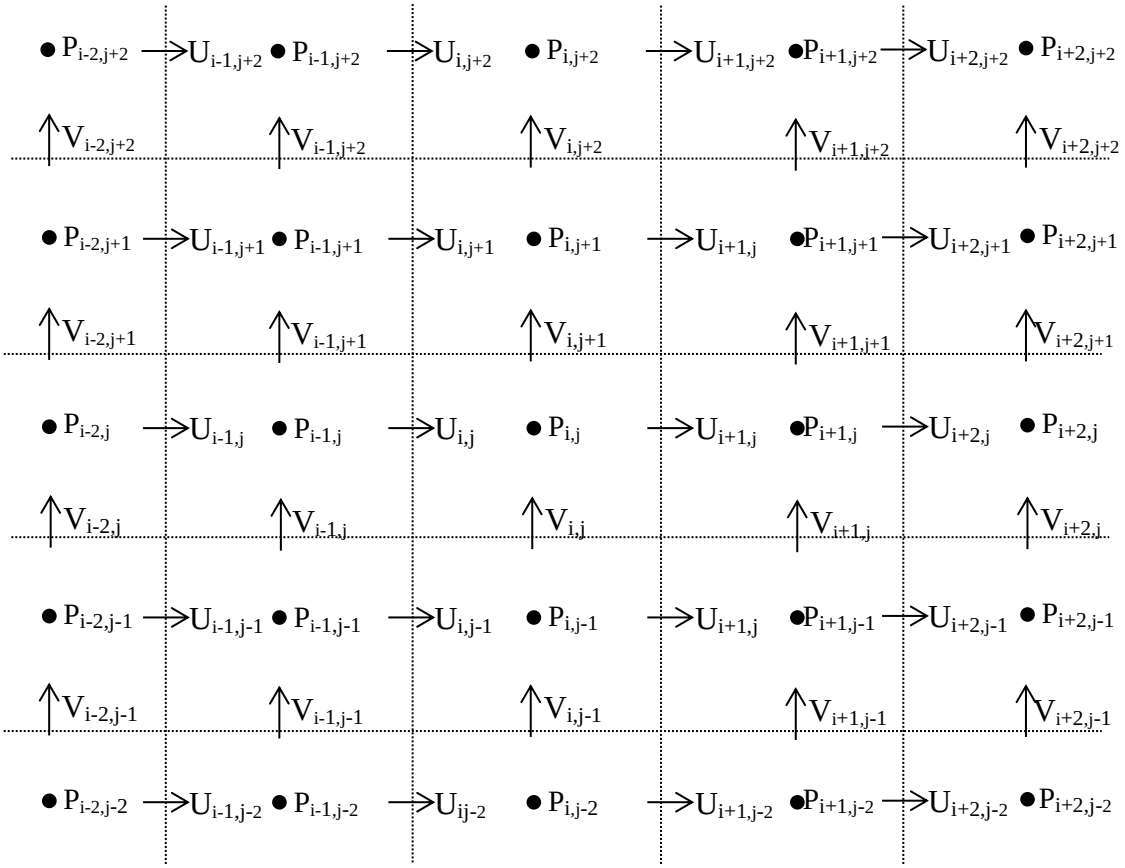

Fig. 4.4 The horizontal grid sketch

As in most ocean models, the MITgcm considers the horizontal and vertical directions as separable, and treats them differently. This is useful due to the importance of gravity and stratification in the vertical direction.

In vertical, MITgcm uses z-coordinates. The finite volume approach gives the same discretized equations as a 2nd order cantered finite difference method away from the boundaries, however, also allows partially celled cells close to the boundary, allowing a better representation of topography than for a standard z-coordinate finite difference model. A piecewise constant approximation is applied hear, in addition to the standard full step topography representation (Fig. 4.5).

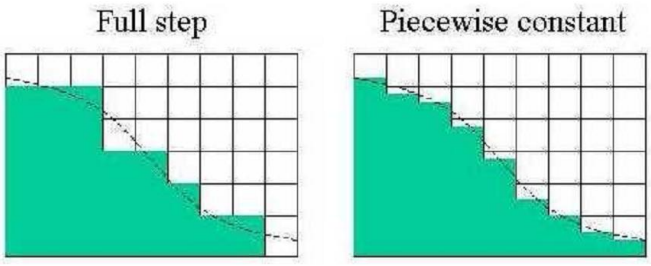

Fig. 4.5 Vertical discretization: Z-coordinates, with finite volume treatment of topography

Fig. 4.6 demonstrates the vertical grid distribution. These vertical layers are not uniformly distributed, can be defined specific layer thickness. The symbol P here represents temperature (T), salinity (S), density (ρ), pressure (P) and horizontal U, V velocity.

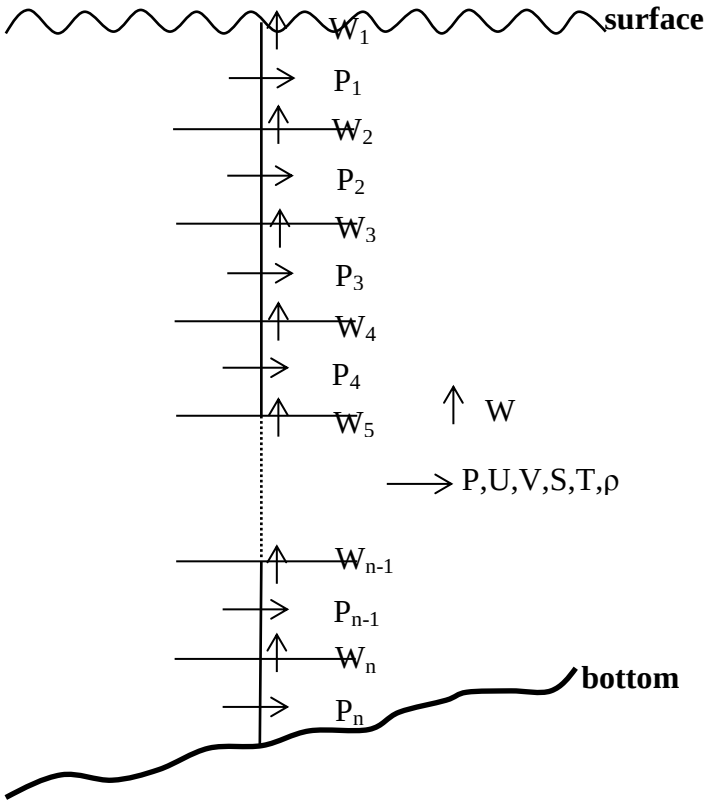

Fig. 4.6 The vertical grid sketch

4.1.5 **Time stepping algorithm**

The equations of motion integrated by the model involve four prognostic equations for flow u and v, temperature θ, and salinity S, and three diagnostic equations for vertical flow w, density ρ and pressure P. In addition, the surface pressure or height

may be described by either a prognostic or diagnostic equation and if non-hydrostatics terms are included then a diagnostic equation for non-hydrostatic pressure is also solved. The combination of prognostic and diagnostic equations requires a model algorithm that can march forward prognostic variables while satisfying constraints imposed by diagnostic equations.

The time stepping algorithm in MITgcm uses a mix between explicit and implicit methods. Some terms are treated explicitly, via a 2nd order Adams-Bashforth scheme, while others are treated implicitly, with a backward method. First, the explicit terms are computed to derive a preliminary value for the next time step, and then the implicit terms are taken into account via a correction step.

Fig. 4.7 illustrates the location of variables in time and the evolution of the algorithm with time. All prognostic variables are co-located in time. Explicit tendencies are evaluated at time level n as a function of the state at that time level (dotted arrow). The explicit tendency from the previous time level, n-1, is used to extrapolate tendencies to n+1/2 (dashed arrow). This extrapolated tendency allows variables to be stably integrated forward-in-time to render an estimate (*-variables) at the n+1 time level (solid arc-arrow). The operator L^{-1} formed from implicit-in-time terms is solved to yield the state variables at time level n+1. In this way, the Adams-Bashforth extrapolation of explicit tendencies fits neatly into the pressure method algorithm when all state variables are co-located in time.

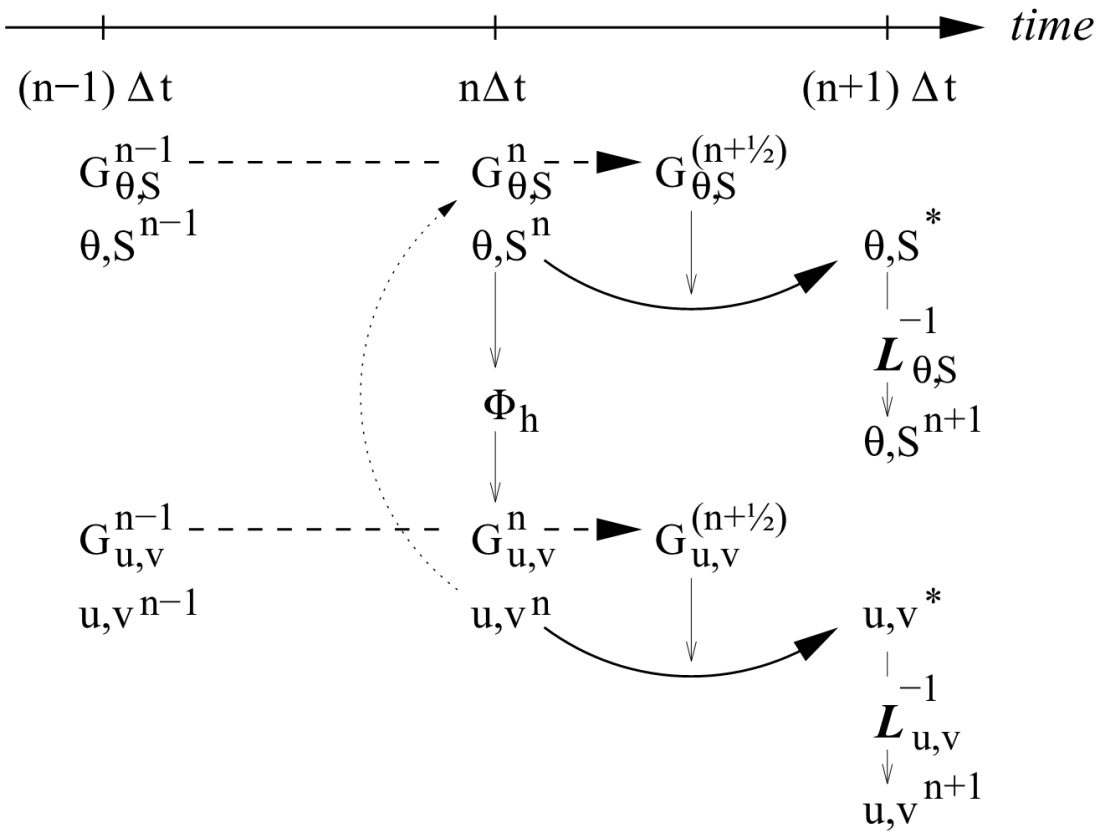

Fig. 4.7 A schematic of the explicit Adams-Bashforth and implicit time-stepping phases of the algorithm.

The algorithm can be represented by the sequential solution of the follow equations:

$$G^{n}_{\theta,S} = G_{\theta,S}(u^{n}, \theta^{n}, S^{n}) \tag{4.14}$$

$$G^{(n+1/2)}_{\theta,S} = (3/2 + \varepsilon_{AB})G^{n}_{\theta,S} - (1/2 + \varepsilon_{A,B})G^{n-1}_{\theta,S} \tag{4.15}$$

$$(\theta^{*}, S^{*}) = (\theta^{n}, S^{n}) + \Delta t G^{(n+1/2)}_{\theta,S} \tag{4.16}$$

$$(\theta^{n+1}, S^{n+1}) = L^{-1}_{\theta,S}(\theta^{*}, S^{*}) \tag{4.17}$$

$$\phi^{n}_{hyd} = \int b(\theta^{n}, S^{n}) dr \tag{4.18}$$

$$\vec{G}^{n}_{\vec{v}} = \vec{G}_{\vec{v}}(\vec{v}^{n}, \phi^{n}_{hyd}) \tag{4.19}$$

$$\vec{G}_{\vec{v}}^{(n+1/2)} = (3/2 + \varepsilon_{AB})\vec{G}_{\vec{v}}^{n} - (1/2 + \varepsilon_{A,B})\vec{G}_{\vec{v}}^{n-1} \tag{4.20}$$

$$\vec{v}^{*} = \vec{v}^{n} + \Delta t \vec{G}_{\vec{v}}^{(n+1/2)} \tag{4.21}$$

$$\vec{v}^{**} = L_{\vec{v}}^{-1}(\vec{v}^{*}) \tag{4.22}$$

$$\eta^{*} = \varepsilon_{fs}(\eta^{n} + \Delta t(P - E)) - \Delta t \nabla \cdot H\vec{v}^{**} \tag{4.23}$$

$$\nabla \cdot gH\nabla \eta^{n+1} - \frac{\varepsilon_{fs}\eta^{n+1}}{\Delta t^{2}} = -\frac{\eta *}{\Delta t^{2}} \tag{4.24}$$

$$\vec{v}^{n+1} = \vec{v}^{*} + \Delta t g \nabla \eta^{n+1} \tag{4.25}$$

1. Calculate the explicitly terms of the tracer $G_{\theta,S}^{n}$ (4.14).

2. Move these terms forward in time $G_{\theta,S}^{(n+1/2)}$, by using the Adams-Bashforth method, where ε_{AB} is a small but finite value, introduced to improve stability of the method(4.15).

3. Find an estimate solution (θ^{*}, S^{*}) (4.16).

4. Find the new tracer fields at n+1 by matrix inversion of the implicit terms (4.17).

5.Similarly procedure is the Adams-Bashforth extrapolation of accelerations, stepping forward and solving of implicit viscosity and surface pressure gradient terms ,corresponding to Equations (4.19)-(4.25). This, then, represents an entire algorithm for stepping forward the model one time-step.

4.1.6 **Advection schemes**

MITgcm allows a number of advection schemes:

Centered second order: Default. Consistent with the continuity equation and conserves energy , but is notoriously noisy , and must therefore be used with some finite amount of diffusion. Easily unstable.

Centered fourth order: More accurate than the second order scheme, and therefore useful in high-resolution simulations.But have the same problem with noise and instability.

Third order upwind bias: Compromise between accuracy and smoothness. Less noisy than with the cantered schemes, but introduces numerical diffusion.

Second order flux limiters: In a flux limiter method, the flux of a conserved quantity into a control volume is limited to a level that will not produce an extrema in that control volume.

Third order direct space time (DST3): Non-linear scheme which deals with space and time discretization together . In the limit when the Courant number vanishes, the DST scheme reduces to a conventional third-order upwind scheme. However, for large Courant numbers, this scheme is more accurate and has more stability (up to Courant number 1).

DST3 with flux limiter: The DST3 method still has some overshoots. This can be controlled with a flux limiter.

4.1.7 **Non-hydrostatic capability**

When the vertical scales are much smaller than the horizontal scales, the vertical momentum equation (the vertical component of equation (4.1)) can be approximated by the hydrostatic balance:

$$\frac{\partial p}{\partial z} = \rho g \tag{4.26}$$

For large-scale ocean flows, the hydrostatic approximation is valid: the non-hydrostatic contribution to the dynamics is very small. The hydrostatic approximation is therefore used in most ocean codes.

However, as the horizontal scales get smaller and become comparable to the vertical scales, the non-hydrostatic terms become increasingly significant, and on a scale somewhere between 10 and 1 km, the hydrostatic approximation breaks down (Marshall *et al.*, 1997b). Fig. 4.8 shows examples of important phenomena on various length scales in the ocean.

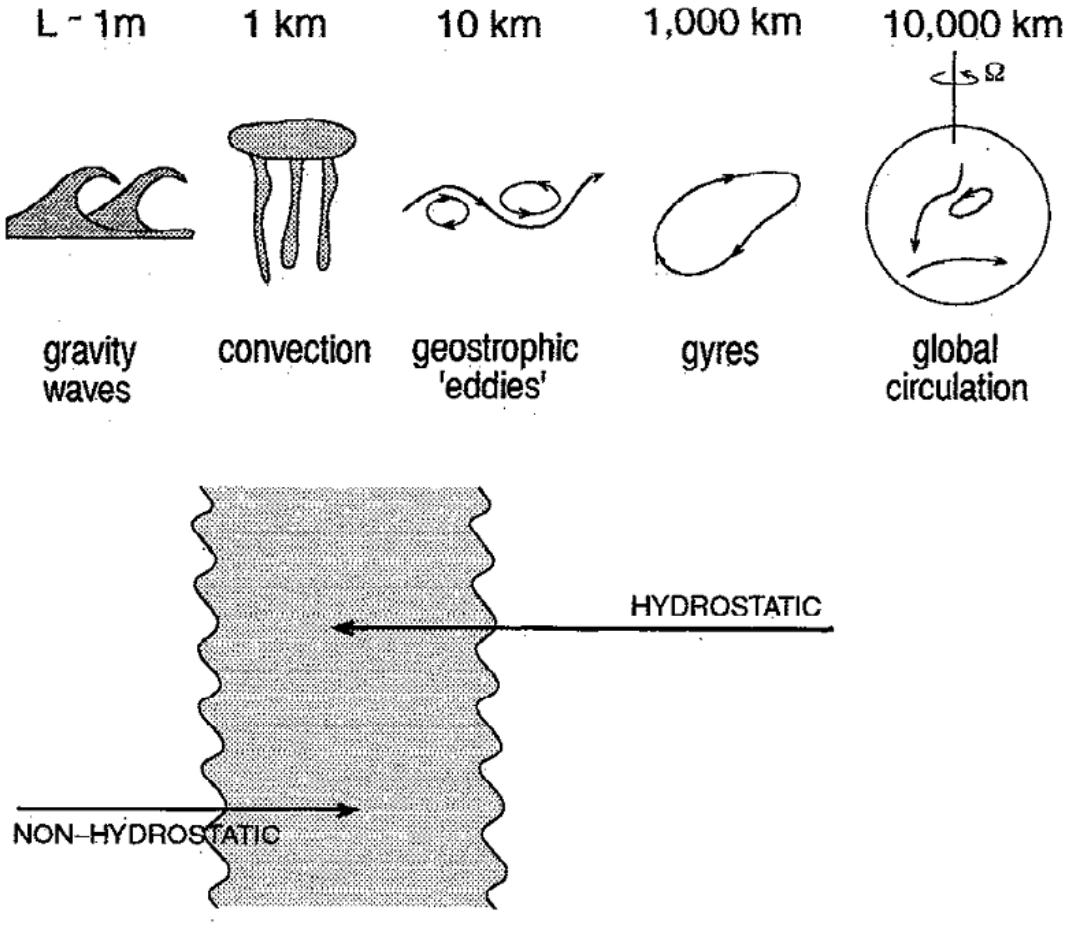

Fig. 4.8 The hydrostatic approximation is valid when the horizontal length scales are much larger than the vertical length scales (Marshall *et al.*, 1997b)

The hydrostatic approximation can be turned on or off, depending on the process studied in MITgcm. This broadens the range of applications of the code, allowing

small-scale studies as well as simulation of larger-scale ocean flows. It also makes it possible to evaluate the validity of the hydrostatic approximation in a specific case, comparing the results from hydrostatic and non-hydrostatic simulations. Also, even if the system is close to hydrostatic balance, the small non-hydrostatic effects can be isolated and studied.

The overall solution strategy used in MITgcm is shown in Fig. 4.9. In hydrostatic mode, the strategy is as follows: First, the surface and hydrostatic pressure is found, solving a 2D elliptic equation. Then, the horizontal momentum equations are stepped forward, and finally, the vertical velocity is found via the continuity equation. In non-hydrostatic mode, an elliptic equation for non-hydrostatic pressure must be solved in addition.

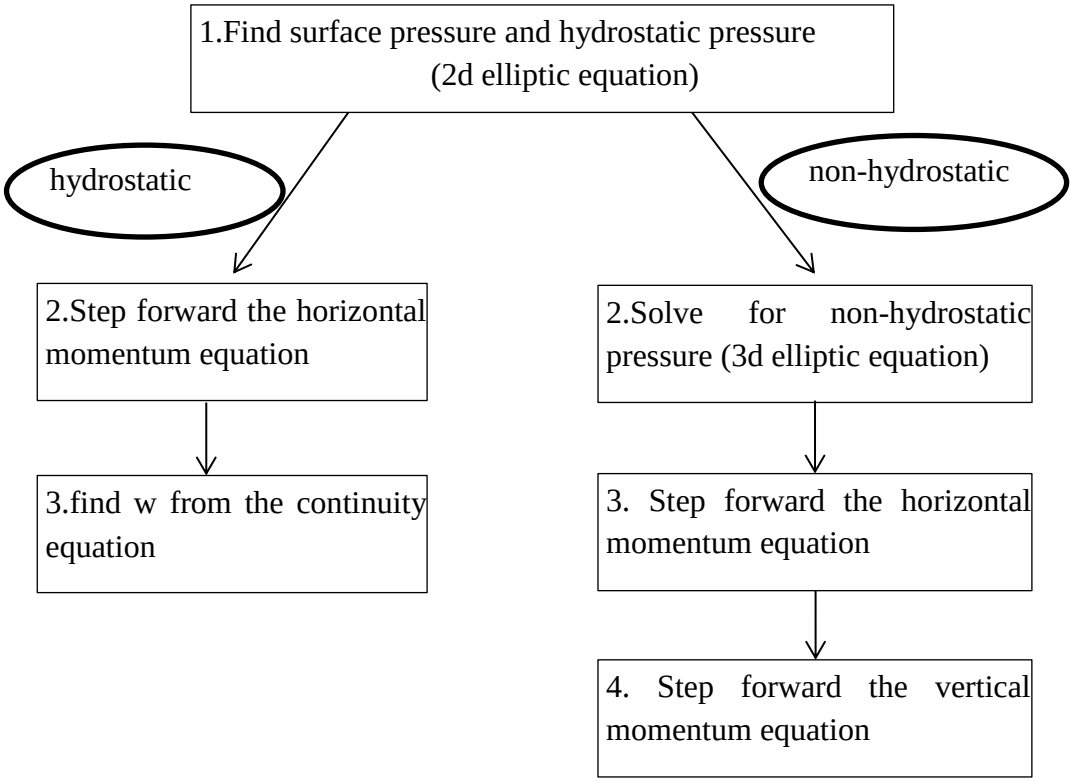

Fig. 4.9 Overall solution strategy in MITgcm

4.2 **Wave module**

The MITgcm has no wave module. Considering the importance of wave on sediment re-suspension, the MITgcm is coupled with a wave module (SWAN) in this study, which is ideal for the regional scale and is often applied to model the wave in the Yellow Sea (Chen *et al.*, 2006; Liang *et al.*, 2007), so that the wave parameters including wave height, period and direction, derived from SWAN, are read into the MITgcm. SWAN can support longitude-latitude regular grid so that the mesh is the same with MITgcm, the coordinate variation is not necessary to consider here.

SWAN is a third-generation wave model for obtaining realistic estimates of wave parameters in coastal areas, lakes and estuaries from given wind, bottom and current conditions. SWAN can be used on any scale relevant for wind-generated surface gravity waves. The model is based on the wave action balance equation with sources and sinks. SWAN can account for diffraction, partial transmission, and reflection, specific formulations for wind input, bottom stress, whitecapping, wave-wave interactions and so on. Table 4.1 lists the physical processes in SWAN.

Table 4.1 Overview of physical processes and generation mode in SWAN

process	authors	Generation		
		1st	2nd	3rd
Linear wind growth	(Cavaleri and Rizzoli, 1981) modified	√	√	
	(Cavaleri and Rizzoli, 1981)			√
Exponential wind growth	(Snyder *et al.*, 1981)(modified)	√	√	
	(Snyder *et al.*, 1981)			√
	(Janssen, 1989; Janssen, 1991)			√
whitecapping	(Holthuijsen and De Boer, 1988)	√	√	
	(Komen and Hasselmann, 1984)			√
	(Janssen, 1991)			√
Quadruplets	(Hasselmann *et al.*, 1985)			√
Triads	(Eldeberky and Battjes, 1996)	√	√	√
Depth-induced breaking	(Battjes and Janssen, 1978)	√	√	√

Bottom friction	(JONSWAP ,1973)	√	√	√
	(Collins, 1972)	√	√	√
	(Madsen *et al.*, 1988)	√	√	√
Obstacle transmission	(Seelig, 1979)	√	√	√
Wave-induced set-up		√	√	√

In SWAN model, the evolution of the wave spectrum is described by the wave action balance equation (Mei, 1983; Komen *et al.*, 1994). The equation expressed by Cartesian coordinates is

$$\frac{\partial N}{\partial t}+\frac{\partial}{\partial x}\left(c_x N\right)+\frac{\partial}{\partial y}\left(c_y N\right)+\frac{\partial}{\partial \sigma}\left(c_\sigma N\right)+\frac{\partial}{\partial \Phi}\left(c_\Phi N\right)=\frac{S_{total}}{\sigma} \qquad (4.27)$$

Where N is wave action density (energy density E_{wave} divided by relative frequency σ), Φ is propagation directions (the direction normal to the wave crest of each spectral component). c_x and c_y are the propagation velocities in the x and y direction. The action density is conserved during propagation in the presence of ambient current, whereas energy density E_{wave} is not (Whitham, 1974).

The left-hand side of Equation (4.27) is the kinematic part of this equation. The second and third terms represent the propagation of wave energy in two-dimensional geographical x and y spaces. The forth term denotes the effect of shifting of the radian frequency due to variations in depth and mean currents. The fifth term represents depth-induced and current-induced refraction. The quantities c_σ and c_Φ are the propagation velocities in spectral space (σ, Φ). The right-hand side is the source/sink term representing all physical processes of wind-wave generation, wave breaking, bottom dissipation, and nonlinear wave-wave interactions.

Based on the results of SWAN model, the wave-induced bottom stress is calculated in different water depth according to a typical mean wave height and period in Yellow

Sea (Fig. 4.10). The wave shear stress is quite large in shallow area but negligible at depth larger than 30m.

The coastal area is important in the sense that the sources of sediment are at the coastal area and the effect of waves become important, it is at the same location where the negative effect of coarse grid is the highest. The grid can be refined further to reduce the negative effect, which requires more computation ability and time. However, as the Yellow Sea has very gentle slope, the shallow coastal can be coverd by 10-20 grid, which is enough to study the regional wave.

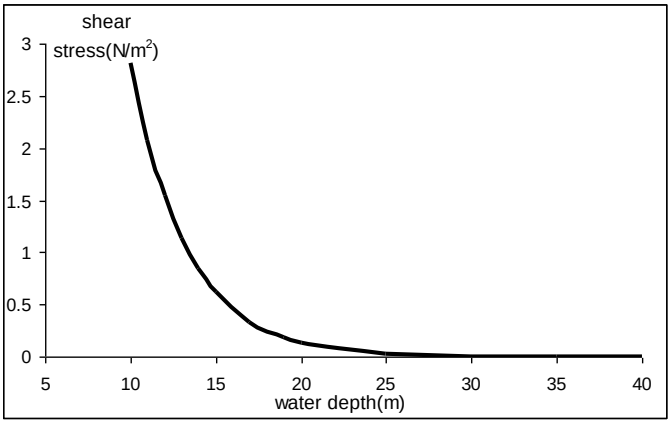

Fig. 4.10 Wave induced shear stress with wave height=2m and wave period=5s

4.3 **Bottom boundary module**

Shear stress, generated by current and waves in the bottom boundary layer, on the seabed is one of the key parameters to the sediment transport. However, the bottom boundary layer is too thin (less than 30 cm) to be resolved in the circulation model, when the treatment of partial cells applied in the MITgcm indicates that the distance between the lowest velocity point and the bottom is on the order of 0.5–1.5 m, which is not fine enough to resolve the boundary layer.

Therefore, a bottom boundary layer (BBL) module is necessary. The bottom boundary layer theory by Grant and Madsen (1979), Kuhrts *et al*.(2004) and Seifert *et al.* (2009) is chosen because it had been applied to study the Yellow Sea sediment

transport by Lu *et al.* (2011). The BBL module is embedded into the MITgcm in this study.

A schematic diagram of bottom boundary layer module (Fig. 4.11) shows how to calculate the current induced bottom shear stress from the lowermost velocity point in the circulation model analytically.

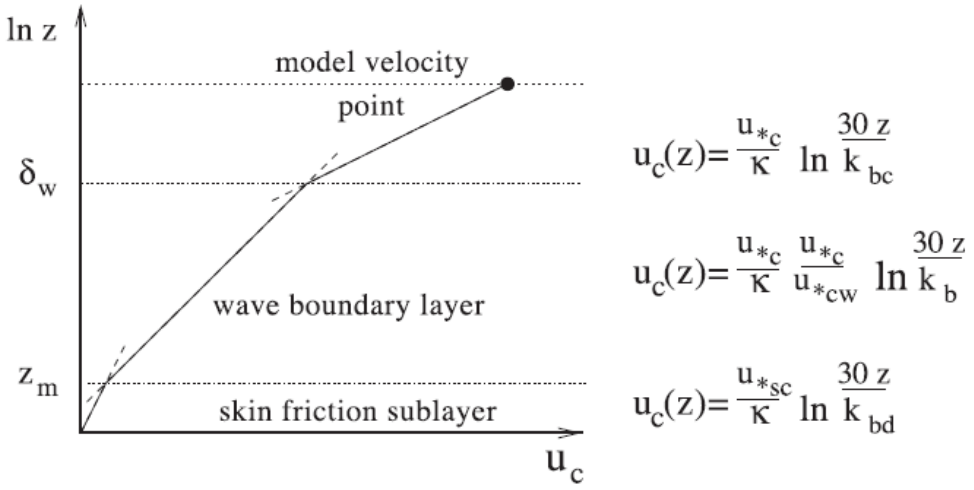

Fig. 4.11 Schematic diagram of the boundary layer model, with piecewise logarithmic velocity profiles.
Where z is the height above the seabed, u_c, current velocity; u_{*c} denotes current bottom shear velocity and u_{*cw} is the total bottom shear velocity caused by currents and waves; u_{*sc}, total skin friction velocity; $\kappa = 0.4$ is the Karman constant; k_b is the geometrical bottom roughness and k_{bc} is the apparent bottom roughness caused by the turbulence in the wave boundary layer while k_{bd} denotes grain roughness.

Considering waves effect of increasing the effective bottom roughness acting on the current and enhance the near-bed turbulence, a wave boundary layer is applied with thickness $\delta_w = 2\kappa u_{*cw}/\omega$, where ω is the angular wave frequency. Assuming a vertically constant shear stress, a piecewise logarithmic velocity profile can be constructed:

$$z < \delta w : u_c(z) = \frac{u_{*c}}{\kappa}\left(\frac{u_{*c}}{u_{*cw}}\right)\ln\frac{30z}{k_b} \tag{4.28}$$

$$z > \delta w : u_c(z) = \frac{u_{*c}}{\kappa} \ln \frac{30z}{k_{bc}} \tag{4.29}$$

$$z < z_m : u_c(z) = \frac{u_{*sc}}{\kappa} \ln \frac{30z}{k_{bd}} \tag{4.30}$$

u_C is the same at the height z= δ_W, implying the relationship

$$k_{bc} = k_b \left(\frac{24 u_{*cw}}{\omega k_b} \right)^{\left(1 - \frac{u_{*c}}{u_{*cw}}\right)} \tag{4.31}$$

The wave shear velocity u_{*W}, assumed not to be affected by the current, is calculated:

$$u_{*w} = \frac{1}{2} f_w U_M{}^2 \tag{4.32}$$

$$f_w = \min \left\{ \exp \left[5.5 \left(\frac{k_b}{A} \right)^{0.2} - 6.3 \right], 0.3 \right\} \tag{4.33}$$

$$U_M = \frac{\pi H}{T} \frac{1}{\sinh(kh)} \tag{4.34}$$

$$A = \frac{H}{2} \frac{1}{\sinh(kh)} \tag{4.35}$$

$$k_b = k_{bd} + k_{br} \tag{4.36}$$

$$k_{bd} = 2.5 d_{50} \tag{4.37}$$

$$k_{br} = 8\varsigma(\varsigma / \lambda) \tag{4.38}$$

$$\lambda \cong 1000\, d_{50} \tag{4.39}$$

$$\varsigma / \lambda \approx 0.1 \tag{4.40}$$

where U_M is the maximal orbital velocity for a wave of height H at the water depth h and A is the amplitude of the wave oscillation excursion on the bottom (k is the wave number). f_w is the wave friction coefficient. k_{br} denotes drag roughness, which can be characterized by ripple spacing λ and ripple height ς.

In order to calculate the current bottom shear velocity u_{*c} from the lowest velocity point of the model grid u_c (z), we start with an initial guess for k_{bc} according to Equation (4.29) and solve then the Equation (4.28) , (4.29)and (4.31) iteratively.

An additional friction sublayer of height $z_m = 0.003 k_{bd} (30\lambda / k_{bd})^{0.8}$ (Smith and McLean, 1977) is introduced to compute the current skin friction velocity. From Equation (4.29) and Equation (4.30) at $z = z_m$, the following expression can be obtained.

$$u_{*sc} = \frac{u_{*c}^{\ 2}}{u_{*cw}} \frac{\ln \frac{30 z_m}{k_b}}{\ln \frac{30 z_m}{k_{bd}}} \tag{4.41}$$

The wave skin friction velocity is calculated similarly as wave friction velocity by:

$$u_{*sw} = \frac{1}{2} f_{sw} U_M^{\ 2} \tag{4.42}$$

$$f_{sw} = \min \left\{ \exp \left[5.5 \left(\frac{k_{bd}}{A} \right)^{0.2} - 6.3 \right], 0.3 \right\} \tag{4.43}$$

Therefore, the total skin friction shear velocity is

$$u_{*s} = \sqrt{u_{*sc}{}^2 + u_{*sw}{}^2} \tag{4.44}$$

4.4 **Sediment module**

Sediment dynamics in the module includes sediment resuspension, transport and deposition of cohesive and noncohesive sediments. Cohesive sediments represent fine-grained sediments with particle diameters less than 75 μm (clay-silt range), while noncohesive sediments with diameters between 75 -500 μm. The main process in sediment module is based on ECOMSED.

As the grain size of the Huanghe River derived sediment is around 19 μm, and the grain sizes of sediment from Old Huanghe River delta and Changjiang River are less than 75 μm, the cohesive sediment is considered here.

4.4.1 **Governing equation**

The three-dimensional advection-dispersion equation for transport of sediment is

$$\frac{\partial \mathrm{C}}{\partial \mathrm{t}} + \frac{\partial UC}{\partial x} + \frac{\partial VC}{\partial y} + \frac{\partial (W - W_s)C}{\partial x} = \frac{\partial}{\partial x}\left(K_H \frac{\partial C}{\partial x}\right) + \frac{\partial}{\partial y}\left(K_H \frac{\partial C}{\partial y}\right) + \frac{\partial}{\partial z}\left(K_v \frac{\partial C}{\partial z}\right) \tag{4.45}$$

Boundary conditions:

$$K_H \frac{\partial C}{\partial z} = 0, z \to \eta \tag{4.46}$$

$$K_H \frac{\partial C}{\partial z} = E - D, Z \to -H \tag{4.47}$$

Where C is suspended sediment concentration; u,v,w is water velocity in the x, y and z direction, W_s is sediment settling velocity; K_H is horizontal diffusivity; K_v is

vertical eddy diffusivity; E_{sed} is resuspension flux, D is deposition flux ; η is water surface elevation and H is bathymetric depth.

4.4.2 **Resuspension of cohesive sediments**

Laboratory experiments (Parchure and Mehta, 1985; Tsai and Lick, 1988; Graham *et al.*, 1992) and field studies (Hawley, 1991; Amos *et al.*, 1992) have revealed that only a finite amount of sediment can be resuspended from a cohesive sediment bed exposed to a constant shear stresses a result of armouring. The amount of fine-grained sediment resuspended from a cohesive sediment bed is given by Gailani *et al.* (1991) as:

$$\varepsilon = \frac{a_0}{T_d^m}\left(\frac{\tau_b - \tau_c}{\tau_c}\right)^n \tag{4.48}$$

where ε is resuspension potential (mg /cm^{-2}); a_0 is constant depending upon the bed properties; T_d= time after deposition (days); τ_b is bed shear stress (dynes/ cm^{-2}); τ_c is critical shear stress for erosion (dynes/cm^{-2}); and m, n is constants dependent on the depositional environment.

The parameters in the above equation are generally determined from shaker studies (Tsai and Lick, 1988).

Experimental results show that the total amount of sediment flux into the water column is not resuspended instantaneously but over a time period of approximately one hour (Tsai and Lick, 1988; MacIntyre *et al.*, 1990). Thus the resuspension rate is given by

$$E_{tot} = \frac{\varepsilon}{3600 \text{ seconds}} \tag{4.49}$$

where E_{tot} is assumed to be constant until all available sediment is eroded. Once the amount ε has been resuspended, E_{tot} is set to zero until additional sediment is

deposited and available for resuspension or until the shear stress increases (Gailani *et al.*, 1991).

The critical shear stress τ_c is a constant without spatial variation in Ecomsed. Some improvement is made by using the following formulation to compute the critical shear stress of the cohesive sediment after Dou (1999):

$$\tau_c = K^2\rho\left(\frac{d'}{d^*}\right)^{\frac{1}{3}}\left[3.6\frac{\rho_s-\rho}{\rho}gd_{50}+\left(\frac{\gamma_0}{\gamma_{0*}}\right)^{\frac{5}{2}}\left(\frac{\varepsilon_0+gh\delta\sqrt{\delta/d_{50}}}{d_{50}}\right)\right] \qquad (4.50)$$

where ρ is water density, ρ_s is sediment density, h is water depth, g is gravitational acceleration, and d_{50} represents median size of sediment. ε_0 is comprehensive cohesion coefficient, ε_0= 1.75 cm^3/s^2 for general sediment. K is a coefficient of different status of incipient motion, is set as 0.128. δ is the thickness of pellicular water, is set as 2.31×10^{-5}cm. d' =0.5 mm when d_{50} is smaller than 0.5 mm, and d_*=10 mm accordingly.

Initial dry bulk density γ_0 is:

$$\gamma_0 = \rho(1-e_0) \qquad (4.51)$$

and steady dry bulk density γ_{0*} is:

$$\gamma_{0*} = \rho_s\left(1-\frac{\pi}{6}\left(1-2\sqrt[3]{d}\right)\right) \qquad (4.52)$$

Where e_0 is the maximum porosity, set as 0.625 for the diameter of 19mm.

4.4.3 **Deposition of cohesive sediments**

The cohesive nature of particles in suspension causes discrete particles to aggregate, forming flocs that vary in size and settling velocities. Variation in concentration and Internal shear stress affects both the size and settling speed of the

floc (Burban *et al.*, 1990).Characterization of depositional fluxes in natural water systems can thus be difficult. In SED, the deposition rate for cohesive sediments depends directly upon the sediment flux approaching the bed and the probability of the flocs sticking to the bed, according to the formulation of Krone(1962)as follows:

$$D = -W_s C P_{dep} \tag{4.53}$$

in which D = depositional flux (g $cm^{-2}s^{-1}$); Ws= settling velocity of the cohesive sediment flocs (cm s^{-1}); C= cohesive suspended sediment concentration (g cm^{-3}) near the sediment-water interface; P_{dep} is probability of deposition.

Settling speeds of cohesive flocs have been measured over a large range of concentrations and shear stresses(Burban *et al.*, 1990). Experimental results show that the settling speed of cohesive flocs is dependent on the product of concentration and the water column shear stress at which the flocs are formed, resulting in the following relationship:

$$W_s = \alpha'(CG)^{\beta'} \tag{4.54}$$

where W_s ,C, G are expressed in m day^{-1}, mg L^{-1}, and dynes cm^{-2},respectively. The above equation implicitly incorporates the effect of internal shear stress (G) on aggregation and settling. For saltwater suspensions, analysis data revealed values of α' and β' of 2.42 and 0.22, respectively(Burban *et al.*, 1990).

The water column shear stress (G) is computed from the hydrodynamic output as flows:

$$G = \rho A_v \left[\left(\frac{\partial u}{\partial z}\right)^2 + \left(\frac{\partial v}{\partial z}\right)^2\right]^{1/2} \tag{4.55}$$

where A_v= vertical eddy viscosity, and ρ= density of the suspending medium.

The probability of deposition (P_{dep}) parameterizes the effects of floc size heterogeneity and near bed turbulence on the deposition rate. The complex interactions occurring at the vicinity of the sediment-water interface cause only a certain fraction of settling sediments to actually become incorporated into the bed (Krone,1962;Parthenia des,1992). Krone(1962)was the first to develop a relationship for the probability of deposition.

$$P_{dep} = \begin{cases} 1 - \frac{\tau_b}{\tau_d}, & \tau_b \leq \tau_d \\ 0, & \tau_b > \tau_d \end{cases} \quad (4.56)$$

Where τ_b= bottom shear stress (dynes cm^{-2}), and τ_d= critical shear stress for deposition (dynescm^{-2}). The critical shear stress for deposition (τ_d) is typically used as a calibration parameter in modeling studies because it is not well known. Limited experimental data indicate τ_d ranges between 0.6 and 1.1 dynes cm^{-2}, depending on sediment concentration and type (Krone, 1962; Mehta and Partheniades, 1975). Wave effects represented in the mud transport on the calculation of the bottom shear stress (τ_b), which derived from the bottom boundary layer module. In this way, wave can affect the sediment resuspension and deposition.

4.5 **Model setup**

4.5.1 **Initial condition**

The model was initialized from a hot start. Geostrophic currents are derived from a project called Estimating the Circulation and Climate of the Ocean, Phase II (ECCO2): High-Resolution Global-Ocean and Sea-Ice Data Synthesis, funded by NASA Modelling, Analysis, and Prediction (MAP) program. While temperature and salinity is interpolated from World Ocean Database 2001(WOD01) with high resolution (1/4

degree) (Boyer *et al.*, 2005). Initial water level is set to zero, because water level can reach stable very quickly given hot start of current velocity.

4.5.2 **Grid**

The model domain covers the area of 27.0625 ℃N–41.125 ℃N and 117.5 ℃E–128.3125 ℃E, with a horizontal resolution of 1/16 degree by 1/16 degree. There are 40 levels in the vertical with 20 levels of grid 5m in the top 100 m, and then 10 levels of 25m, 5 levels of 100m and 5 levels of 180m downwards.

4.5.3 **Boundary conditions**

- Heat flux

The boundary input heat flux comes from NOAA NCEP-NCAR CDAS-1: Climate Data Assimilation System Reanalysis Project, where includes monthly mean climatology from all years. The latent and sensible heat flux, long wave flux, incoming solar radiation are added up, and then interpolated to the 1/16 °*1/16 ° grid. The monthly mean heat flux conditions are linearly interpolated at each model time step.

- Wind stress

The model is forced with surface wind stress from monthly mean QuikSCAT wind with resolution of 0.5 *0.5 degree (Risien and Chelton, 2008). The wind fields were interpolated to impose in each model grid using the spline method. Also, the monthly wind data was linearly interpolated to the model time step.

- Tide boundary

The tidal harmony constitutes of east and south boundary are interpolated from an improved version of the Global Tide Model in 0.125 º x 0.125 º resolution, developed by DTU Space in collaboration with DHI(Cheng and Andersen, 2010).

- Current boundary

The east and south boundary current velocities are interpolated from a high resolution (0.25° ×0.25°) global circulation model called Estimating the Circulation and Climate of the Ocean, Phase II (ECCO2): High-Resolution Global-Ocean and Sea-Ice Data Synthesis, funded by NASA Modeling, Analysis, and Prediction (MAP) program.

- Land boundary

The normal component of current is set to zero at the land boundary and a slip condition is imposed.

- Sediment boundary

An upstream boundary condition is applied here. The boundary SSC is set to zero when water flows into the domain in order to clearly distinguish the unique Huanghe River-derived sediment. While water flows out of the boundary, the SSC of the inner connecting grid is used.

Summary：The MITgcm model has a non-hydrostatic capability which enables it to simulate fluid phenomena over a wide range of scales and has a wide variety of packages available to resolve many different processes including overturning and mixing processes caused by temperature, salt and density stratification, which are very important to the hydrodynamic circulation of Yellow Sea. The code allows domain decomposition via MPI, and can thus be run on multiple processors. The limitation is lack of wave and sediment module, which is overcomed by embedding these modules into it in this study. Another limitation is its regular grid rather than flexible mesh, however, regular mesh is enough for studying this large regional area.

Chapter 5 Results and discussions

5.1 **Tide**

The tide in Yellow Sea is predominantly semidiurnal. The tidal range along the China coast is 1 to 2 m while along the Korean coast is 4 to 8 m (Fig. 5.1). The tidal forcing is significant, though variable in time and space. Tidal current velocities vary from lower than 40 cm/s in the central parts of the north and south Yellow Sea to larger than 100 cm/s in the southwest and northeast Yellow Sea. Peak tidal currents along the shores of western Korea can often reach up 1 to 1.5 m/s with a maximum of 4.4 m/s in the passage off the southwest tip of the peninsula. In the central basin, the speeds are of order 0.5 m/s (Choi *et al.*, 2003). The currents circulate counterclockwise around the amphidromic point indicted by the small circles in Fig. 5.1.

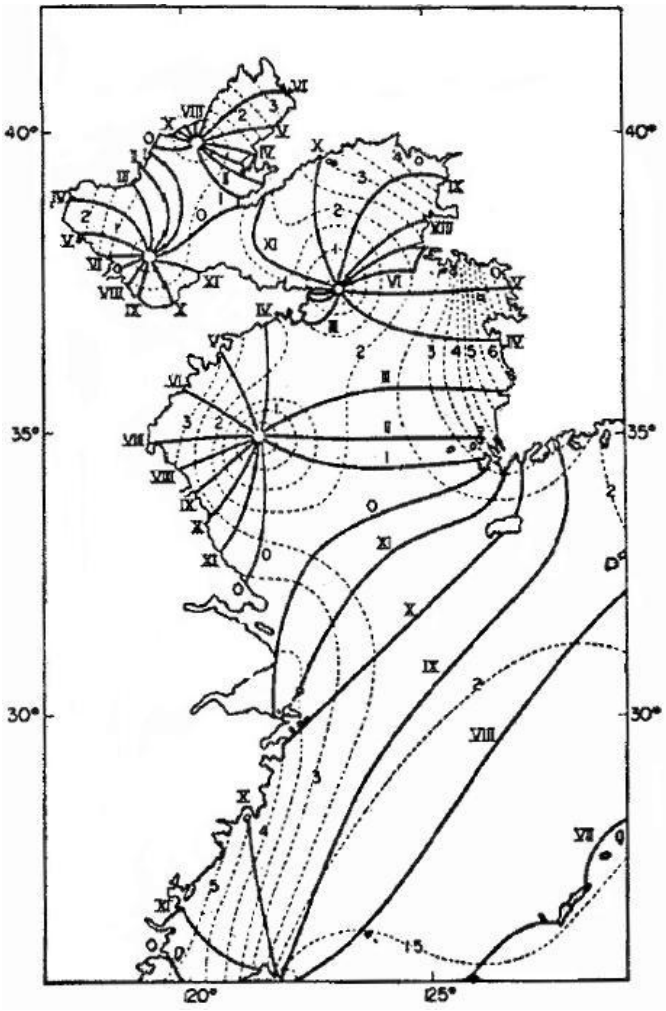

Fig. 5.1 Co-phase lag lines of M2 and range of the semidiurnal tide in the Yellow Sea and East China Sea based on measurement.
Phases refer to the 135 Ɛ longitude and co-range in meters. (Tidal range is twice as amplitude of M2 constitute)(Jackson and Apel, 2004)

Tide is the most studied hydrodynamic process in the Yellow Sea and East China Sea using numerical models of different sophistication (Table 5.1). Here, we applied the MIT model, including a turbulence closure sub-model, to simulate the four major M2, S2, K1 and O1 tides in the EYS, which account for over 95% of tidal energy. The water levels and current velocities over a two-month period were analysed by T_tide at each grid point (Pawlowicz *et al.*, 2002). The tidal model was validated by comparing the model results with observed data and model results from previous researchers.

Table 5.1 Tidal models in the East China Sea and the Yellow Sea

source	Tide	Dimension	ADV	HEV	VEV
(Yanagi and Inoue, 1994)	four	2D	yes	yes	
(Guo and Yanagi, 1998)	four	3D	yes	yes	simple
(Lee and Jung, 1999)	four	3D	yes	yes	close
(Bao *et al.*, 2001)	four	3D	yes	yes	close
(Lee *et al.*, 2002)	M2	3D	yes	yes	simple
(Xia *et al.*, 2006)	M2	3D	yes	yes	close
(Moon *et al.*, 2009)	M2	3D	yes	yes	close

Note: Four means M2, S2, K1, O1tide; ADV: advection term; HEV and VEV, horizontal and vertical eddy viscosities, respectively. The VEV simple means vertical eddy viscosity is calculated by relatively simple flow-related equation while the close means VEV is calculated by solving the close turbulent kinetic energy equation.

5.1.1 **Water elevation**

The model was verified by comparison with observations at the tidal gauges. Harmonic constants of the M2 tide from the model are compared with observed values as shown in Fig. 5.2. The model values are used after interpolation and the observed data are from observation data from tidal stations along the coastline. The differences in the mean values and standard deviations between the simulated and observed M2 tidal amplitude and phase for all sites are 4.6 to 12.5 cm and 6.3 to 10.3 degrees, respectively. The results show that the simulated M2 tide is generally in good agreement with the observation.

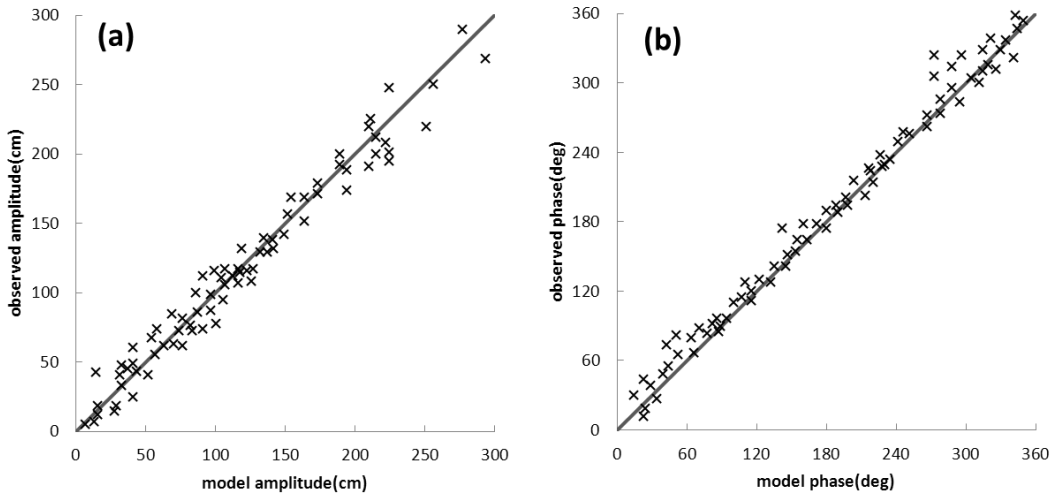

Fig. 5.2 Comparison between the observed M2 amplitude (a) and phase (b) with the model results

Fig. 5.3 shows the calculated co-tidal charts of dominate tidal constitute M2. Compared with the observed chart (Fig. 5.1) and published model results (Fig. 5.4), the general patterns, the number and location of the amphidromic points, and the distribution trend of most co-tidal and co-amplitude lines in the BYECS are generally in good agreement well with observed data (Chen, 1992; Jackson and Apel, 2004) and previous numerical results (Guo and Yanagi, 1998; Bao *et al.*, 2001; Xia *et al.*, 2006), except for a small area near the mouth of Changjiang River and on the coast in the Hangzhou Bay, mainly because the numerical model resolution is not high enough to resolve the complex local topography.

There are four amphidromic points in the Bohai Sea and Yellow Sea. Distribution of co-phase lines indicates that the tidal wave in the East China Sea consists mainly of a northwestward progressive wave. In the Yellow Sea, on the other hand, the peculiar amphidromic system is generated by an overlap of incoming and outgoing Kelvin waves. West-ward shift of the two amphidromes (at the northeast and south of the Shandong Peninsula) from the basin axis can be ascribed either to dissipation of wave

energy, to generation of propagating Poincare waves or to asymmetric depth profile in zonal direction.

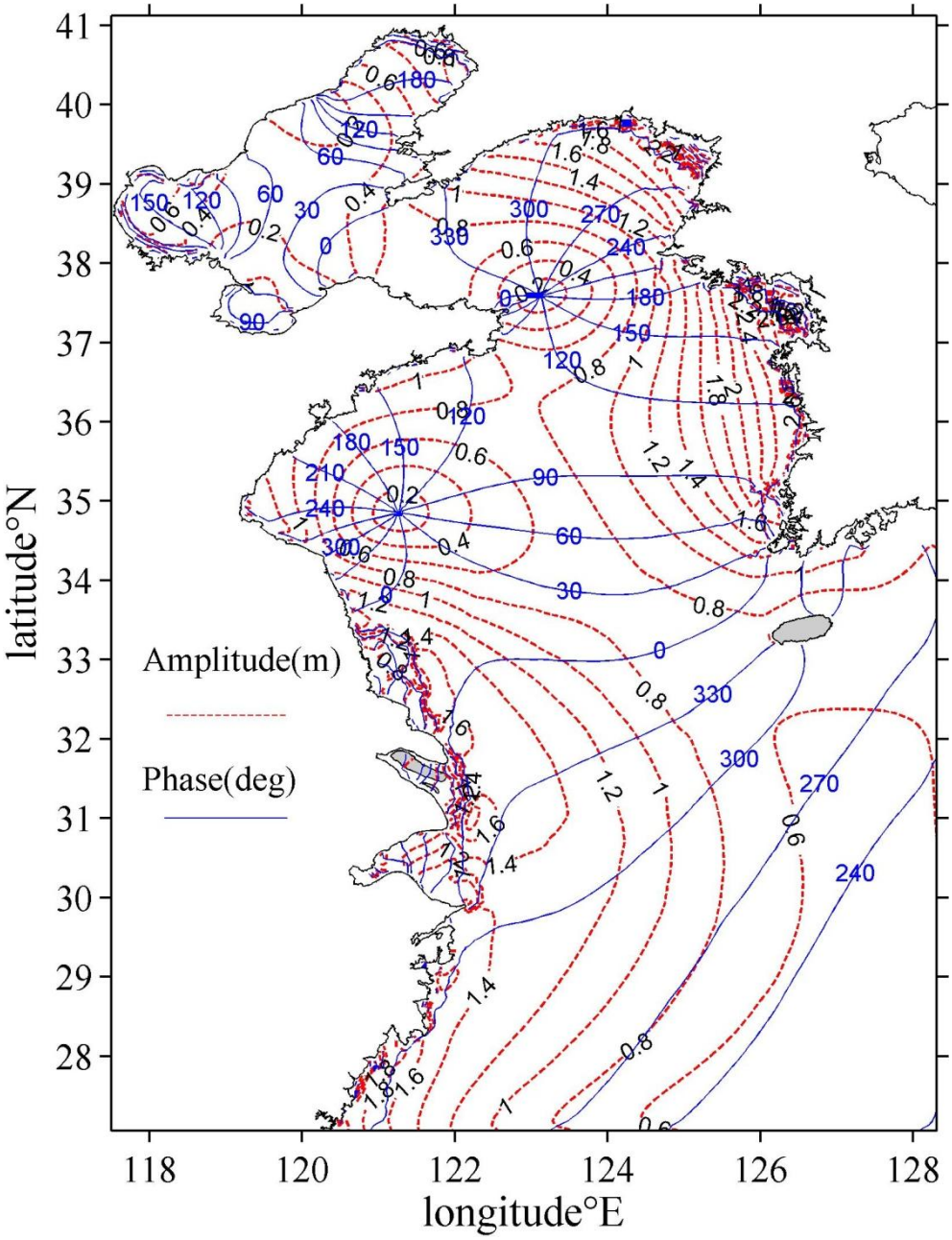

Fig. 5.3 Distribution of co-amplitude (m) and co-phase lag (degree) lines of M2 constitute (phase referred longitude 135 ℃)

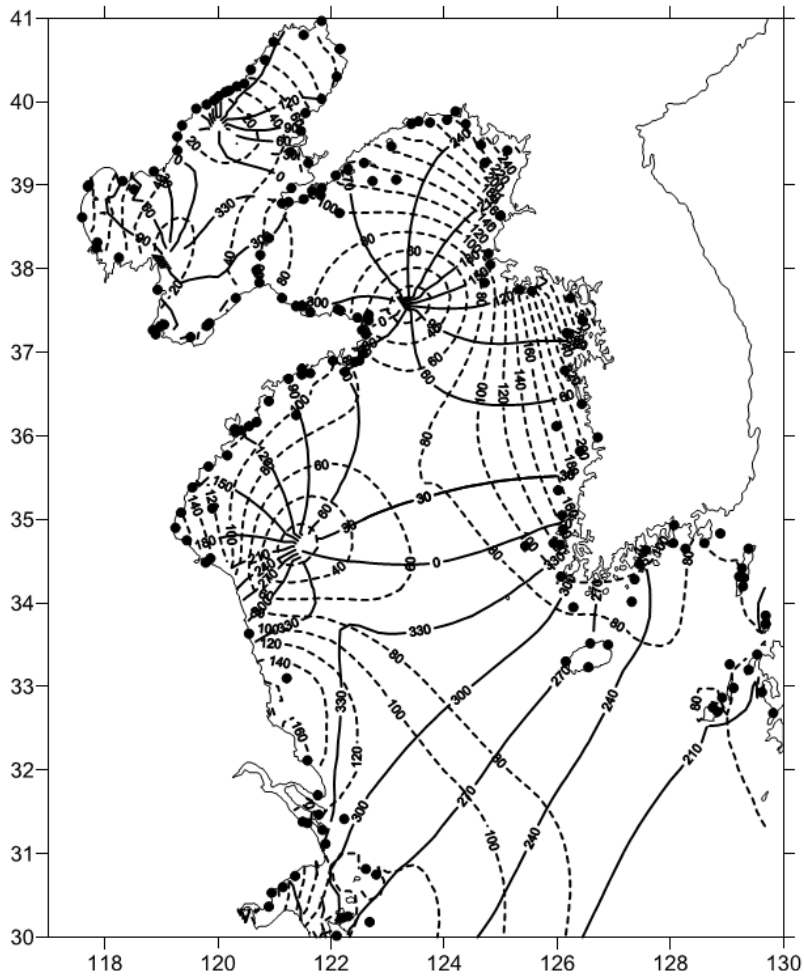

Fig. 5.4 M2 co-tidal chart of model results (Xia *et al.*, 2006)
Solid and dashed lines show the distributions of phase lag (in degree and referred to the 120 ℉ longitude) and amplitude (in cm).

Also as a semi-diurnal constitute, the patterns of S2 is similar with M2, only with smaller amplitude (Fig. 5.5). Maximum amplitudes of M2 and S2 elevations are in the South Korea peninsula coast.

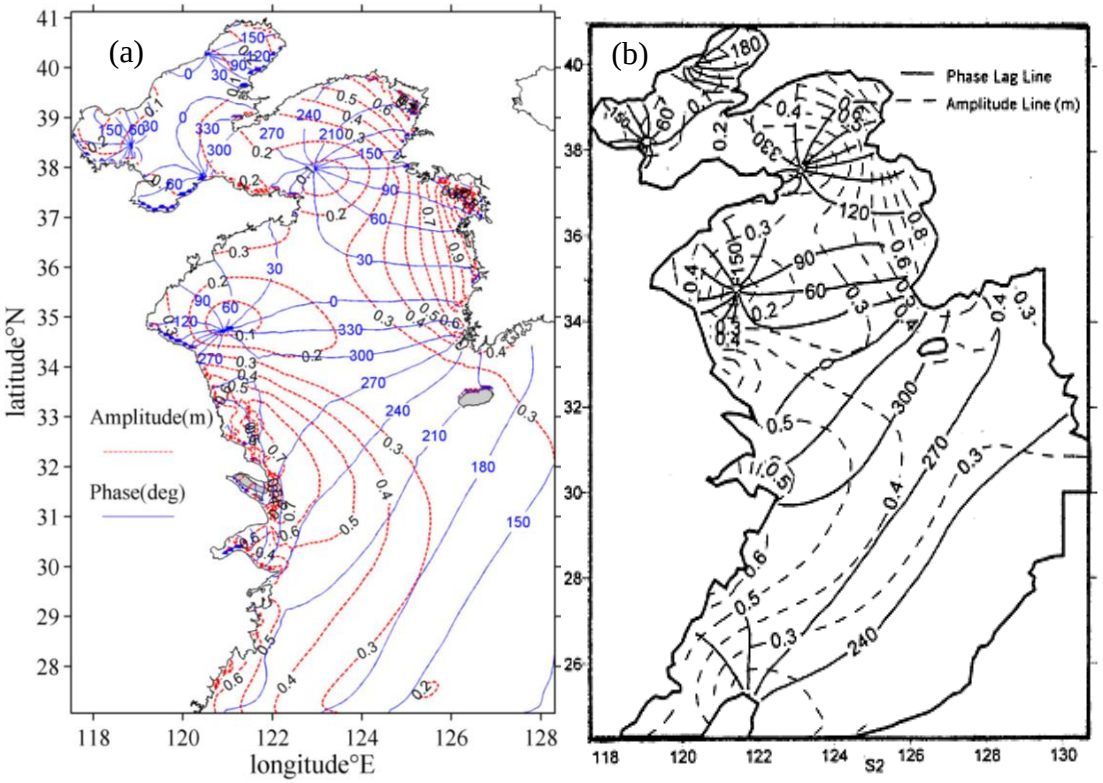

Fig. 5.5 Distribution of co-amplitude (m) and co-phase lag (degree) lines of S2 constitute

(a) model result(phase referred longitude 135 ℃E)

(b) numerical result from (Bao *et al.*, 2001)

Two amphidromic points of diurnal constitutes (K1, O1) exist in the BYES (Fig. 5.6&Fig. 5.7). Distance between the amphidromic points is longer than that in the M2 and S2 case because of the longer wavelength. The amphidromic cells are more symmetric to the basin axis compared to the semi-diurnal case because propagating mode of Poincare waves cannot exist in the diurnal period. K1 amplitude ranges ranged mostly within 0.2- 0.3 m. Again, O1 has similar co-tidal pattern with K1 only with slightly smaller amplitude (Fig. 5.7).

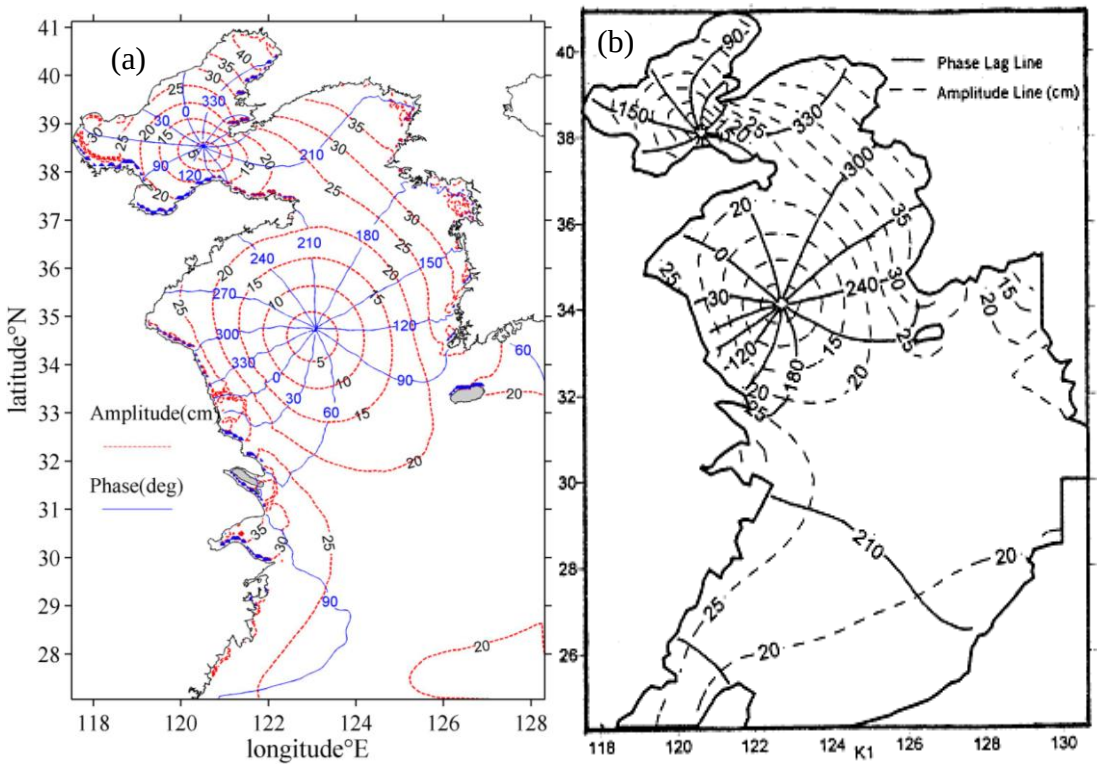

Fig. 5.6 Distribution of co-amplitude (cm) and co-phase lag (degree) lines of K1

(a) model result (phase referred longitude 135 ℃)

(b) numerical result from (Bao *et al.*, 2001)

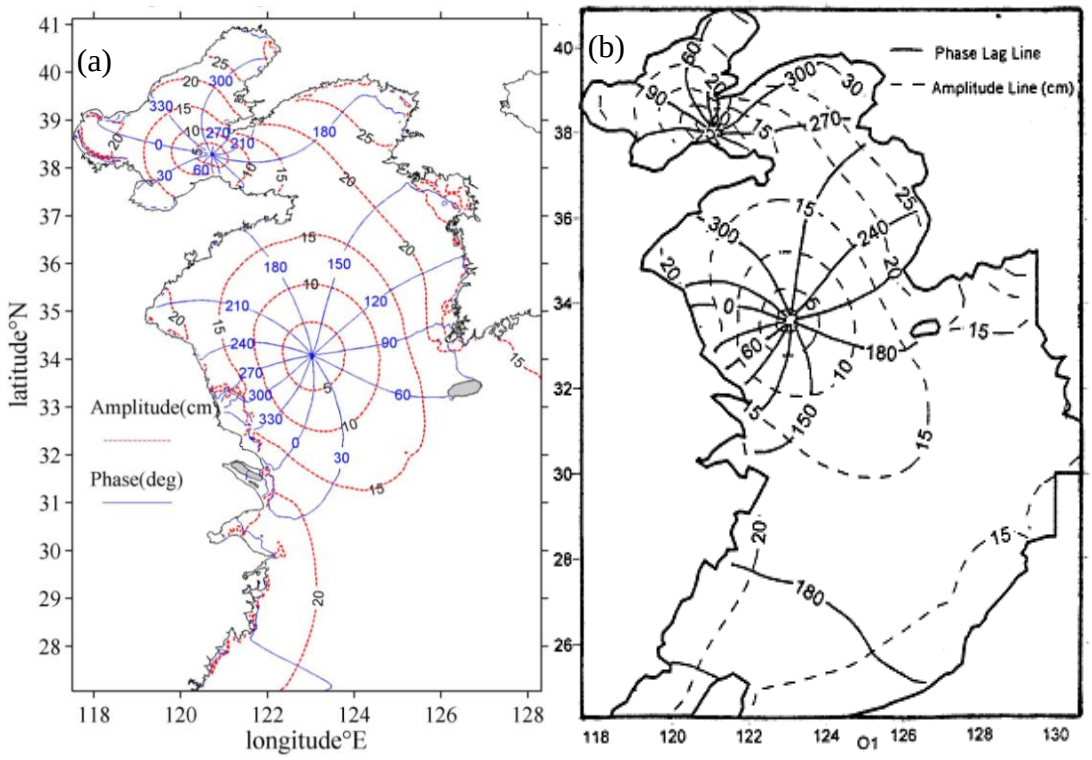

Fig. 5.7 Distribution of co-amplitude (cm) and co-phase lag (degree) lines of O1

(a) model result(phase referred longitude 135 ℃)

(b) numerical result from (Bao *et al.*, 2001)

5.1.2 **Tidal current**

The M2 current ellipse derived from tidal current analysis is shown in Fig. 5.8, which is in good accordance with field data and previous model results (Fig. 5.9&Fig. 5.10). Based on the tidal current analysis, M2 has the highest contribution to the current, about 65%, while the S2, K1, O1 are 18% 10% and 7% respectively.

The velocity of semi-diurnal currents is high (order of 100 cm/s) on the western coast of Korea and at the entrance to the Changjiang River and Hangzhou Bay. Large scale clockwise rotary tidal current with nearly circular ellipses developed in the area off the Changjiang River mouth, as tidal waves from the north-west Pacific Ocean enter the Yellow Sea and the Bohai Sea. The directions of the major axes of tidal

current ellipses are mainly NW-SE in the offshore area south of the Changjiang River mouth.

Tidal currents are weak in the central area of the southern Yellow Sea and change into anti-clockwise northwards. The major axes of tidal current ellipses with greater values of ellipticity in the Haizhou Bay are basically parallel to the trend of coastline, while the major axes of tidal current ellipses offshore the Korea Peninsula are approximately perpendicular to the bay heads.

The values of tidal ellipticity in the Jianghua Bay are higher, and the major axes of tidal current ellipses are near NE-SW, while rectilinear currents appear in the west Korea Bay, and the major axes are NNE-SSW. Weak tidal currents dominate in the western area of the northern Yellow Sea.

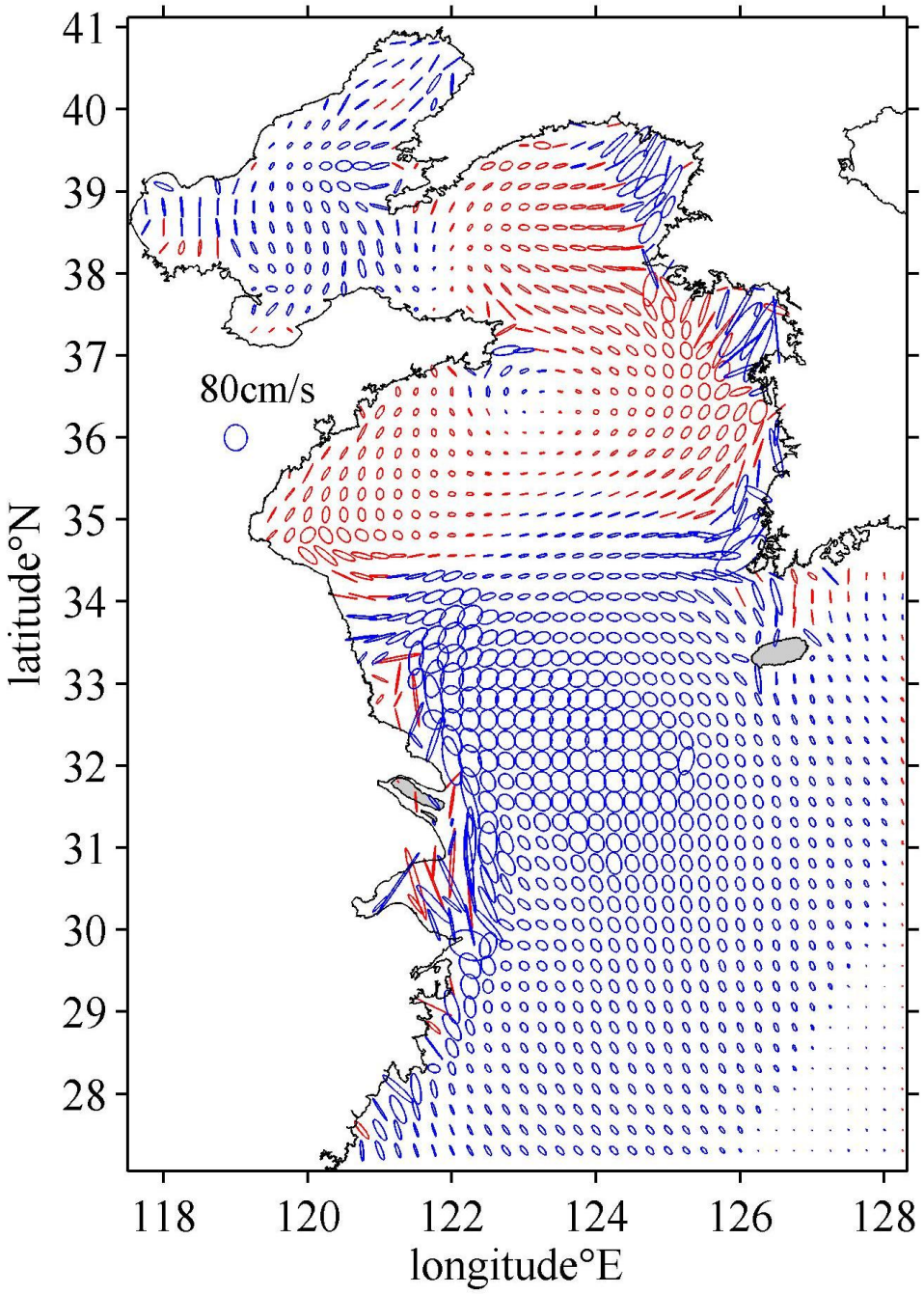

Fig. 5.8 Tidal current ellipse of M2 constitute (Blue- clockwise; Red-anticlockwise)

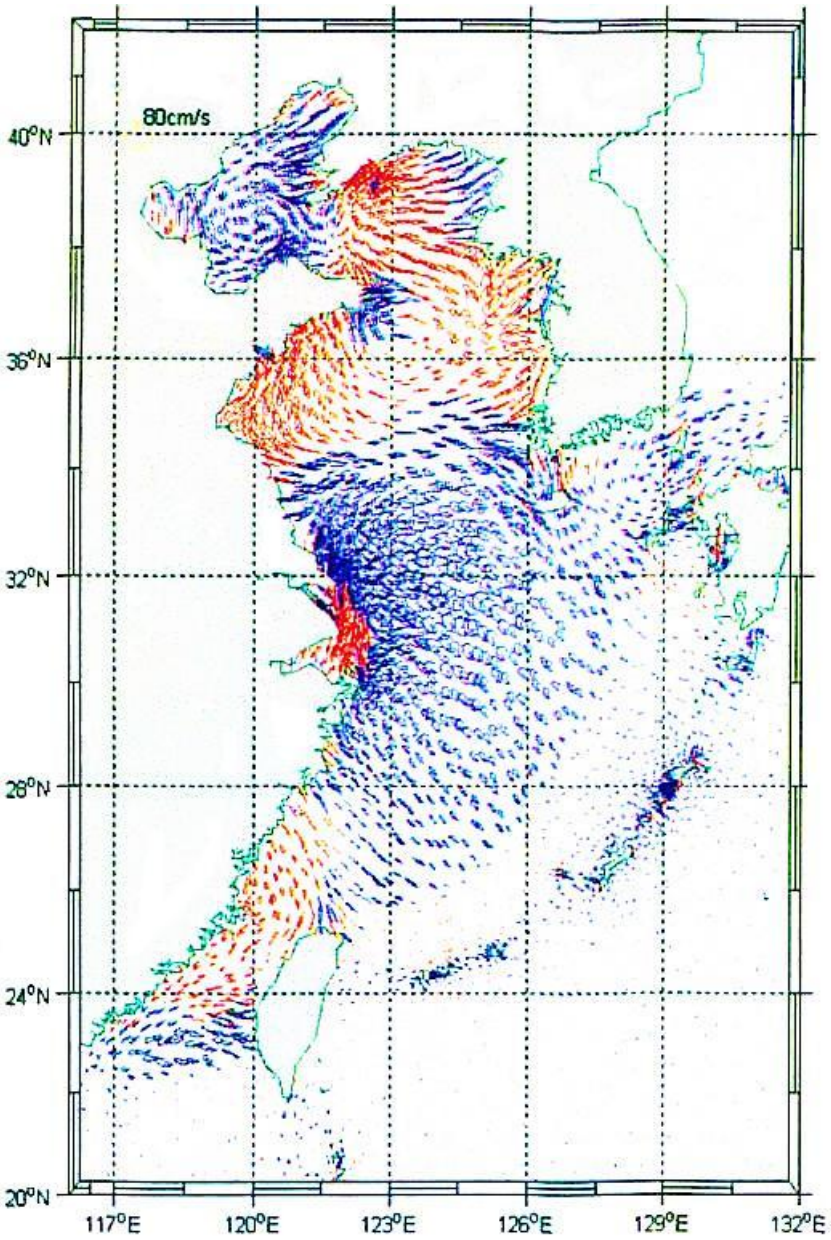

Fig. 5.9 Tidal current ellipse of M2 in the Yellow Sea and East China Sea, model result from Yu (2010) (Blue- clockwise; Red-anticlockwise)

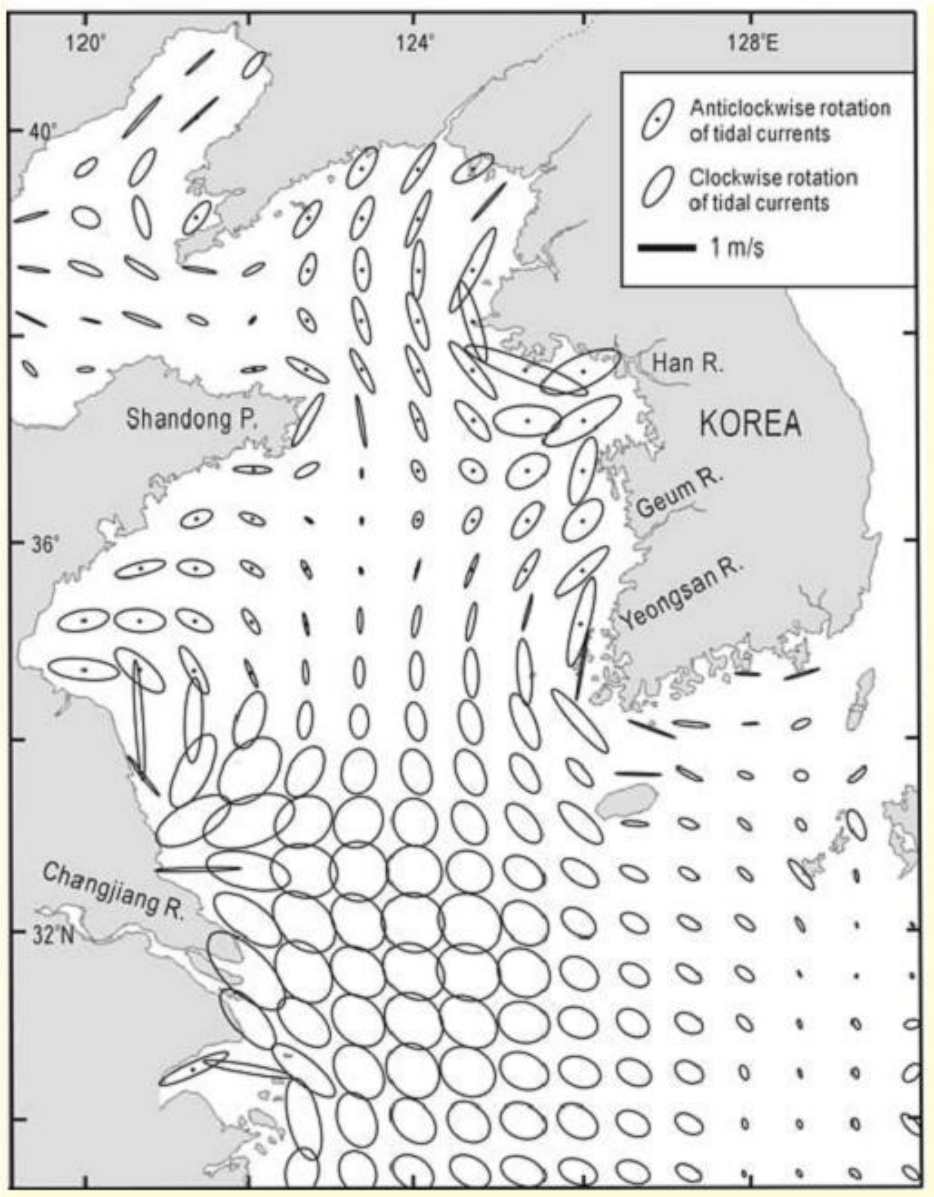

Fig. 5.10 M2 tidal model of the Yellow Sea (Chough *et al.*, 2004).

Some important phenomena such as the Yellow Sea Cold Water Mass and sediment distribution are related to the distribution of tidal currents. The YSCWM front, where the thermocline intersected with the sea bottom, is tidal induced front (Xu *et al.*, 2003; Huang *et al.*, 2010). It is found that distribution of mud deposits on the whole east margin sea of China (except for the Bohai Sea) is always along around 50 m bathymetry (Fig. 1.1). This may be because that the current in the northern hemisphere is always flow along the 50 m bathymetry so as to maintain the angular momentum balance (Lin and Yang, 2011; Lin *et al.*, 2011). Thus the 50 m bathymetry

in fact becomes an interface zone between tidal current and along shore current, and the sediments brought from terrestrial sources could be trapped in the bottom of this interface front area and a high SSC layer is formed. The Central Southern Yellow Sea Mud has a wide sedimentary area, and it became thinner up-dip and wedge out from left edge to right edge with the thickest areas at along 50 m bathymetry.

Fig. 5.11 shows the tidal induced residual current field. The residual current vectors indicated that the tidal current can transport the Huanghe River derived sediment into the Southern Yellow Sea area, and the residual current speed is very small (<2cm/s) at the Central Yellow Sea Mud area which is favourable for the finest mud to deposit.

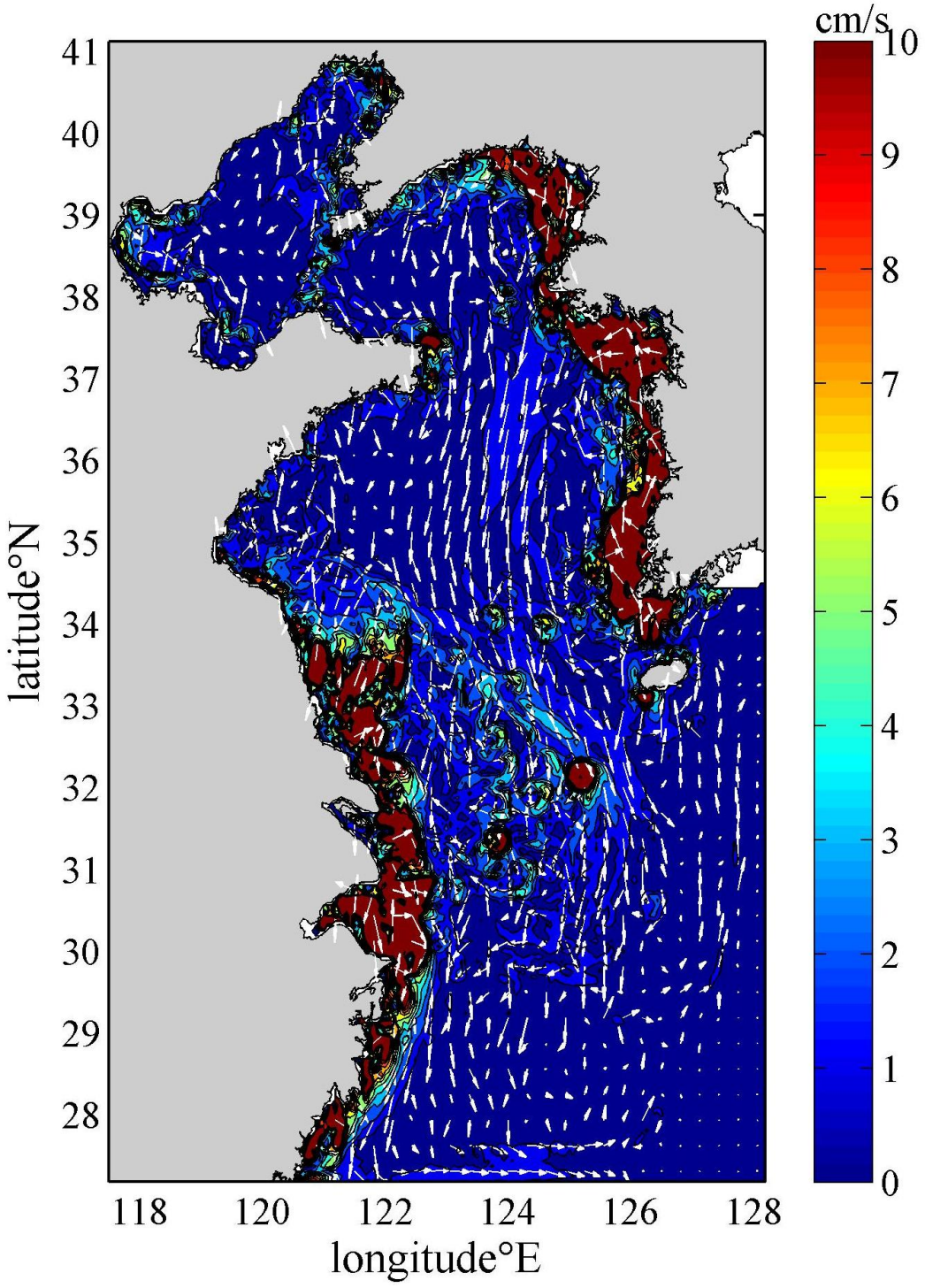

Fig. 5.11 Tidal induced residual current. Velocity (cm/s) is shown in contour.

Fig. 5.12 shows the maximum tidal induced bottom shear stress, which is the maximum value over one month. It can been seen that the bottom shear stress is higher at the coastal area (0.15-0.3 Pa) while smaller in the CYSM area (less than 0.05Pa).

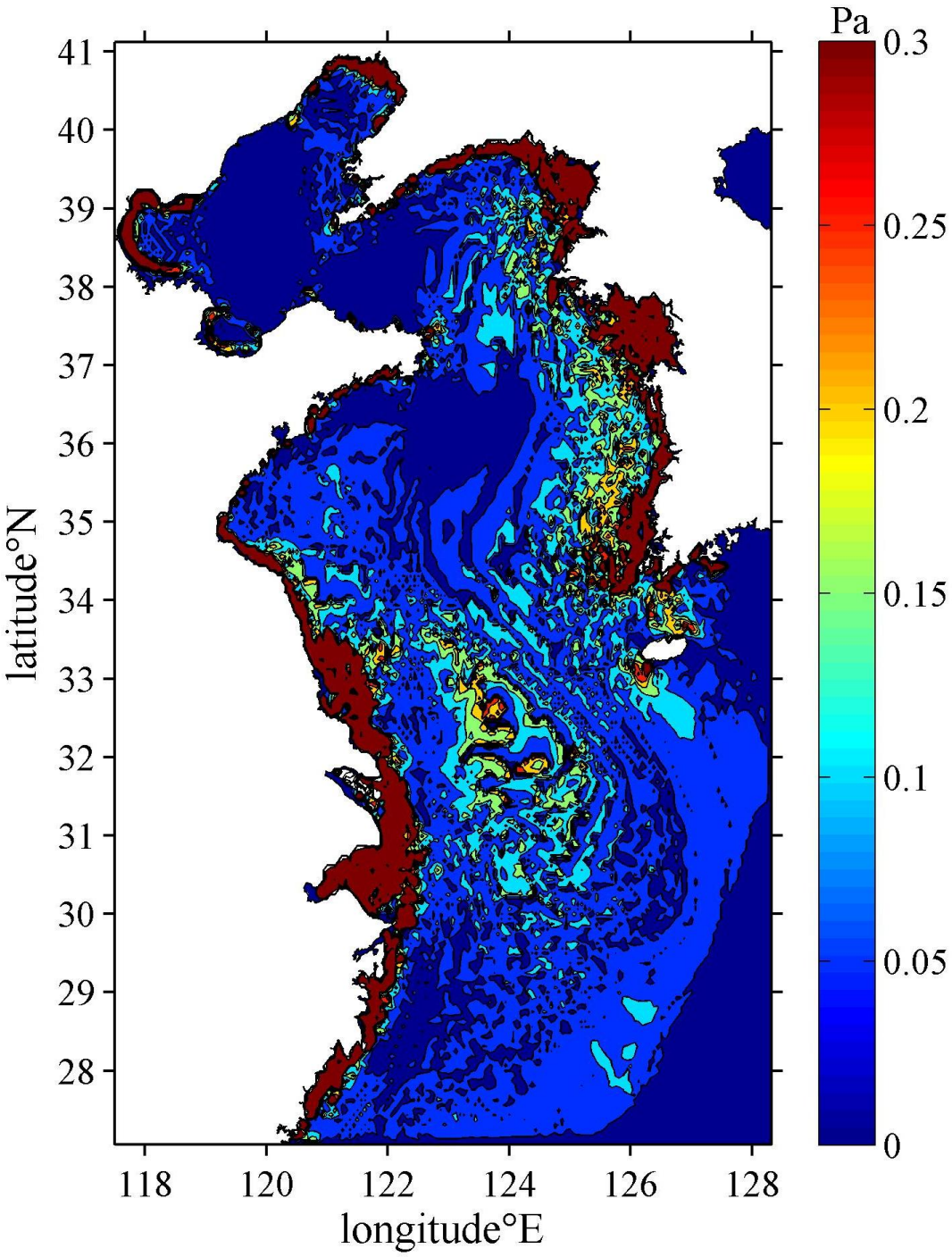

Fig. 5.12 Maximum tidal induced bottom shear stress (Pa)

5.1.3 **Tide evolution under different sea lever over the last 12,000 years**

The geometry of the Yellow and East China Sea (YECS) has experienced significant changes since the last glacial maximum. Geological records indicated the occurrence of rapid sea-level rose more than 100 m during the last 20000 years (Fig. 3.1). Most of the YECS region consists of a continental shelf shallower than 150 m, especially yellow sea shelf shallower than 80m. As basin geometries play an important role in tide propagation, tidal fields in this region must have changed significantly by this rapid sea-level rise. It is therefore necessary to evaluate the paleotidal properties when recovering the paleo-environments in the YECS area and inspecting the SYS mud deposit genesis.

The paleo-tides were induced by specifying amplitude and phase of M2, S2, K1 and O1 along the open boundaries. Output of a present global model was adopted as the boundary values, same with that applied in the present sea level tidal model，becausethere is no data of tidal forcing on the boundary in the past. The first three experiments were carried out by lowering the sea-level from the present state to -60,-30,-15 m respectively, using a present bathymetry (no data available of bathymetry over the geological period), whereas the last one by increasing the sea-level by 5m. All runs initiated from rest state and integrated for 2 months, among which the last 30 days were used for tidal harmonic analyses. The -60, -30, -15, 5m represent the sea-level at 11600,9400,9000 and 7000 aBP according the sea-level curve of Liu et al.(2004c) (Fig. 3.1). When the sea level was lowered by 60 m, the Yellow Sea became a channel of about 200 km wide, bordered by a large landmass extended from the Chinese coast. Amplitude of M2 (Fig. 5.13 (a)) was smaller than that at present in the Yellow Sea (Fig. 5.3). The two degenerated amphidromes in the Yellow Sea, each of which corresponds to the amphidrome of the present located at the north-east and

south of the Shandong Peninsula, shifted to the northeast or east (Table 5.2), and most of the co-phase lines aligned in direction normal to the axis of the bay, indicating smaller influence of the Coriolis force. Large M2 tidal amplitude (>1.4 m) appeared along the southern coast of Korea, just outside the mouth of the paleo-Yellow Sea. M2 tide was also strong at around the paleo-Changjiang estuary (29 ºN, 124.5 ºE) with amplitude of 1.6m. As the sea water level increased to -30m (Fig. 5.13 (b)), almost the entire Bohai Sea region was above the sea level, the two degenerated amphidromes in the Yellow Sea shifted to the northwest or west (Table 5.2) compared with that of -60m case. The M2 tidal amplitude decreased around the southern coast of Korea while increased significantly in the paleo-Changjiang estuary. With sea level rises to -15 m below current sea level (Fig. 5.14 (a)), the other two amphidromes appeared in the Bohai Sea. The amplitudes in the Yellow Sea and Bohai Sea enlarged, mostly because the basin geometry benefits the M2 propagation into the Yellow Sea and Bohai Sea. In the case of sea water level at 5m higher than present, there are still four amphidromes in Bohai and Yellow Sea. The amplitude obviously decreased in the northern Yellow Sea and Bohai region, which is shallow area with water depth mostly 20-50m at present. The 5 meters increase in depth can have significant influence on the tide pattern. Mainly beacause the new basin area enlarged in the 5m case, especially the vast area around the Subei and Changjiang estuary, also very near the amphidromes in the south Yellow Sea, which dissipated large amount of tide energy. The new coastline and bathymetry changed the propagation pattern of M2 (Fig. 5.22) and with the same boundary tide input as present, the tide energy propagated to the north Yellow Sea and Bohai Sea decreased significantly. Furthermore, the M2 co-phase line rotated anti-clockwise as the sea water level increased.

S2 shared the similar evolution pattern with M2 as sea level rose from -60 to 5m (Fig. 5.15&Fig. 5.16 &Table 5.3).

Table 5.2 M2 amphidromic points position under different sea water levels (SWL)

SWL(m)	-60	-30	-15	0	5
Bohai Sea North	—	—	119.196 °E	118.911 °E	118.601 °E
	—	—	38.1154 °N	38.0824 °N	37.7532 °N
Bohai Sea South	—	—	120.28 °E	120.126 °E	120.434 °E
	—	—	39.9235 °N	40.0728 °N	40.2167 °N
North Yellow Sea	122.876 °E	121.312 °E	121.224 °E	121.239 °E	120.657 °E
	35.9075 °N	34.7676 °N	35.0551 °N	34.829 °N	34.4558 °N
South Yellow Sea	123.358 °E	122.246 °E	122.916 °E	123.095 °E	123.217 °E
	37.5225 °N	37.9027 °N	37.5874 °N	37.5819 °N	37.8416 °N

Table 5.3 S2 amphidromic points position under different sea water levels

SWL(m)	-60	-30	-15	0	5
Bohai Sea North	—	—	119.21 °E	118.857 °E	118.608 °E
	—	—	38.1188 °N	38.416 °N	37.75 °N
bohai Sea South	—	—	120.273 °E	120.58 °E	120.528 °E
	—	—	39.9282 °N	40.2721 °N	40.2869 °N
North Yellow Sea	122.745 °E	121.347 °E	121.168 °E	120.925 °E	120.549 °E
	36.0107 °N	34.9706 °N	35.1368 °N	34.7329 °N	34.4495 °N
South Yellow Sea	123.347 °E	122.232 °E	122.895 °E	122.968 °E	123.077 °E
	37.5308 °N	37.8392 °N	37.6586 °N	37.9574 °N	37.9519 °N

In the case of sea level -60 m, amplitude of K1 (Fig. 5.17(a)) was smaller than that at present in the Yellow Sea (Fig. 5.6). Only one amphidrome exists off the southeast of Shandong peninsula in the Yellow Sea. K1 amplitude maximum value is 15-20 cm in the paleo-Yellow Sea. K1 tide retains its amplitude along the axis of the bay, as can be recognized from the 0.1 m contour, which is quite different with M2 tide amplitude decreasing rapidly as it enters the Yellow Sea (from about 1.2 m to less than 0.4 m). As the sea level rose to -30m (Fig. 5.17(b)), the amphidromic point shifted northward in the Yellow Sea (Table 5.4) compared with that of -60m case. The large K1

amplitude value (50cm) appeared in the Bohai Sea strait (122.5 ℃, 38.4 ℃), much larger than present value (20cm). With sea level increasing to -15 m (Fig. 5.18(a)), two amphidromes appeared, one in the Bohai Sea and the other in the Yellow Sea, shifting westward compared with present points (Table 5.4), the amplitudes decreased in general compared with modern state. In the case of sea water level 5m higher than present, there are still two K1 amphidromes totally in Bohai and Yellow Sea. The K1 amplitude, however, increased in the northern Yellow Sea and Bohai region while decreased slightly in the southern Yellow Sea. Because the K1 amphidromic point in the South Yellow Sea are relatively far away from the Subei and Changjiang estuary area. The new coastline and bathymetry benefit the K1 propagating into the north Yellow Sea and Bohai Sea.

Moreover, the K1 co-phase line also rotated anti-clockwise as the sea water level increased. O1 have the similar change pattern with K1 as sea level rose from -60 to 5m (Fig. 5.19&Fig. 5.20 &Table 5.5).

Table 5.4 K1 amphidromic points position under different sea water levels

SWL(m)	-60	-30	-15	0	5
Bohai Sea	—	—	119.877 ℃ 38.1245 ℃	120.526 ℃ 38.5191 ℃	120.146 ℃ 38.1797 ℃
Yellow Sea	123.227 ℃ 36.4229 ℃	123.499 ℃ 36.8932 ℃	122.001 ℃ 35.0079 ℃	123.113 ℃ 34.7315 ℃	122.543 ℃ 34.5304 ℃

Table 5.5 O1 amphidromic points position under different sea water levels

SWL(m)	-60	-30	-15	0	5
Bohai Sea	—	—	120.052 ℃ 38.1999 ℃	120.724 ℃ 38.2769 ℃	120.347 ℃ 38.1643 ℃
Yellow Sea	123.13 ℃ 36.2165 ℃	123.467 ℃ 36.5528 ℃	122.6 ℃ 34.7447 ℃	123.04 ℃ 34.0777 ℃	122.714 ℃ 34.1629 ℃

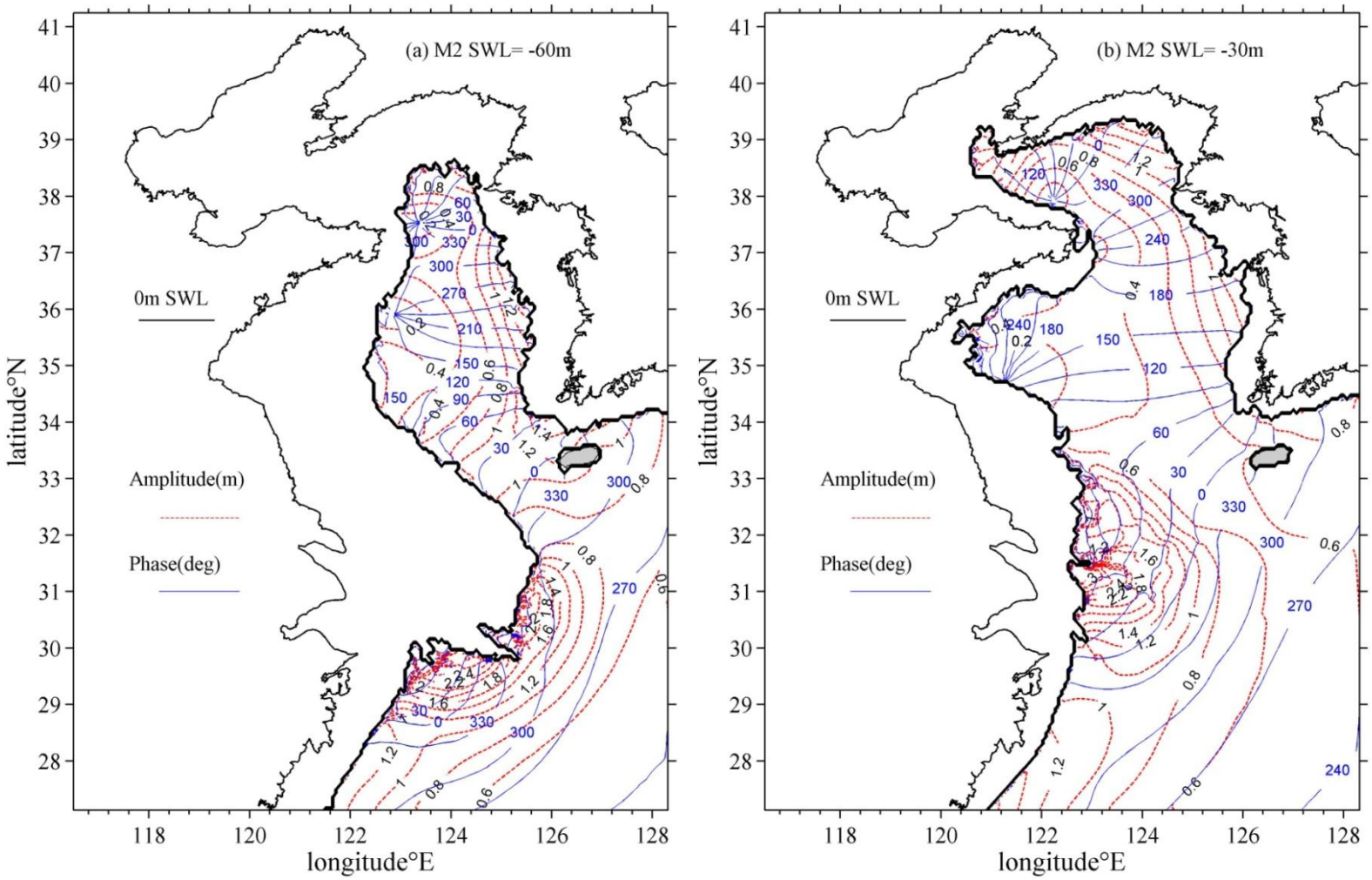

Fig. 5.13 Co-tidal chart of the calculated M2 constitute for sea water level (a)-60m (b) -30m, blue lines show co-phase lines with 30 °interval

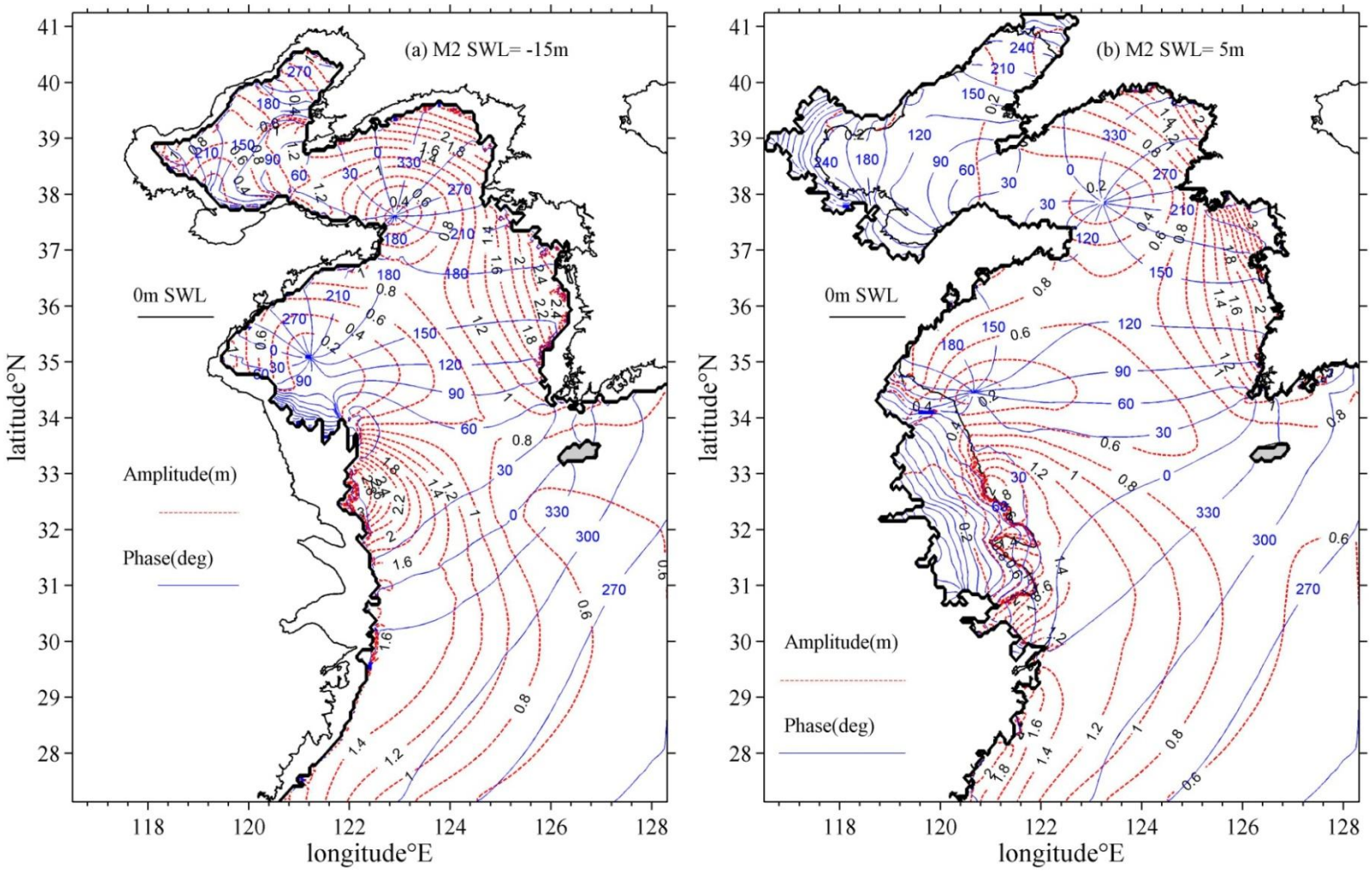

Fig. 5.14 Co-tidal chart of the calculated M2 constitute for sea water level (a)-15m (b) 5m, blue lines show co-phase lines with 30 °interval

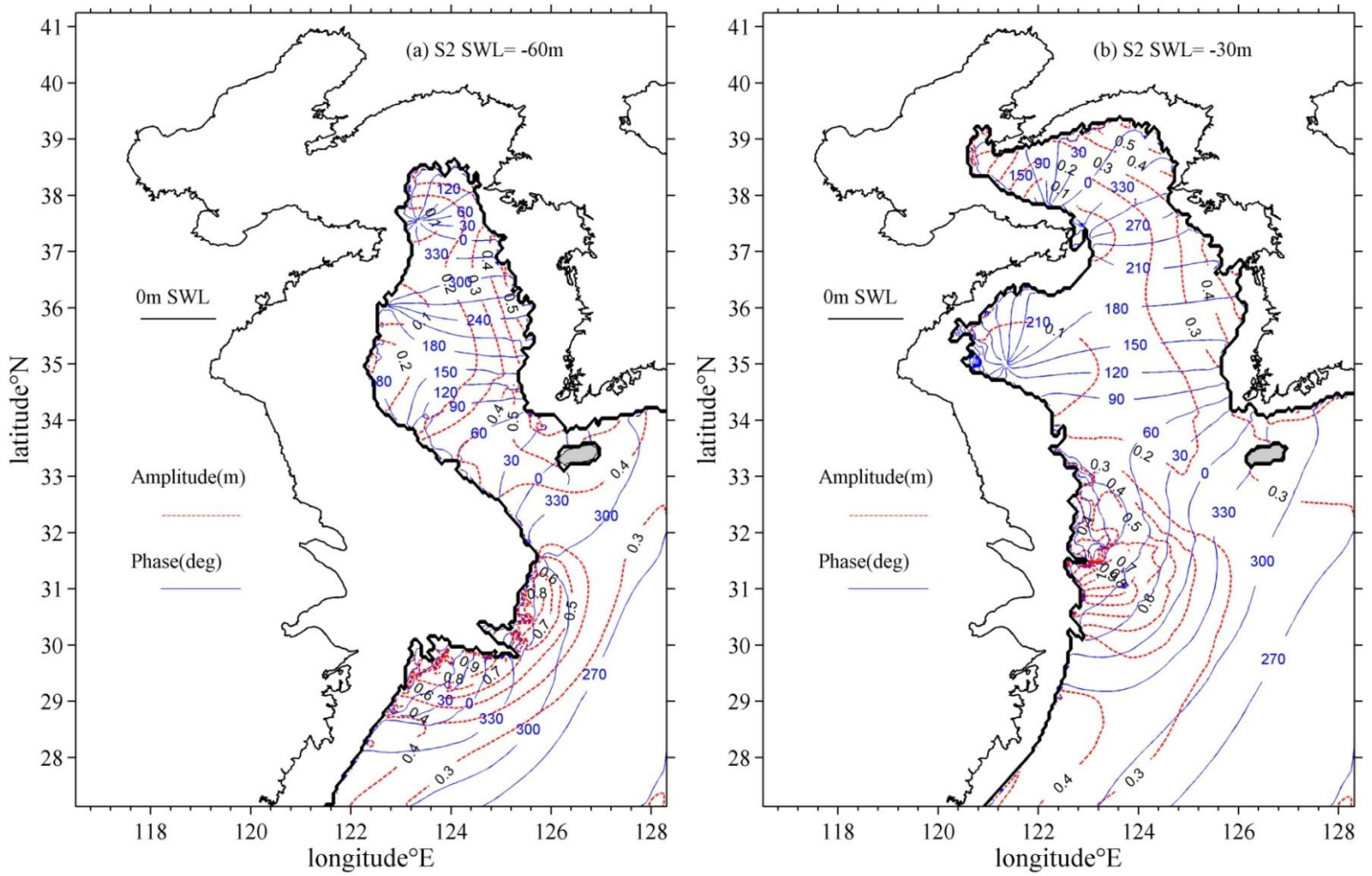

Fig. 5.15 Co-tidal chart of the calculated S2 constitute for sea water level (a)-60m (b) -30m, blue lines show co-phase lines with 30 °interval

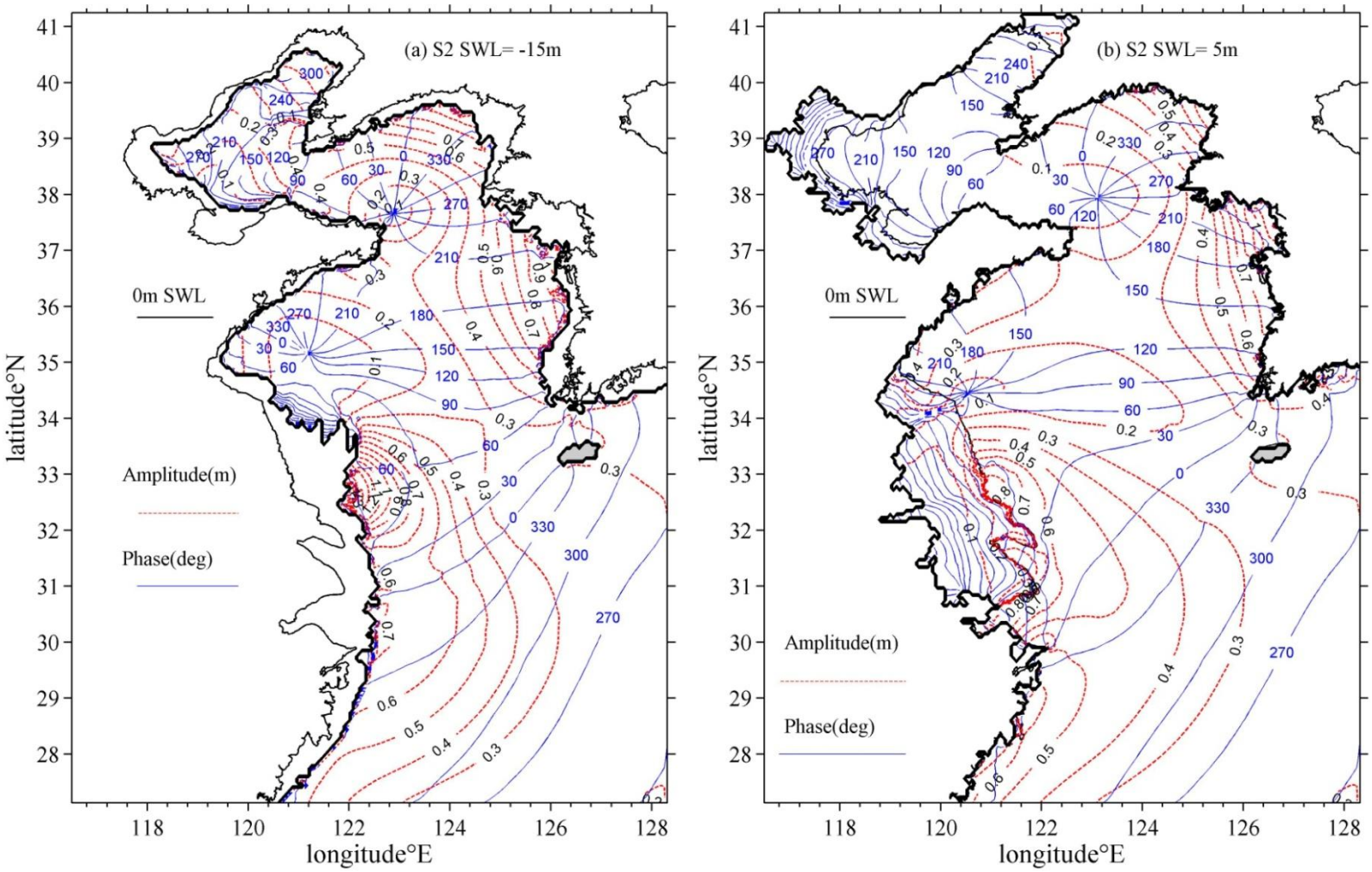

Fig. 5.16 Co-tidal chart of the calculated S2 constitute for sea water level (a)-15m (b) 5m, blue lines show co-phase lines with 30 °interval

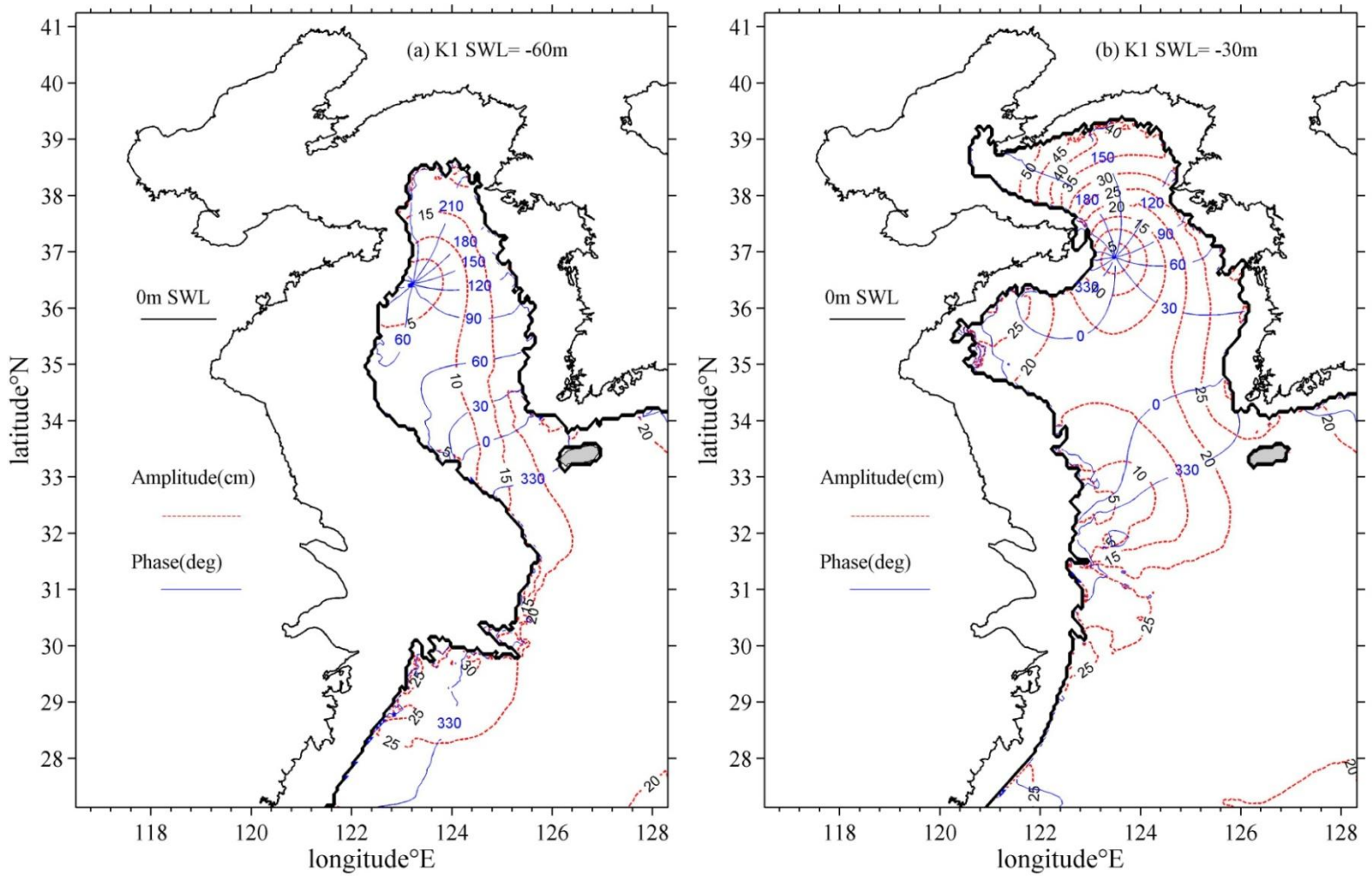

Fig. 5.17 Co-tidal chart of the calculated K1 constitute for sea water level (a)-60m (b) -30m, blue lines show co-phase lines with 30 °interval

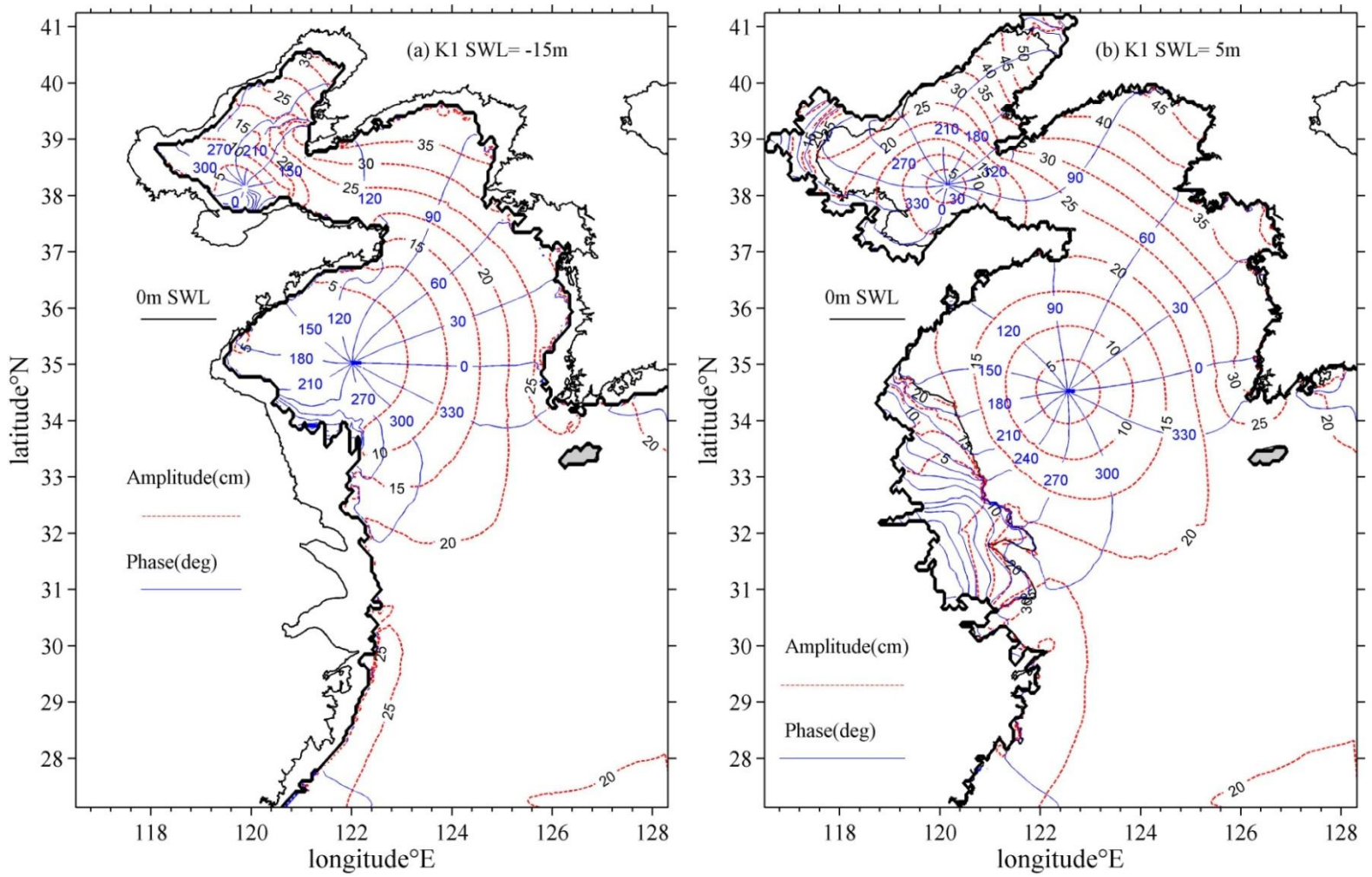

Fig. 5.18 Co-tidal chart of the calculated K1 constitute for sea water level (a)-15m (b) 5m, blue lines show co-phase lines with 30 °interval

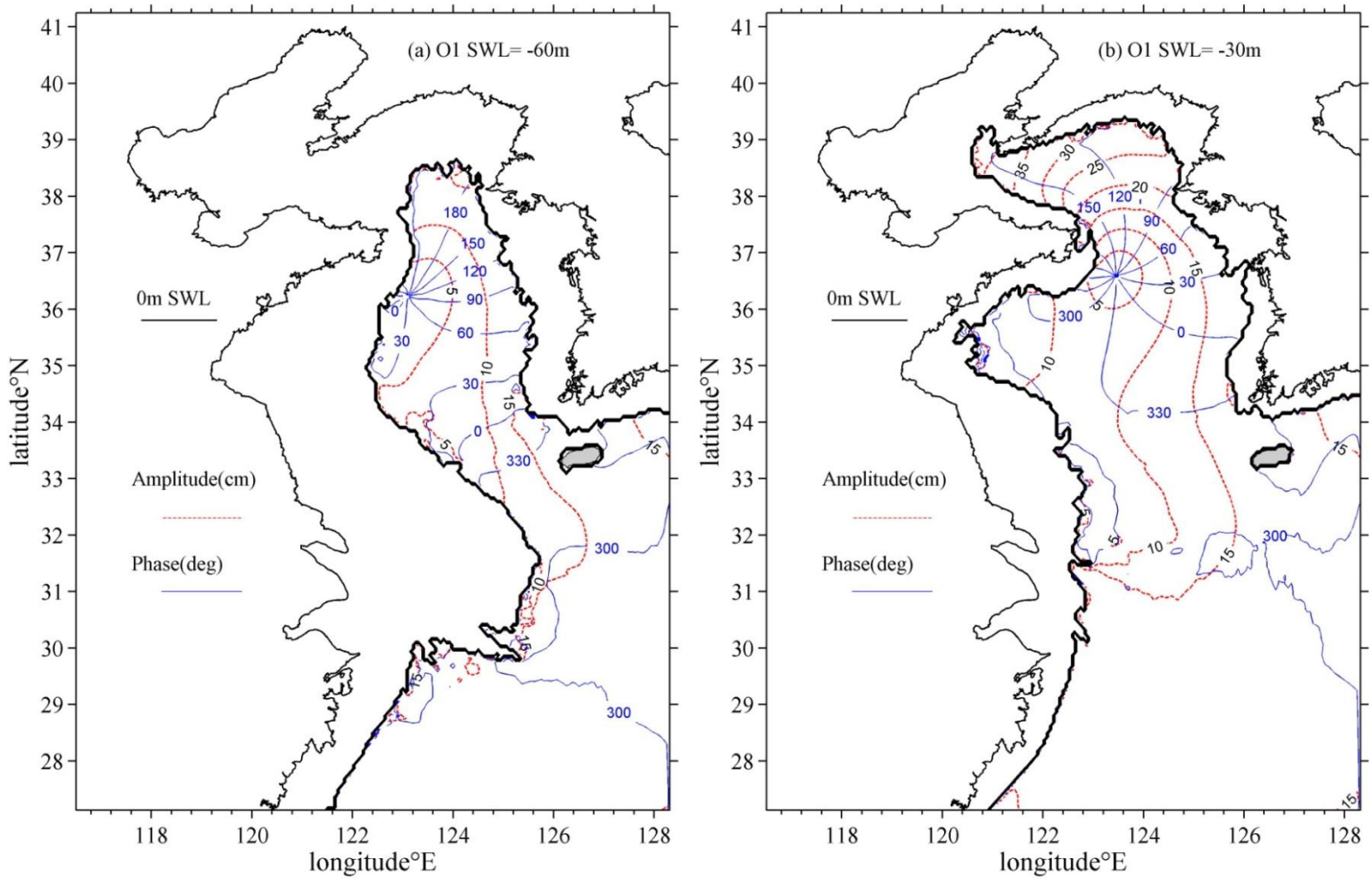

Fig. 5.19 Co-tidal chart of the calculated O1 constitute for sea water level (a)-60m (b) -30m, blue lines show co-phase lines with 30 °interval

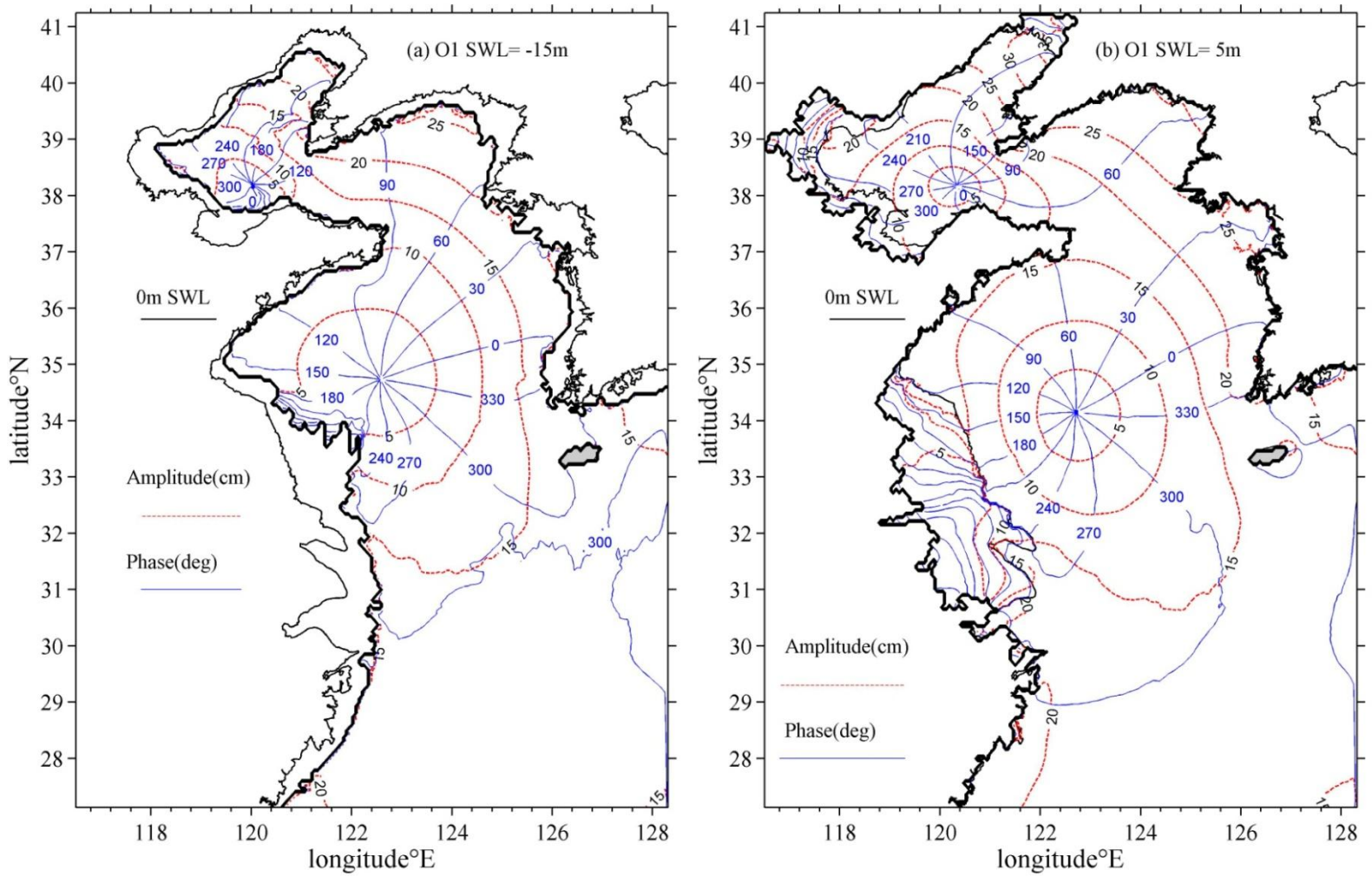

Fig. 5.20 Co-tidal chart of the calculated O1 constitute for sea water level (a) -15m (b) 5m, blue lines show co-phase lines with 30 °interval

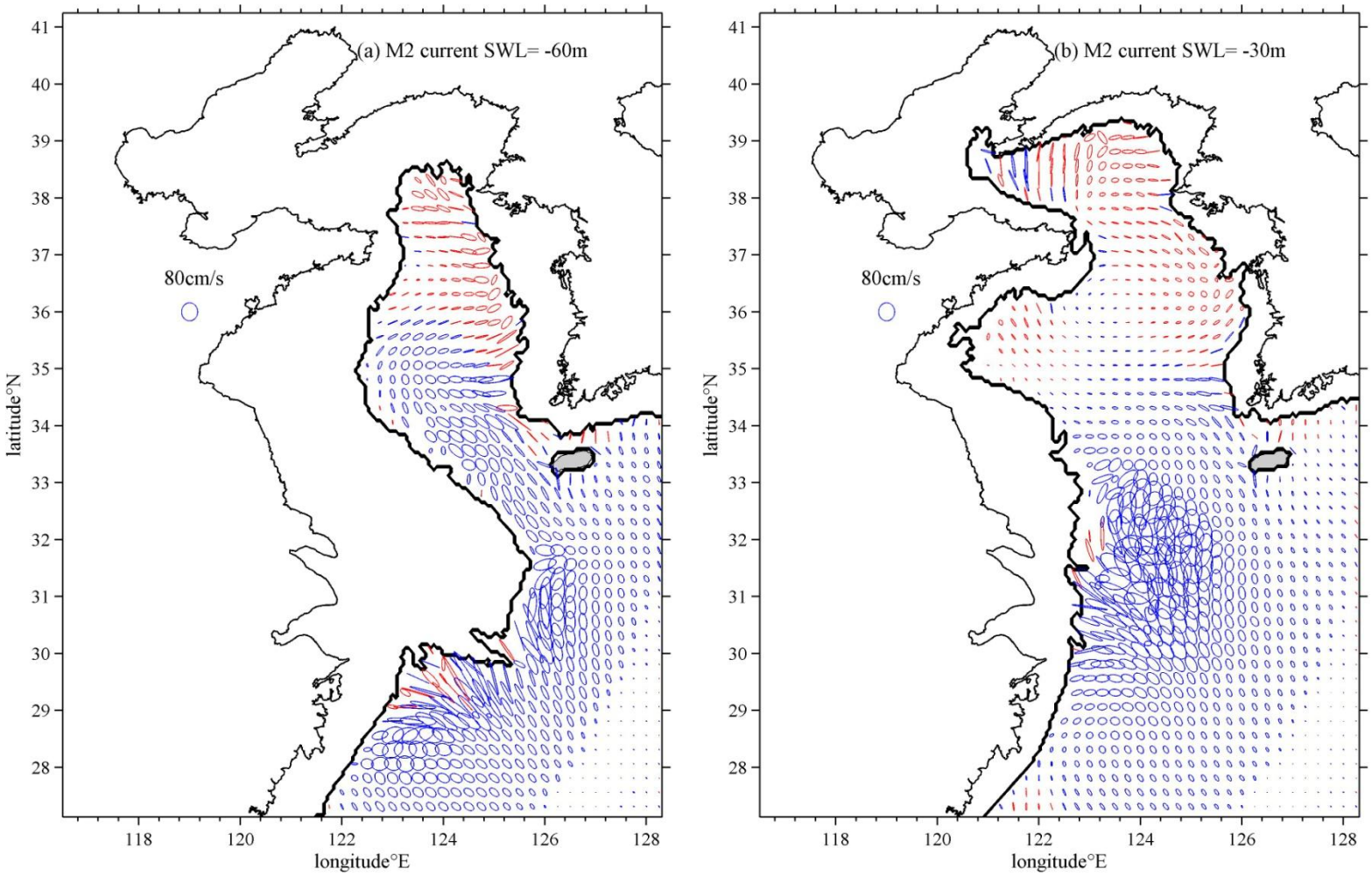

Fig. 5.21 Tidal current ellipse of M2 constitute for sea water level (a) -60m (b) -30m (Blue- clockwise; Red-anticlockwise)

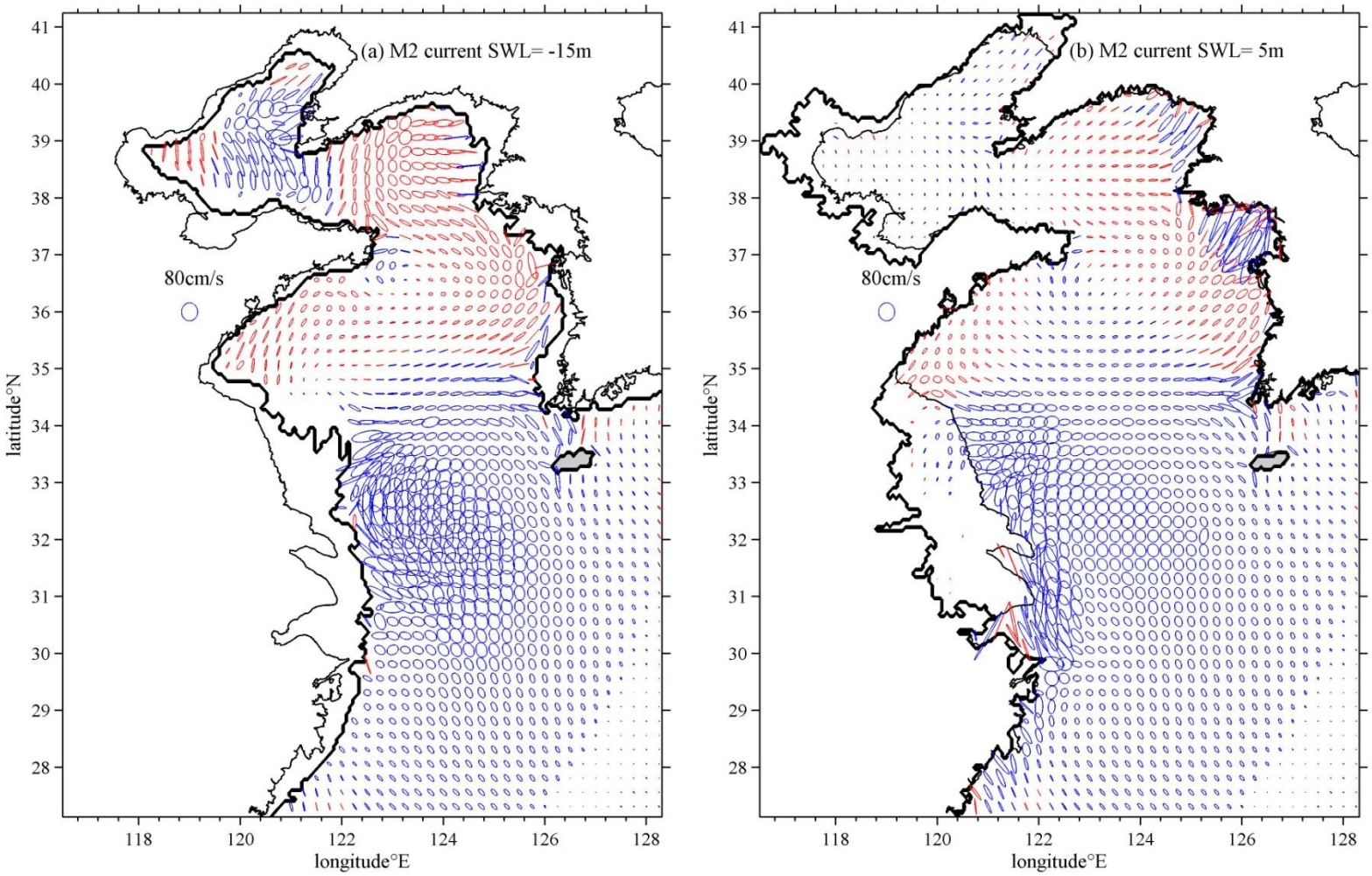

Fig. 5.22 Tidal current ellipse of M2 constitute for sea water level (a) -15m (b) 5m (Blue- clockwise; Red-anticlockwise)

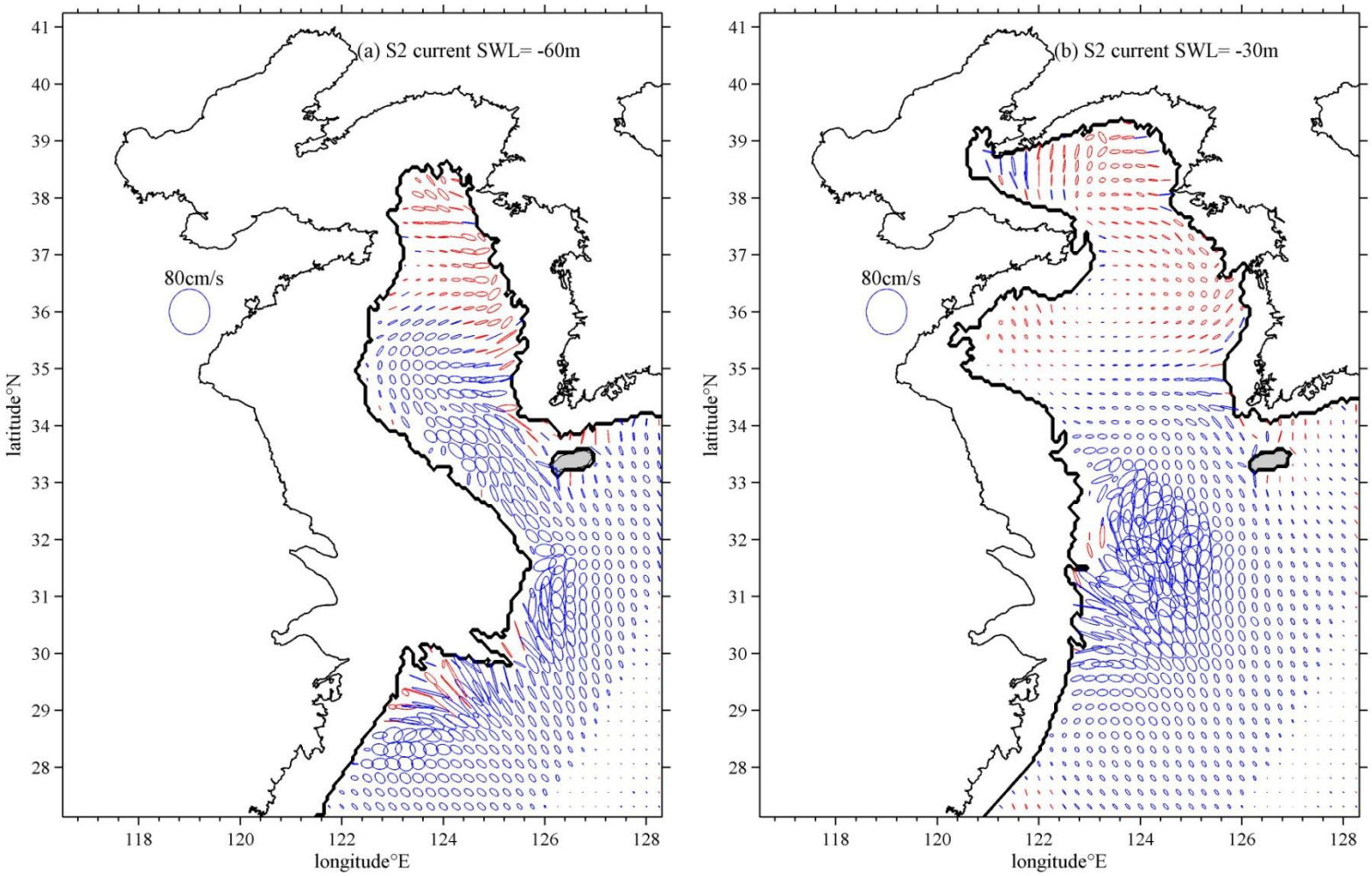

Fig. 5.23 Tidal current ellipse of S2 constitute for sea water level (a) -60 m (b) -30m (Blue- clockwise; Red-anticlockwise)

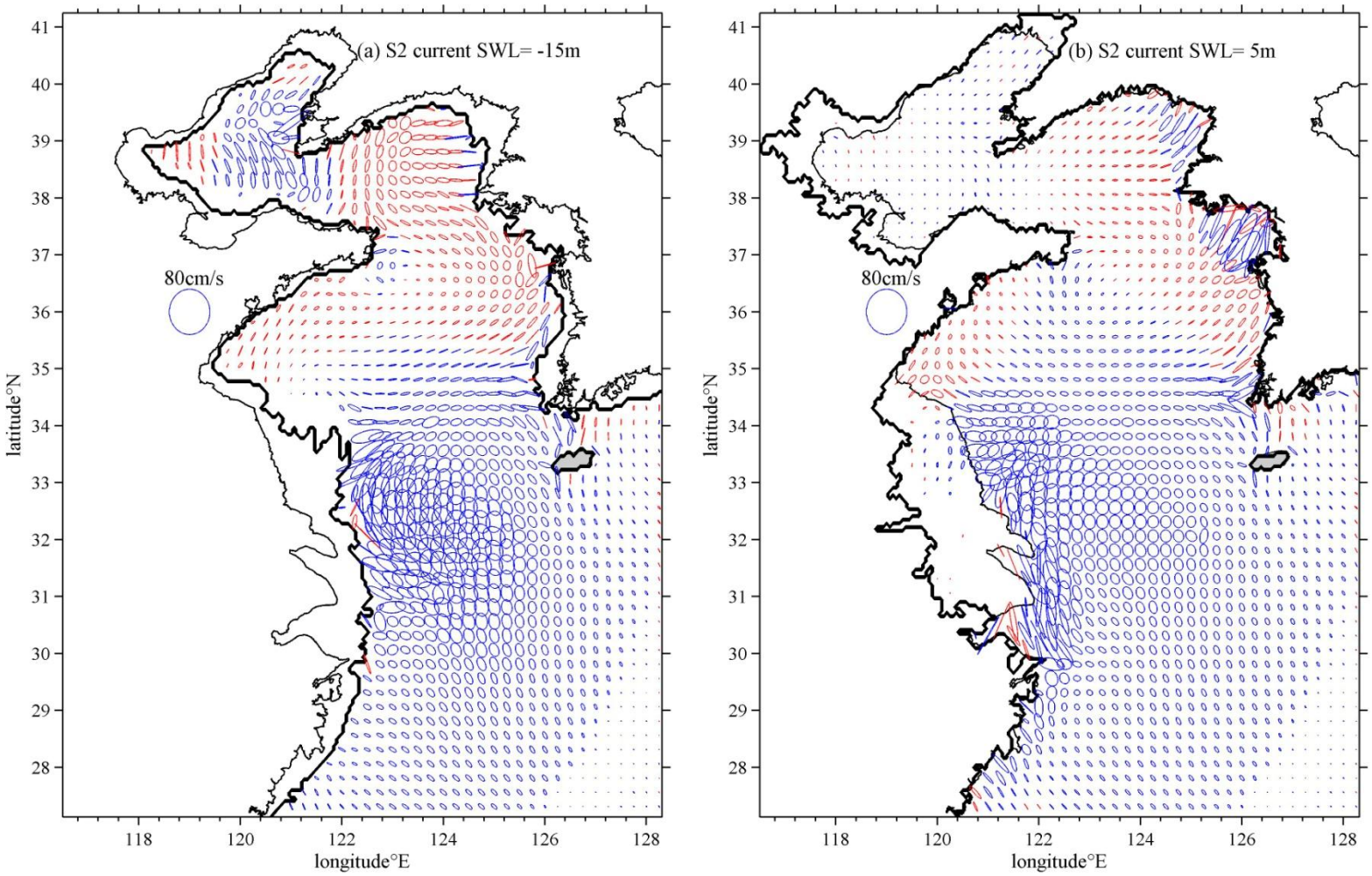

Fig. 5.24 Tidal current ellipse of S2 constitute for sea water level (a) -15 m (b) 5m (Blue- clockwise; Red-anticlockwise)

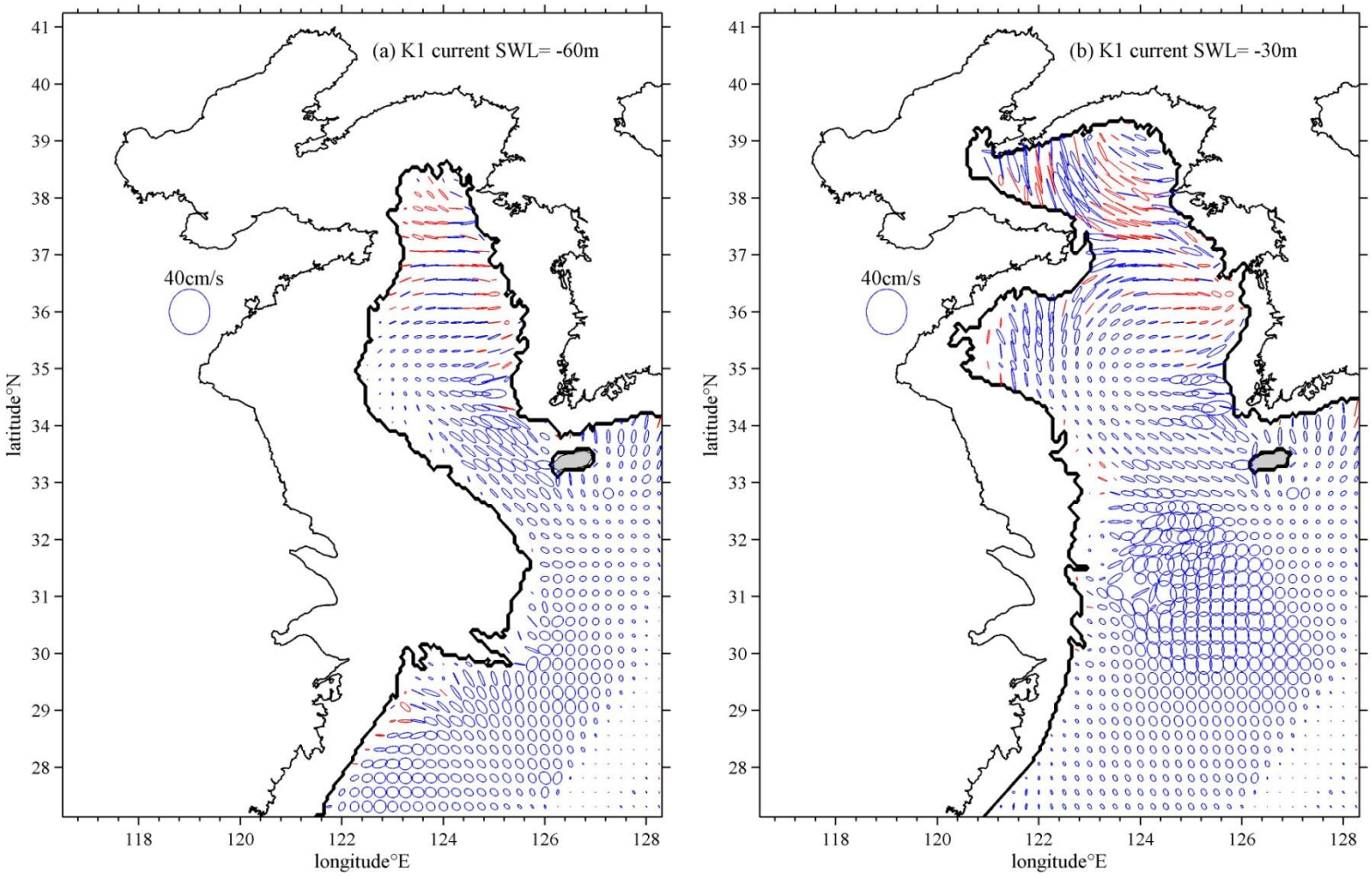

Fig. 5.25 Tidal current ellipse of K1 constitute for sea water level (a) -60 m (b) -30m (Blue- clockwise; Red-anticlockwise)

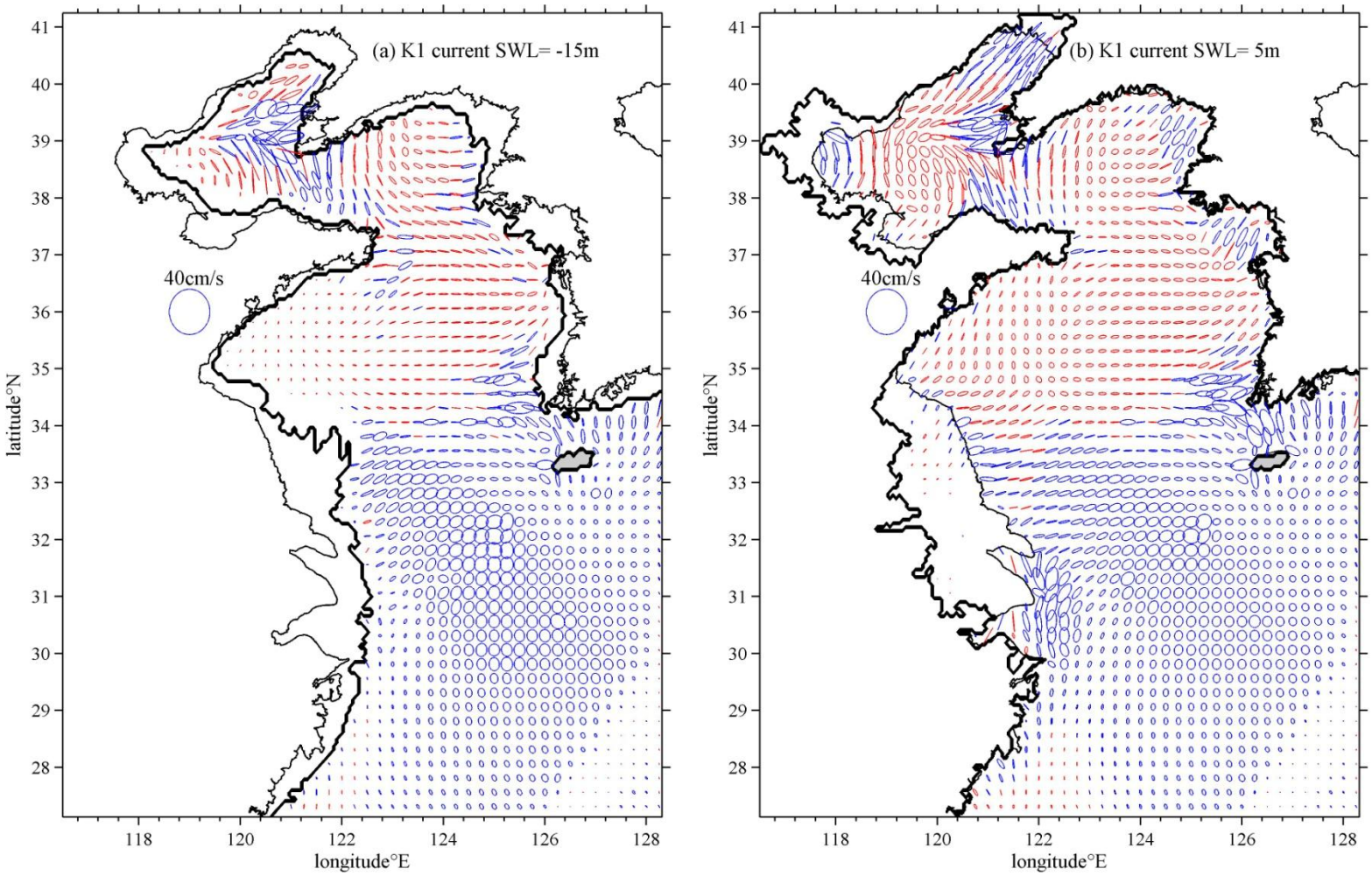

Fig. 5.26 Tidal current ellipse of K1 constitute for sea water level (a) -15 m (b) 5m (Blue- clockwise; Red-anticlockwise)

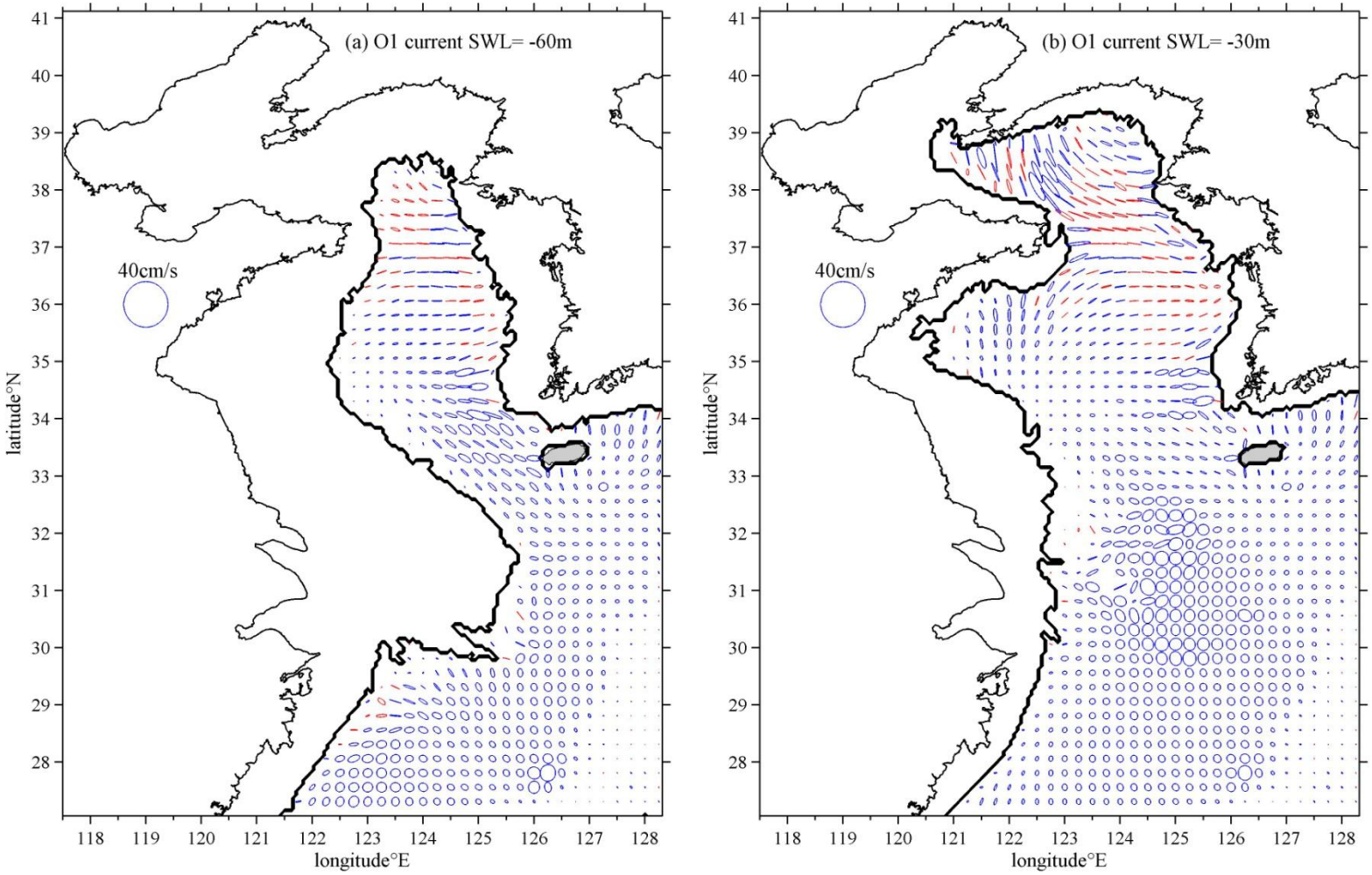

Fig. 5.27 Tidal current ellipse of O1 constitute for sea water level (a) -60 m (b) -30m (Blue- clockwise; Red-anticlockwise)

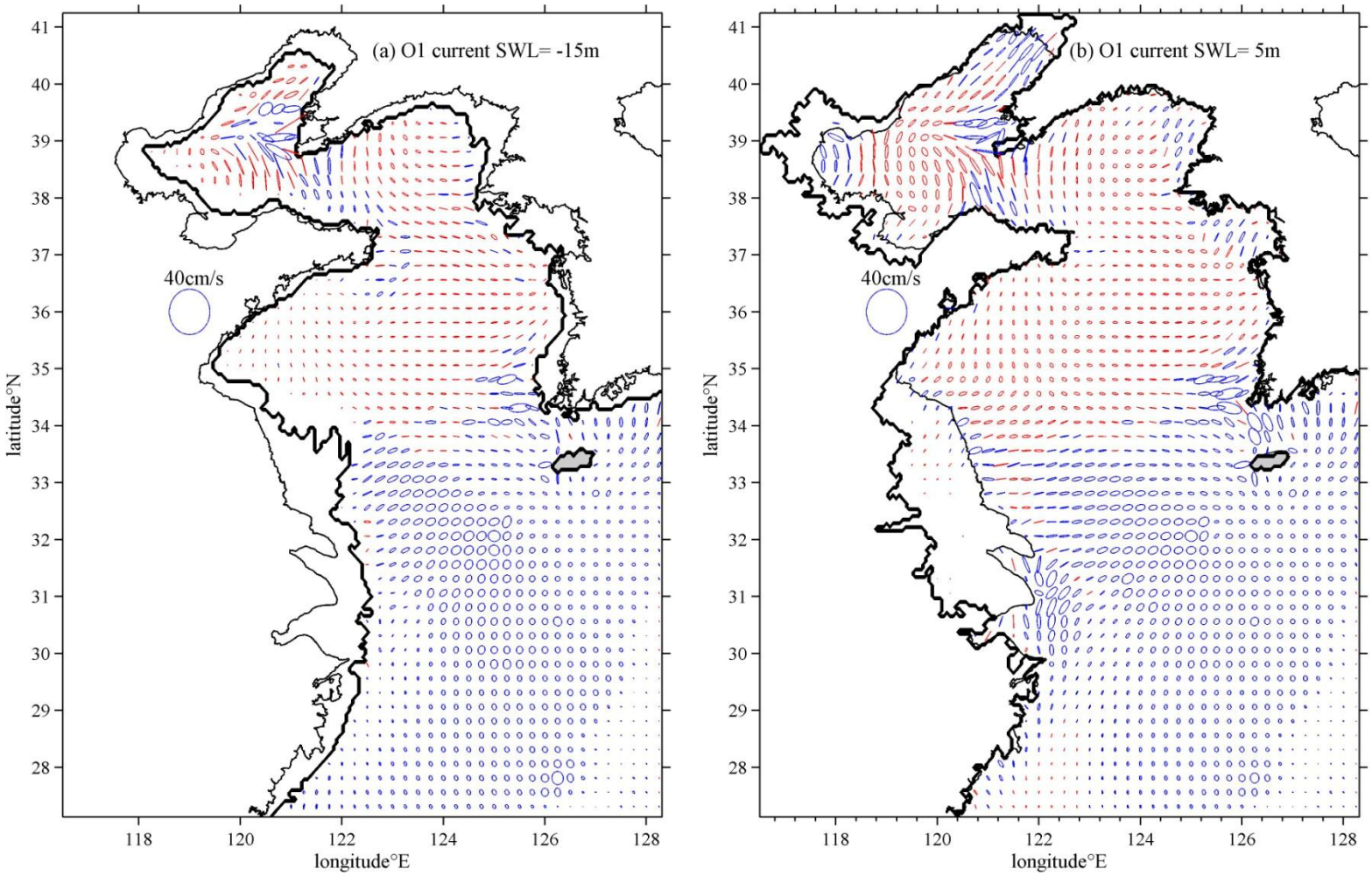

Fig. 5.28 Tidal current ellipse of O1 constitute for sea water level (a) -15 m (b) 5m (Blue- clockwise; Red-anticlockwise)

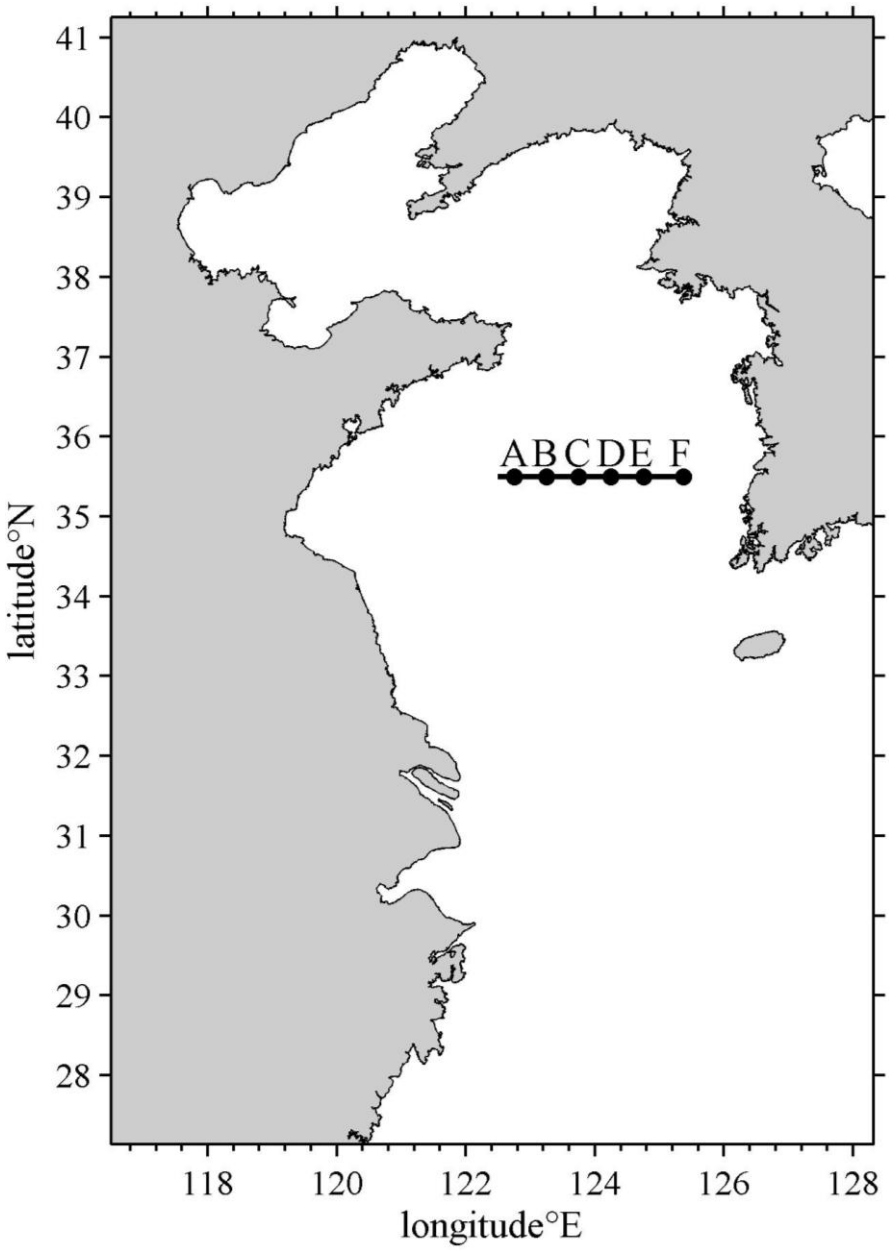

Fig. 5.29 Points position in the CYSM area

A few deposition points along the 35.5 ℃N through the CYSM area (Fig. 5.29) are chosen to look at the change details over the history. The M2 current ellipse long axis values of points under different sea levels are shown in Fig. 5.30.

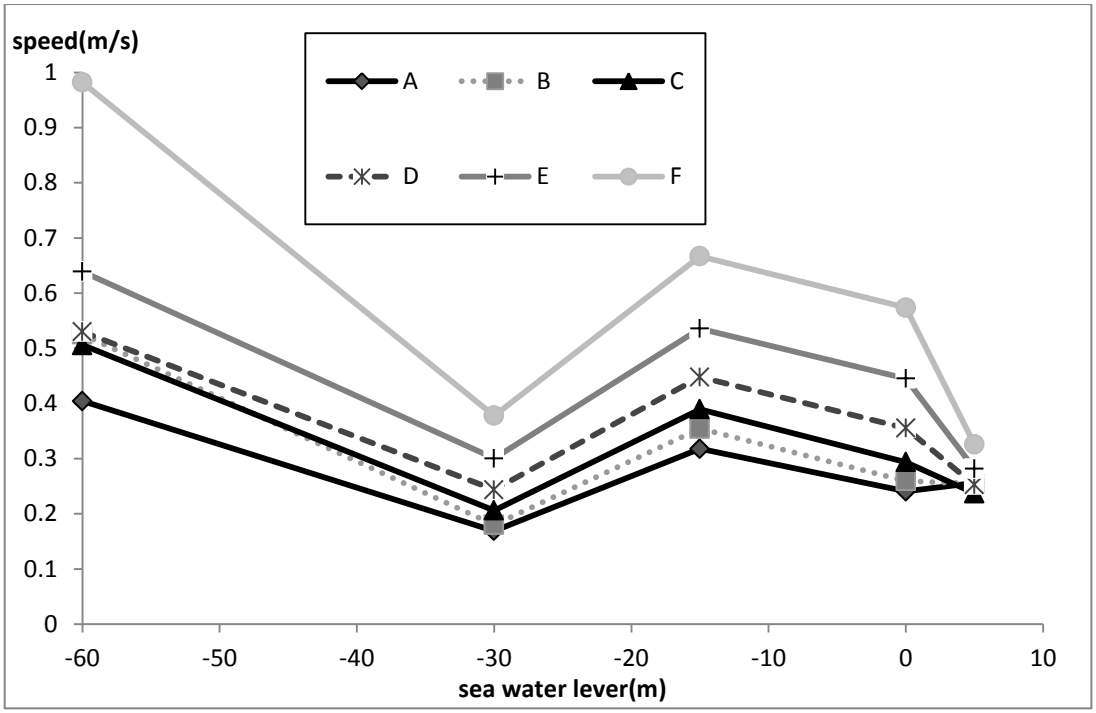

Fig. 5.30 M2 current ellipse long axis values of points under different sea levels

The values are generally decreased as sea level rising except for the sea level of 30m below present, mainly because most tidal energy is dissipated around the palaeo-Changjiang area under that specific geometry of sea level -30m. The tidal current value decreased gently since sea level of -15m, indicating that steady environment was built since 9, 000 years and the tidal current were very weak at the CYSM deposit area (point A B C).

5.2 **Shelf circulation**

The numerical model circulation in the YECS is driven only by the strong Kuroshio Current, which flows from southwest to the northeast along the continental slope all the year round, and East Asian Monsoon, without tide forcing. Typical East Asian monsoon in the Yellow Sea causes southerly and southwesterly winds during summer, northerly and northeasterly winds during winter. Besides, the temperature and salinity is relaxed to monthly mean sea surface temperature and monthly mean sea surface salinity respectively.

5.2.1 **Seasonal current patterns**

The current circulation patterns show considerable seasonal variations (Fig. 5.31). The seasonal averaged current fields show that in winter (Fig. 5.31(a)), the Kuroshio-driven current extends from the Taiwan Strait all the way into the northern Yellow Sea. The Yellow Sea Warm Current intrudes northwards to the Yellow Sea from the southwest of the Cheju Island. A little part of the Yellow warm current flows into the Bohai Sea, and most of it turn to the east and flow southward along the West Korea coast, forming the west Korea coastal current. The Yellow Sea coastal current flows southwards along the East China Sea coast. The model results are in good agreement with the field observation (Tang *et al.*, 2000).

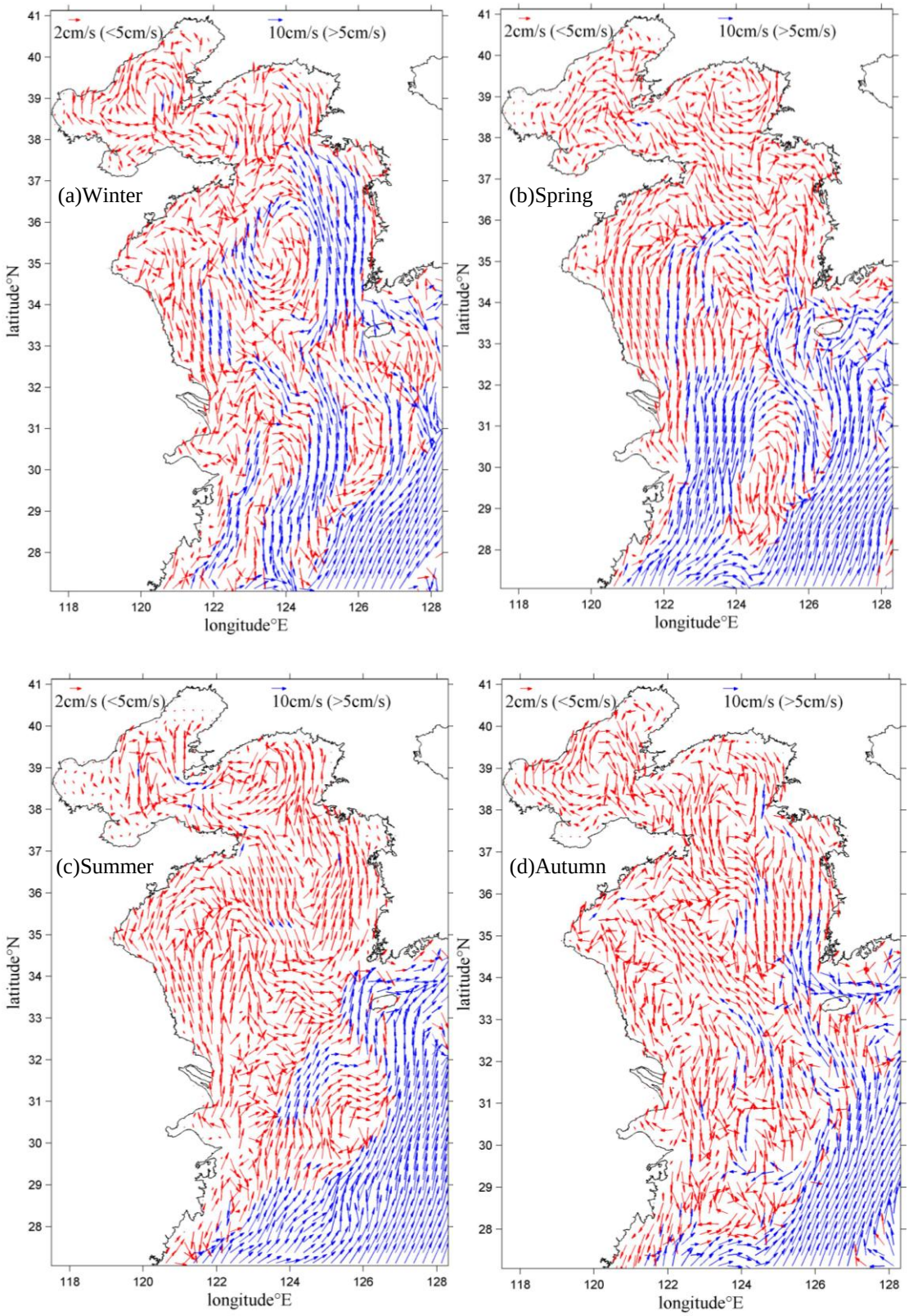

Fig. 5.31 The surface circulation in the Yellow Sea and the East China Sea at four seasons

In spring, the Yellow Sea Warm current can reach the Southern Yellow Sea. The coast current offshore China coast reverse and flows northward while that along the Korea coast remain southward with smaller velocities (Fig. 5.31(b) & Fig. 5.32 (b)).

Fig. 5.31(c) revealed a remarkably different circulation pattern in summer compared with that in winter. Almost no Yellow Sea Warm current can be found in summer and the intrusion to the Yellow sea (Fig. 5.32 (c)). The coastal currents offshore the Korea and China coast reverse and flow northward.

When it comes to autumn, the Yellow Sea Warm Current gets stronger and so does the southward coast current along the Korea coast. The current along the China coast remain northwards with much smaller velocities (Fig. 5.31(d) & Fig. 5.32 (d)).

The shelf circulation in winter, spring and autumn is favourable for transporting sediment from Old Huanghe River delta to the Central Yellow Sea Mud. In winter, the shelf circulation can transport the Huanghe River discharged sediment to the CYSM by resuspending process.

The shelf circulation current shows asymmetric distribution, which indicates that the strong shelf circulation current in the west of Yellow Sea is favourable for resuspending and carrying the sediment from the Chinese coastal are and then the fine sediment is deposited at the weaker shelf circulation current area (the middle Yellow Sea). The eastside current, although strong in winter, the current direction shows carrying sediment southwards to the Cheju island.

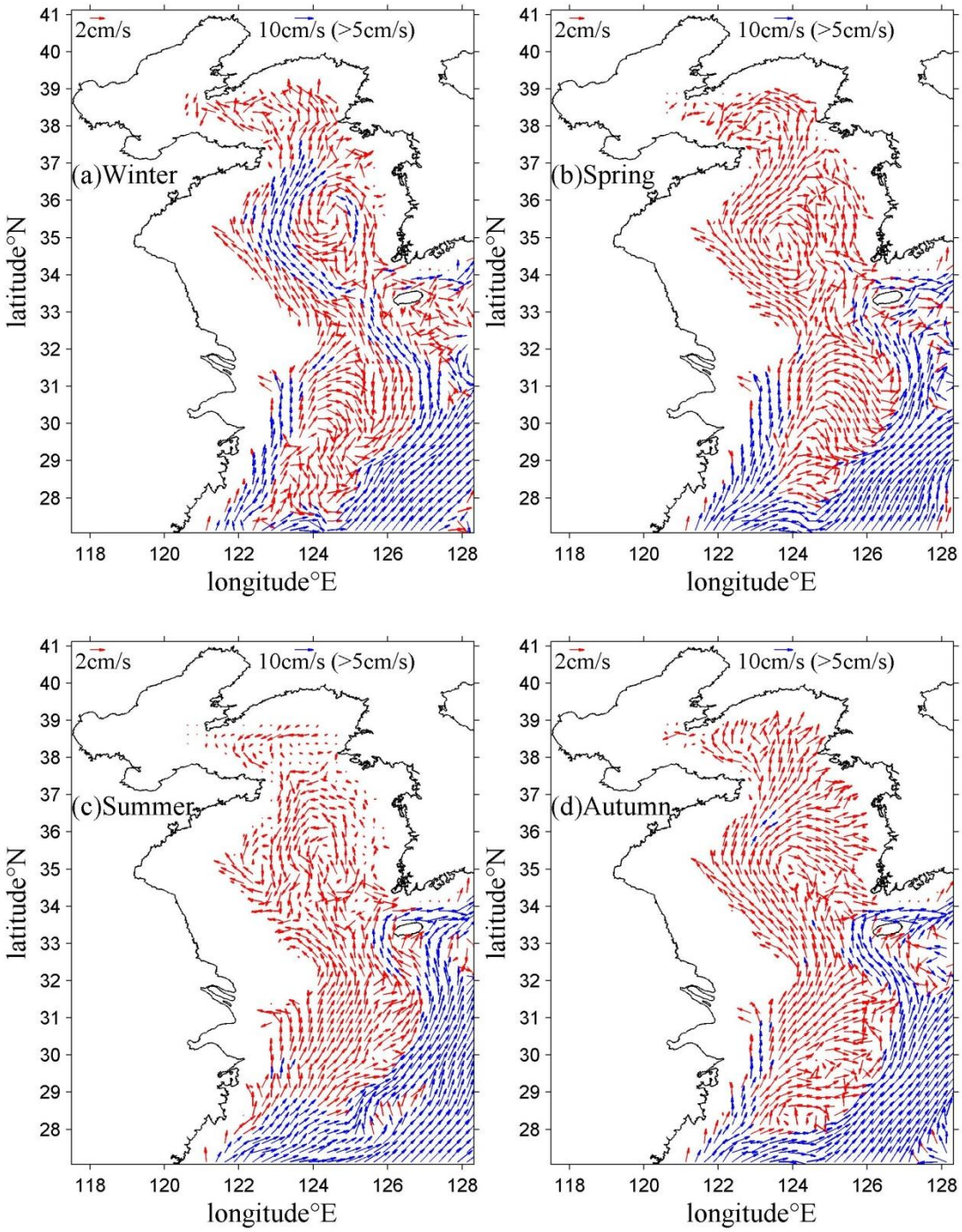

Fig. 5.32 Current at 45 m depth of four seasons.

Fig. 5.33 shows the seasonal shelf circulation induced bottom shear stress, which is quite different from the tidal-induced one (Fig. 5.12). The value is larger in the southeast of East China Sea (but little sediments there), and smaller in the Yellow Sea and coastal area, which indicates that the shelf circulation contributes little to resuspending the sediments in the Yellow Sea.

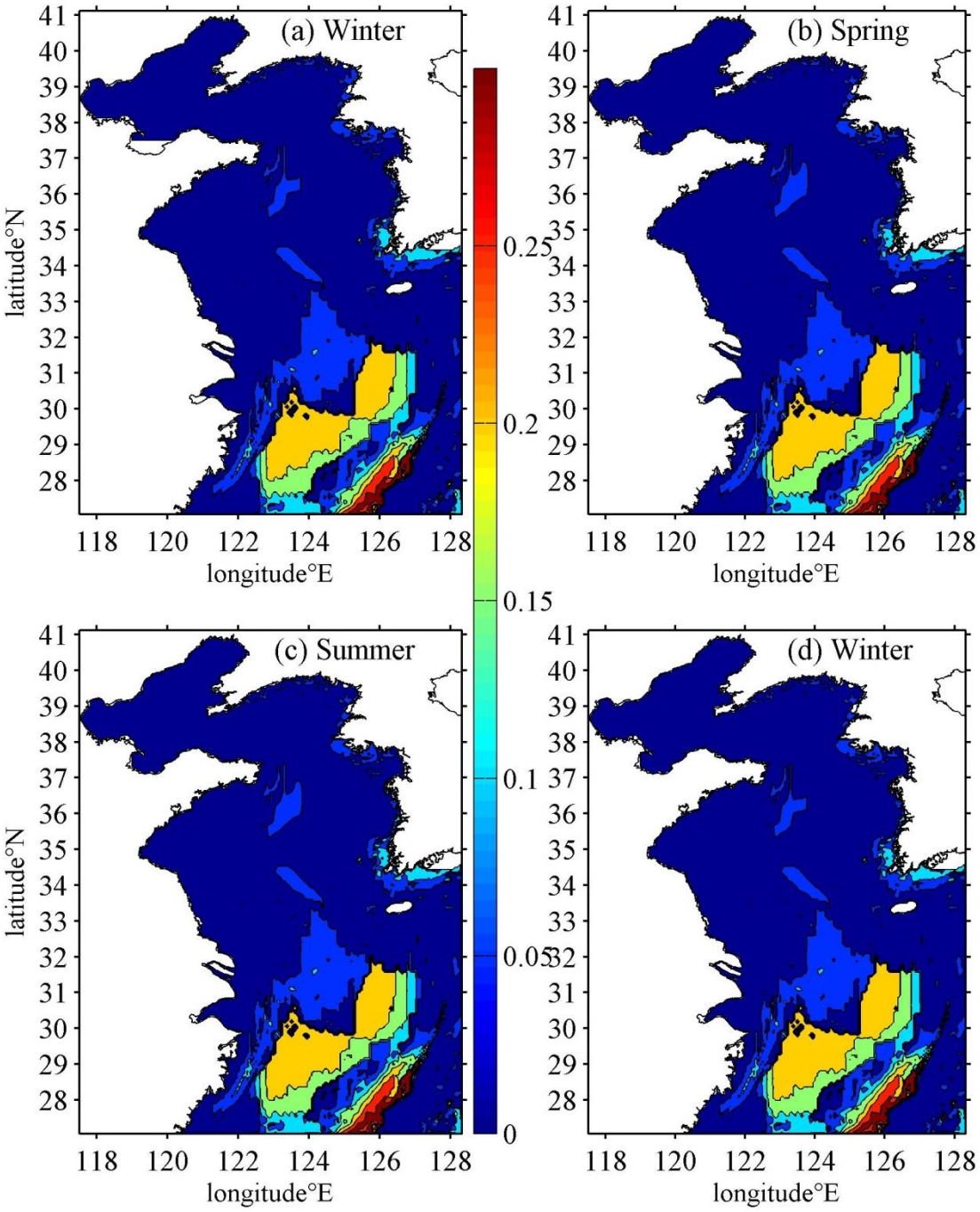

Fig. 5.33 Seasonal shelf circulation induced bottom shear stress (Pa)

5.2.2 **Current without wind**

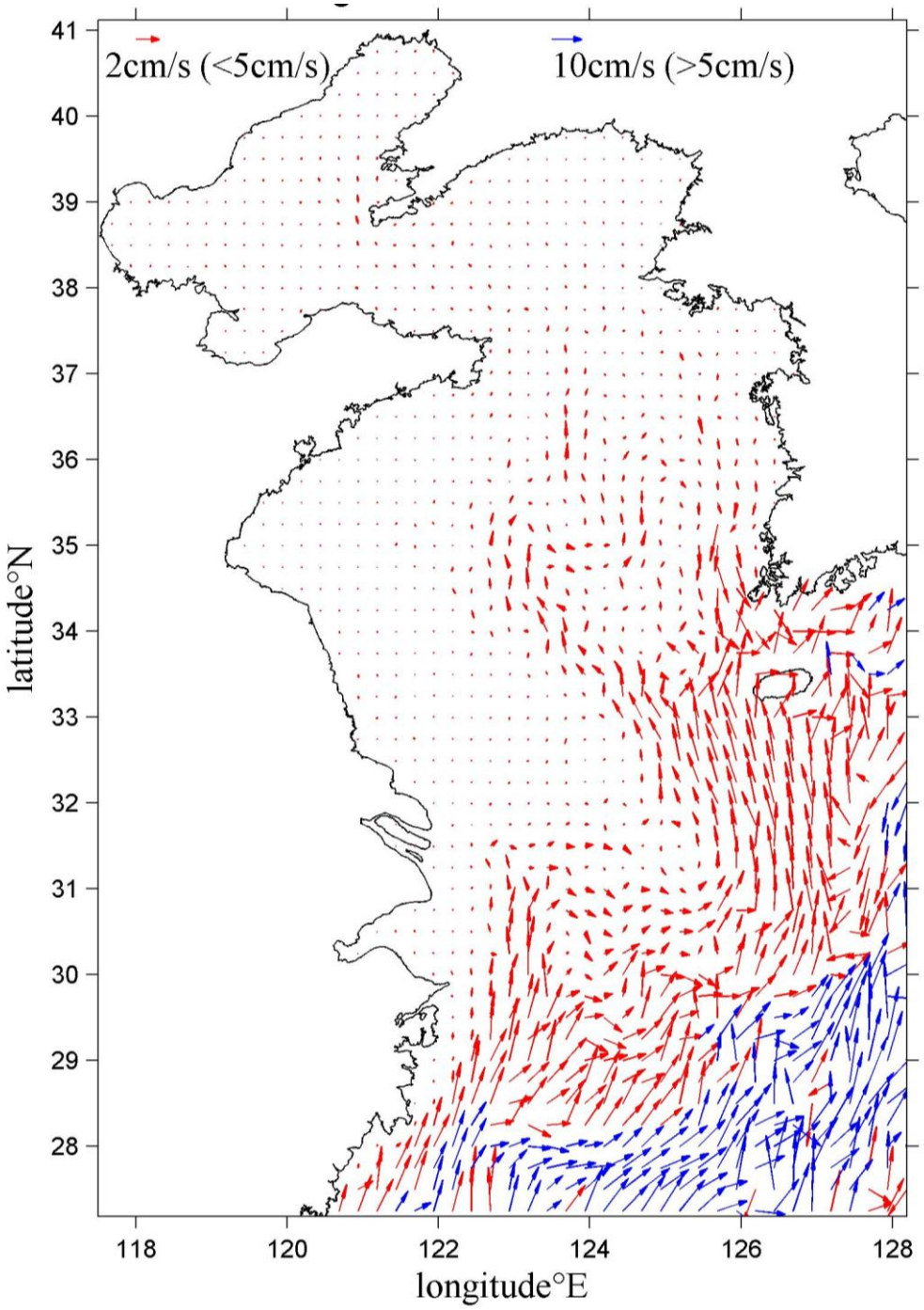

Fig. 5.34 Current circulation without wind in winter

Fig. 5.34 shows the current circulation pattern without wind in winter, forced only by the Kuroshio along the continental slope, the current turned northeast at south of Cheju island, and the circulation in Yellow Sea and East China Sea is generally very weak. It can be inferred that the circulation current alone cannot intrude further north into central southern Yellow Sea, suggesting that prominent circulation pattern

observed in winter over the continental shelf could not have been induced by the through-flow of the Kuroshio in the East China Sea alone.

5.2.3 **Seasonal temperature and salinity distribution**

Seasonal sea temperature field varied a lot as shown in Fig. 5.35&Fig. 5.36. In winter, two warm water tongues related to the Yellow Warm Current are very obvious: one is along the westward of Yellow Sea trough and the other is heading northwestward toward the Shandong coast line. The warm water axis reaches the most western position of about 122.5 °E in 35 °N. To north of 35 °N, the warm water intrusion is basically along the bathymetry. In summer, the temperature field is characterized by the Yellow Sea Cold Water Mass, which is a cold mass under the thermocline in the Yellow Sea as shown in Fig. 5.36 at depth of 20m. Spring and autumn temperature field are in transitional condition between the winter and summer.

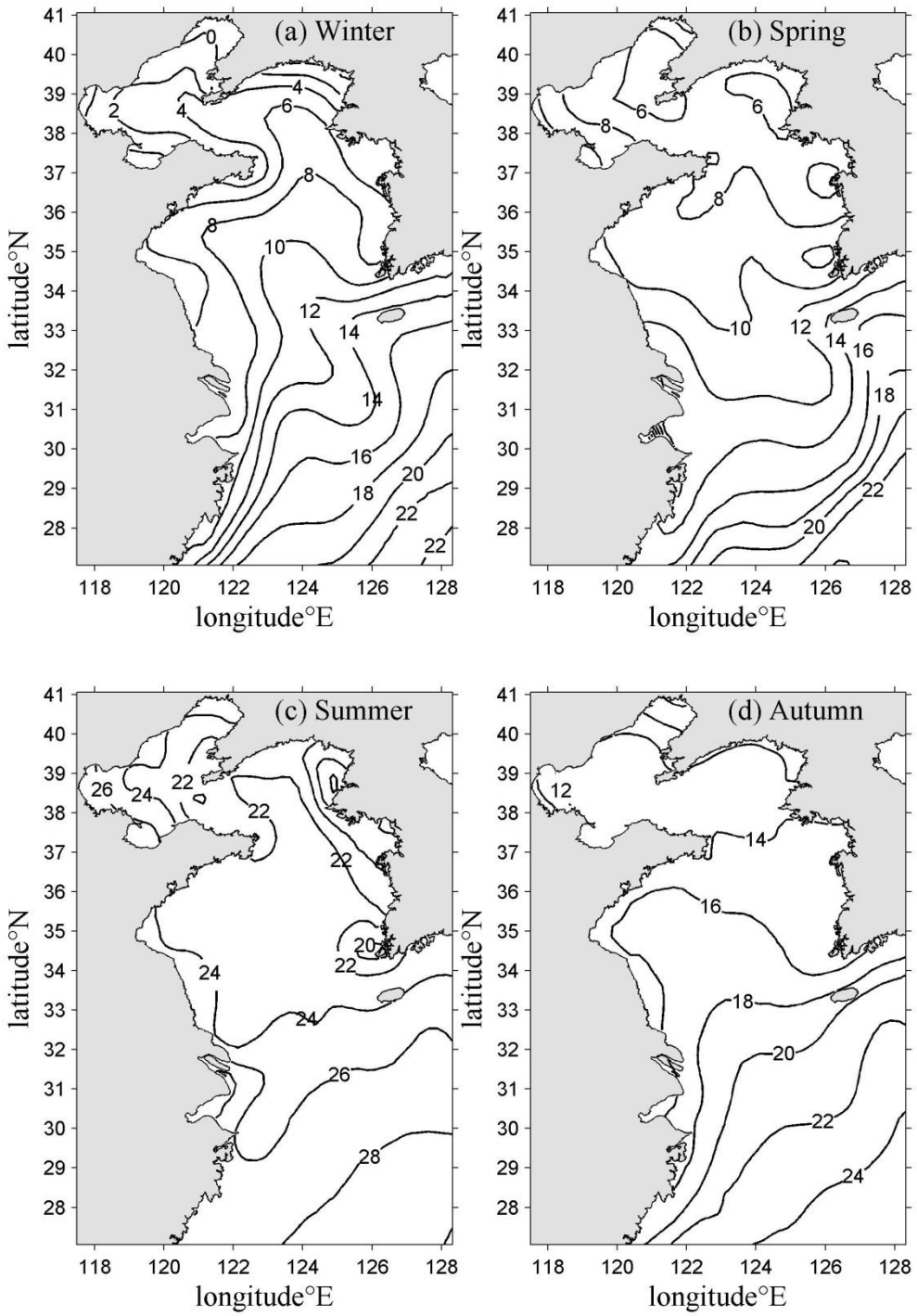

Fig. 5.35 Seasonal sea surface temperature distribution (℃)

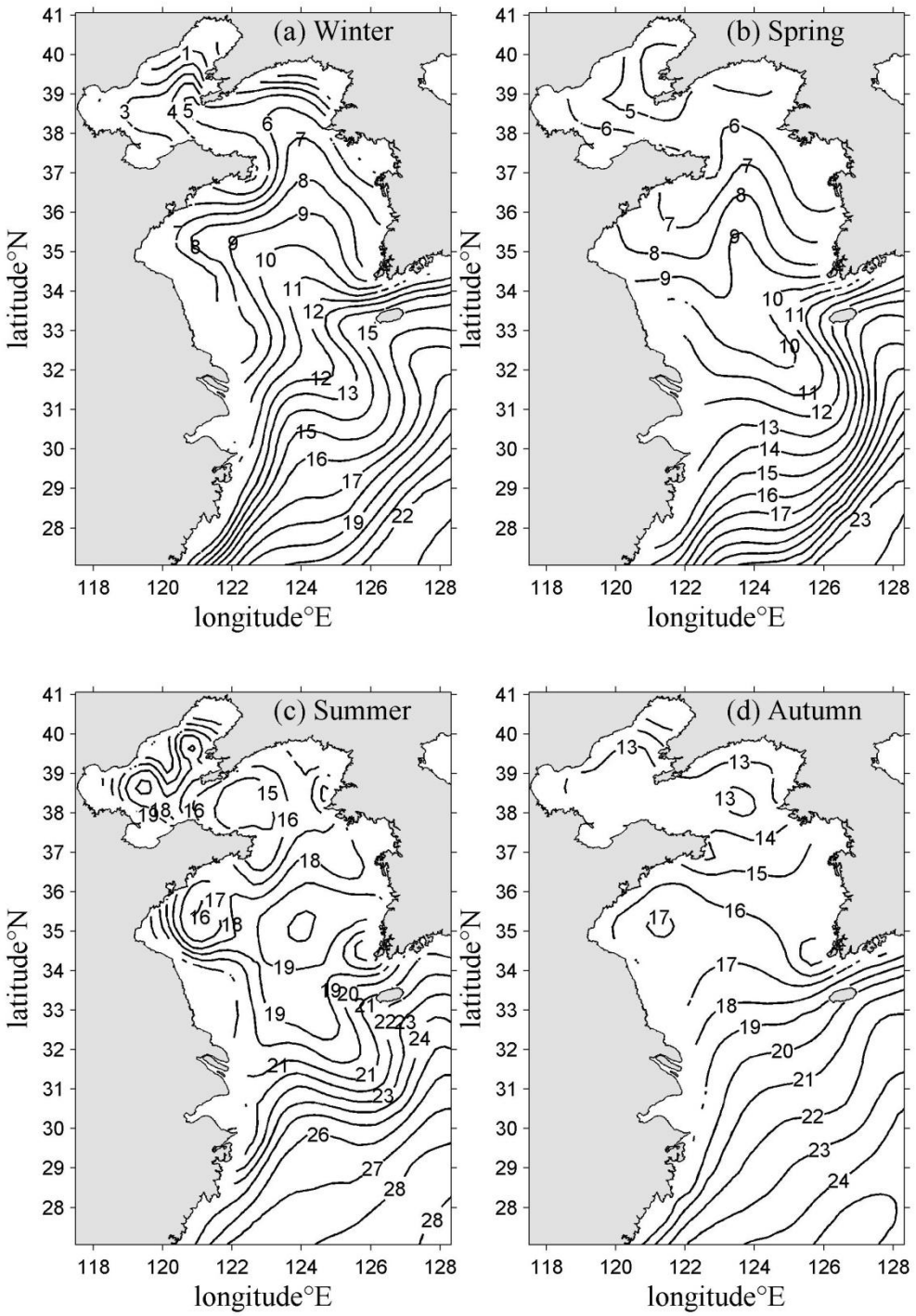

Fig. 5.36 Seasonal sea temperature distribution at depth of 20m (℃)

5.3 **Wave**

Fig. 5.37 shows distribution of wind at the four seasons at YECS. It is clear that the YECS is dominated by East Asian monsoonal wind. In the winter, northerly winds

from the Asian mainland are strong (9-10m/s), and southerly wind from the ocean with average speed of 5-6m/s prevails in the summer.

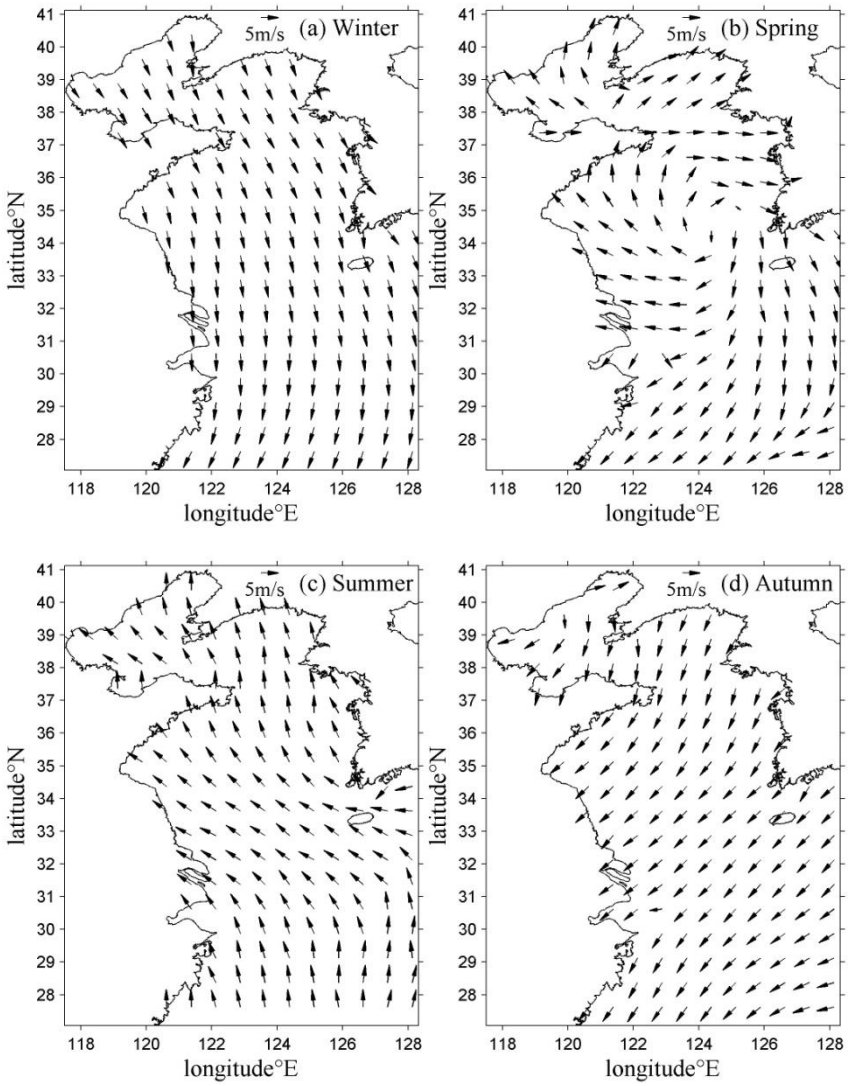

Fig. 5.37 Climatological monthly mean wind over the Yellow and East China Sea area.

5.3.1 **Wave parameters of four seasons**

Fig. 5.38-Fig. 5.40 show the distribution of four seasonal mean wave fields. In general, both wave height and wave period decrease from southeast to northwest and from sea to coast. The mean wave height in the south area is statistically larger than those in the north area, no matter which direction wind comes from. For the north wind, with relatively smaller effective wind fetch and water depth, the wave height in the north was smaller than that in the south. However, for the south wind blowing

from the equator ocean, the wave at the south boundary has enough wind fetch to grow and the wave energy was significantly dissipated as the waves propagated towards the north, due to the effects of bay-shape and decreasing water depth, therefore, the mean wave height in the north was still smaller than that in the south.

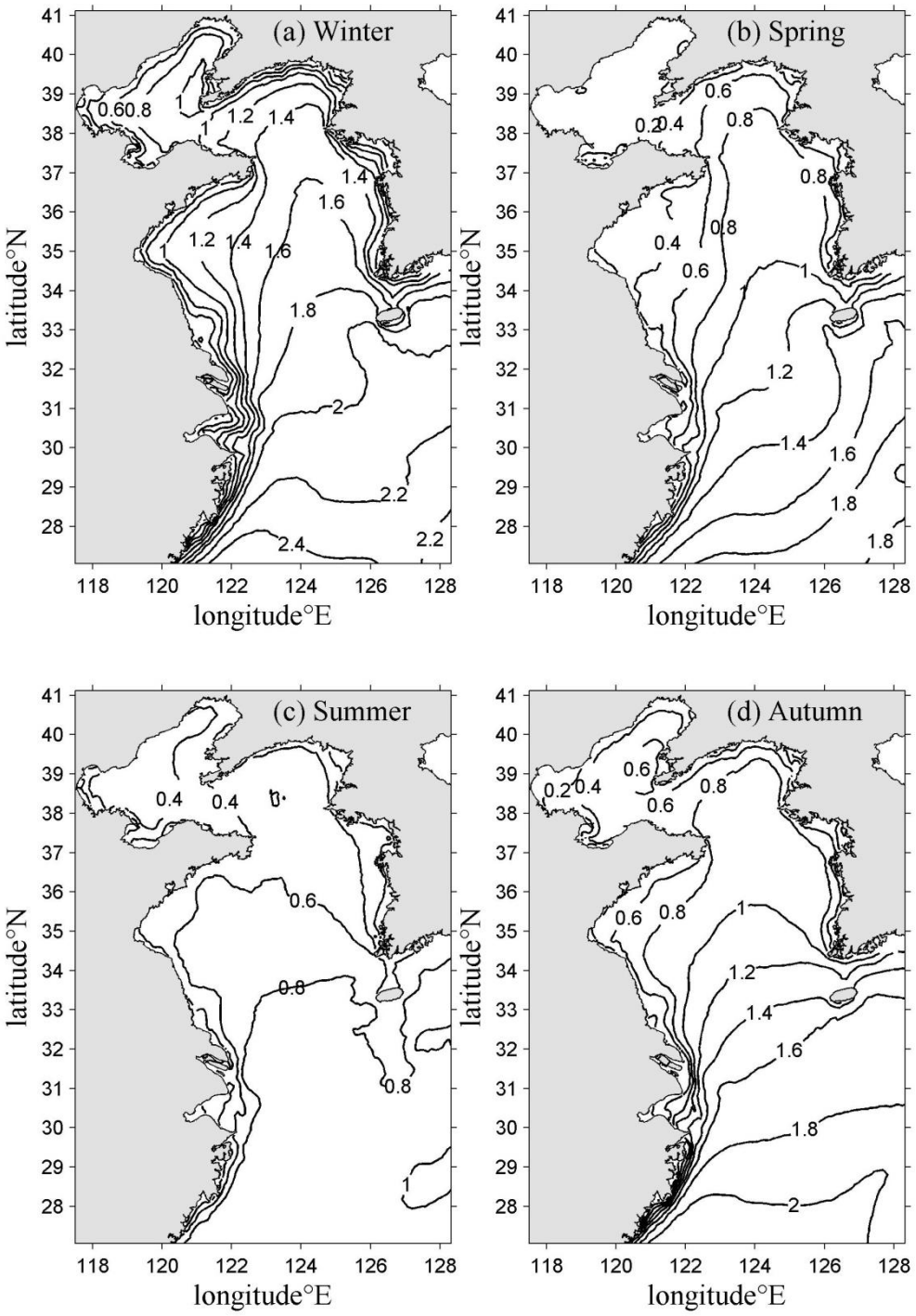

Fig. 5.38 Seasonal mean significant wave height (m)

The mean wave is largest in the winter and smallest in the summer, because of strong northerly wind in winter and relatively smaller southerly wind speed in the summer. The model results of seasonal mean wave statistics are generally consistent with those analysis result of field measurement data (Liu and Sun, 2000; Chen *et al.*, 2006).

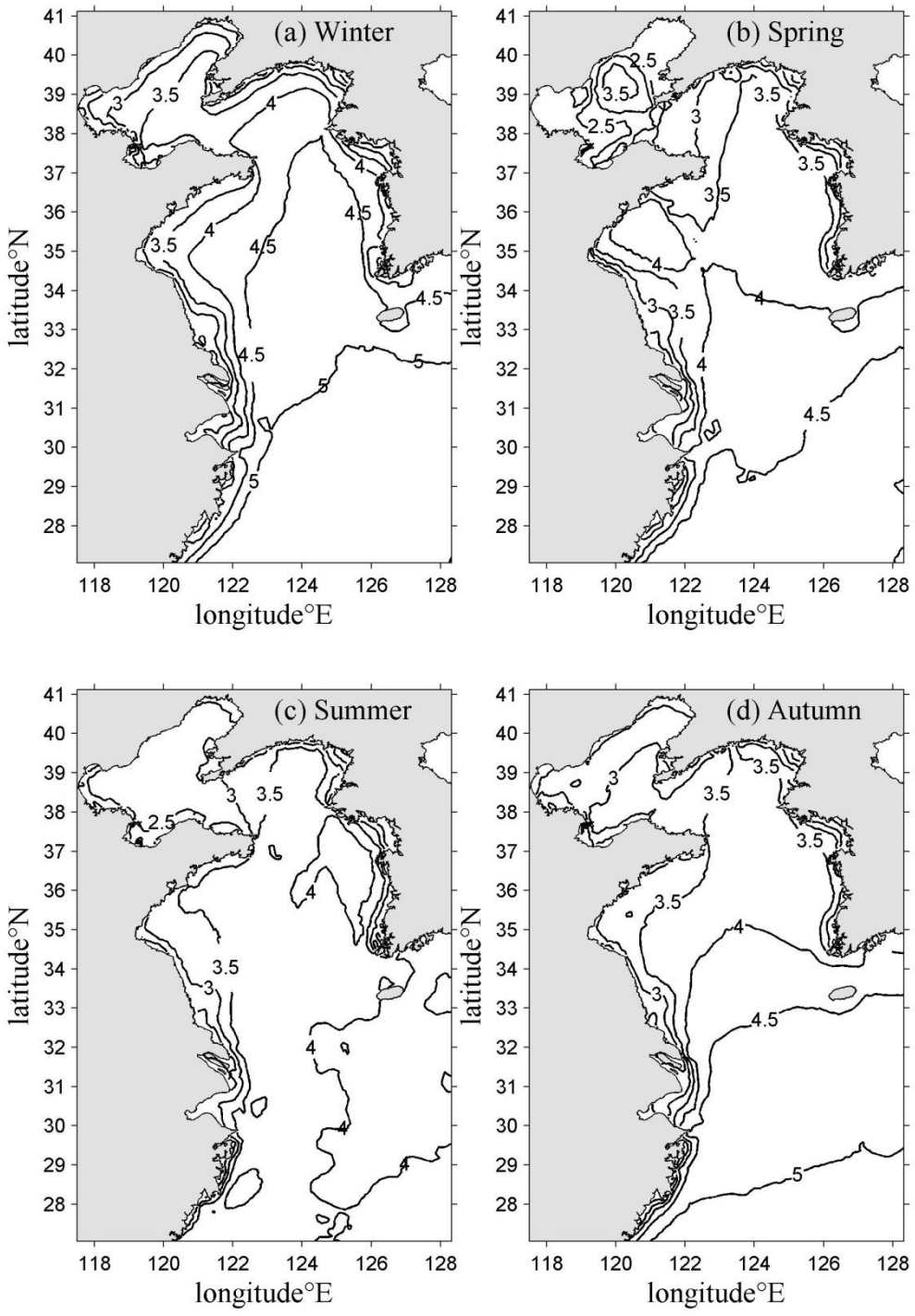

Fig. 5.39 Seasonal mean wave fields of period (second)

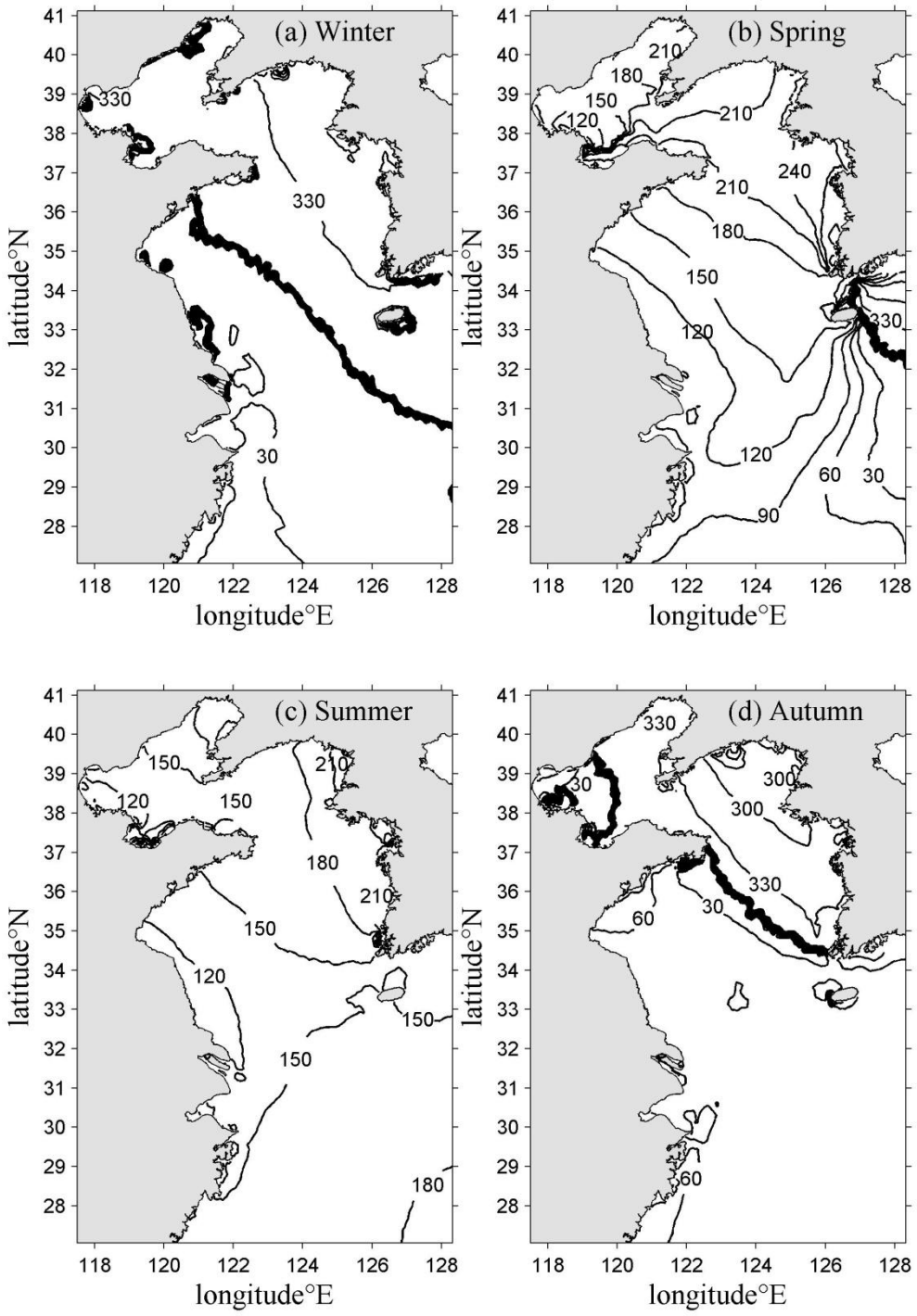

Fig. 5.40 Seasonal mean wave fields of direction (degree)

5.3.2 **Wave induced bottom shear stresses**

the wave induced bottom shear stress is shown in Fig. 5.41. The wave induced bottom shear stress is calculated based on the maximum wave field under monthly

mean wind. The wave induced shear stress is highest in the winter and smallest in the summer, but negligible at depth larger than 30m. Though simulation in the shallow area is least accurate, but accurate enough because of very gentle shelf of Yellow Sea.

In order to investigate the role of wave on the sediment transport, the wave induced shear stress is compared with that induced by tide (Fig. 5.12). Fig. 5.42-Fig. 5.44 show the shaded area where wave/tide induced bottom shear stress ratio is larger than 0.2, 0.5 and 1 respectively.

The wave induced bottom shear stress is quite significant in the coastal area with water depth less than 20m, especially in the Subei coast area (old Huanghe delta) and the modern Huanghe River mouth. Thus, the wave plays a significant role in resuspending the fine sediments there, which are important sediment source for the muddy patches in central Southern Yellow Sea.

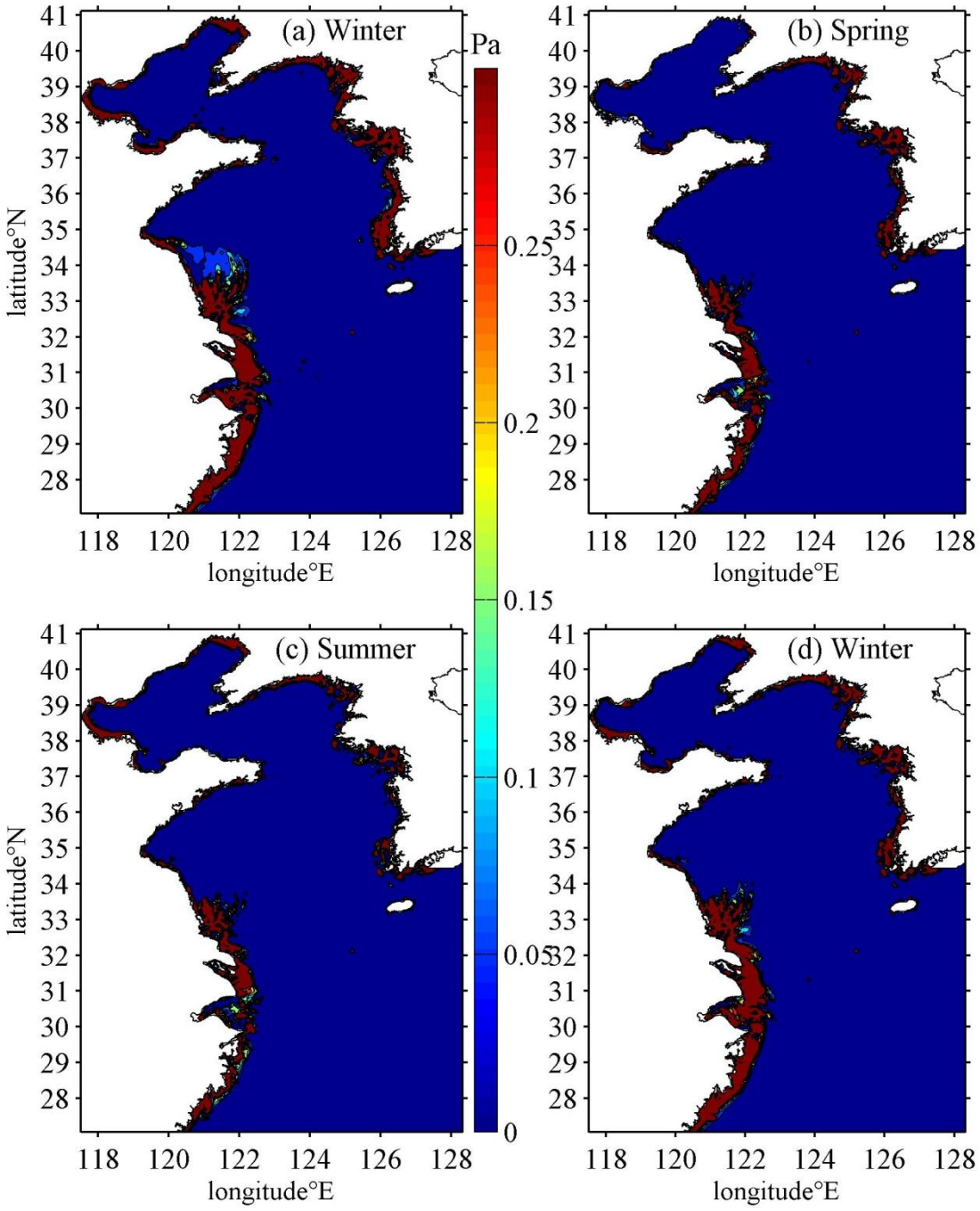

Fig. 5.41 Seasonal wave induced bottom shear stress (Pa)

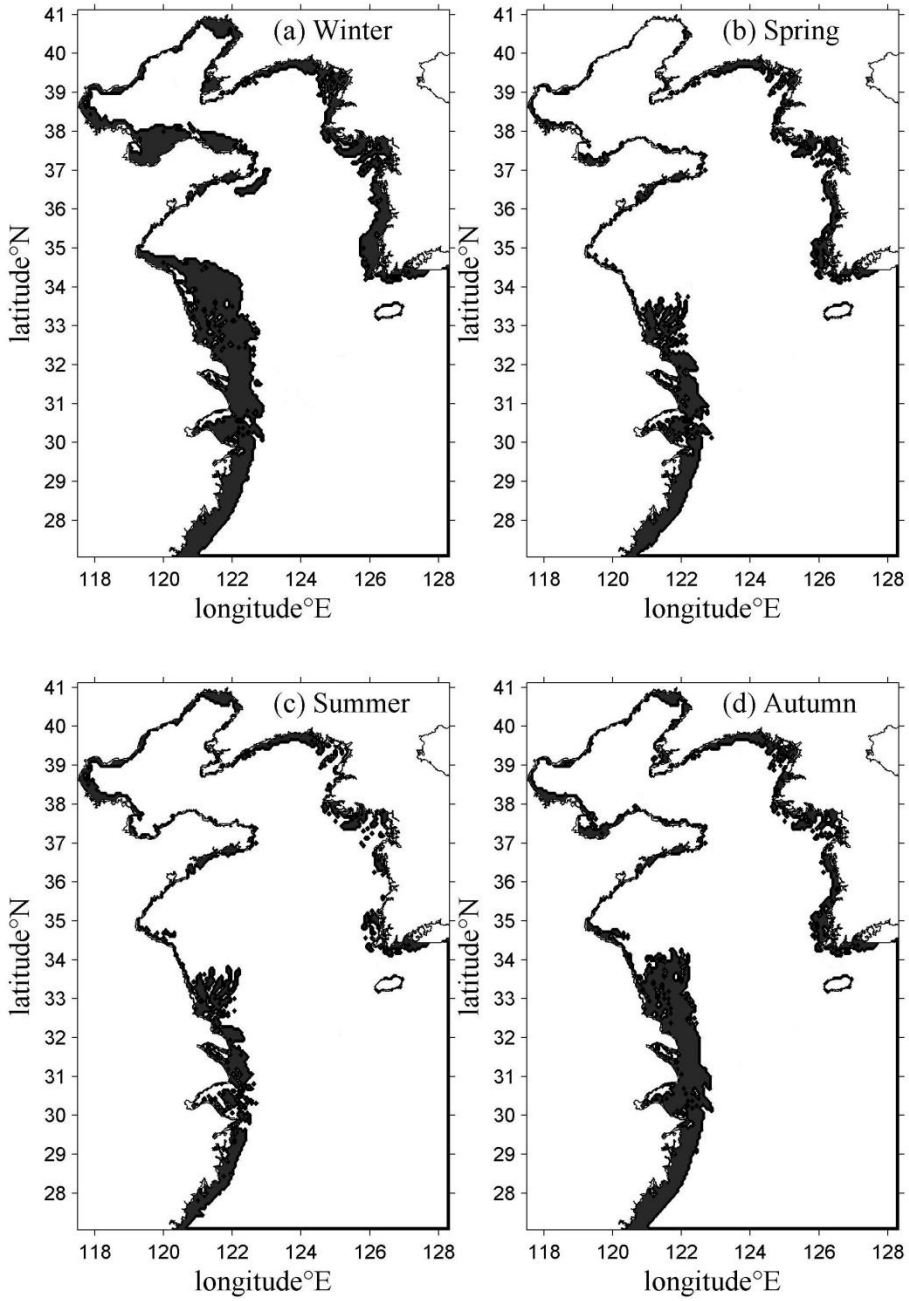

Fig. 5.42 The shaded area where wave induced bottom shear stress is larger than 0.2*maximum tidal induced bottom shear stress

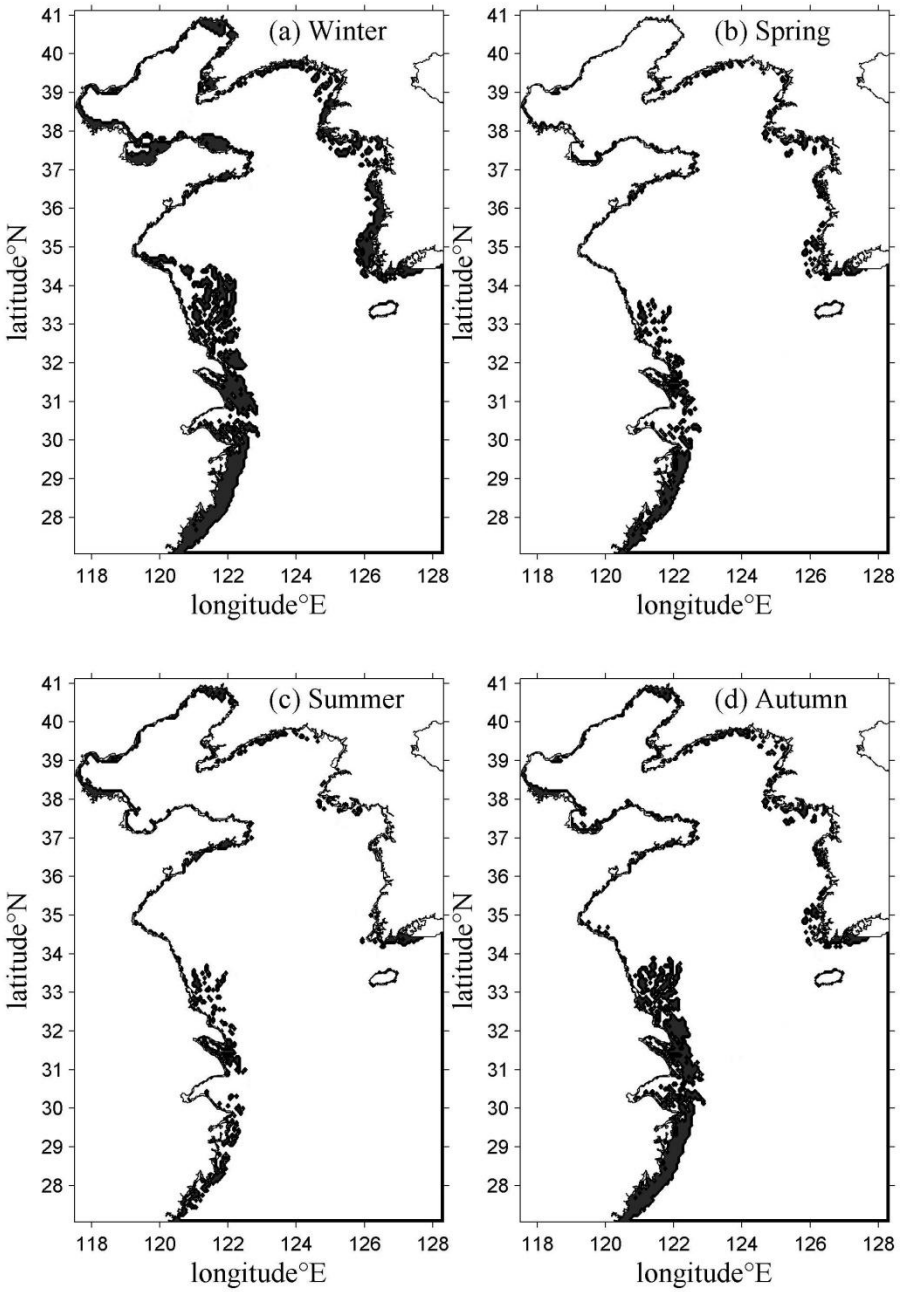

Fig. 5.43 The shaded area where wave induced bottom shear stress is larger than 0.5*maximum tidal induced bottom shear stress

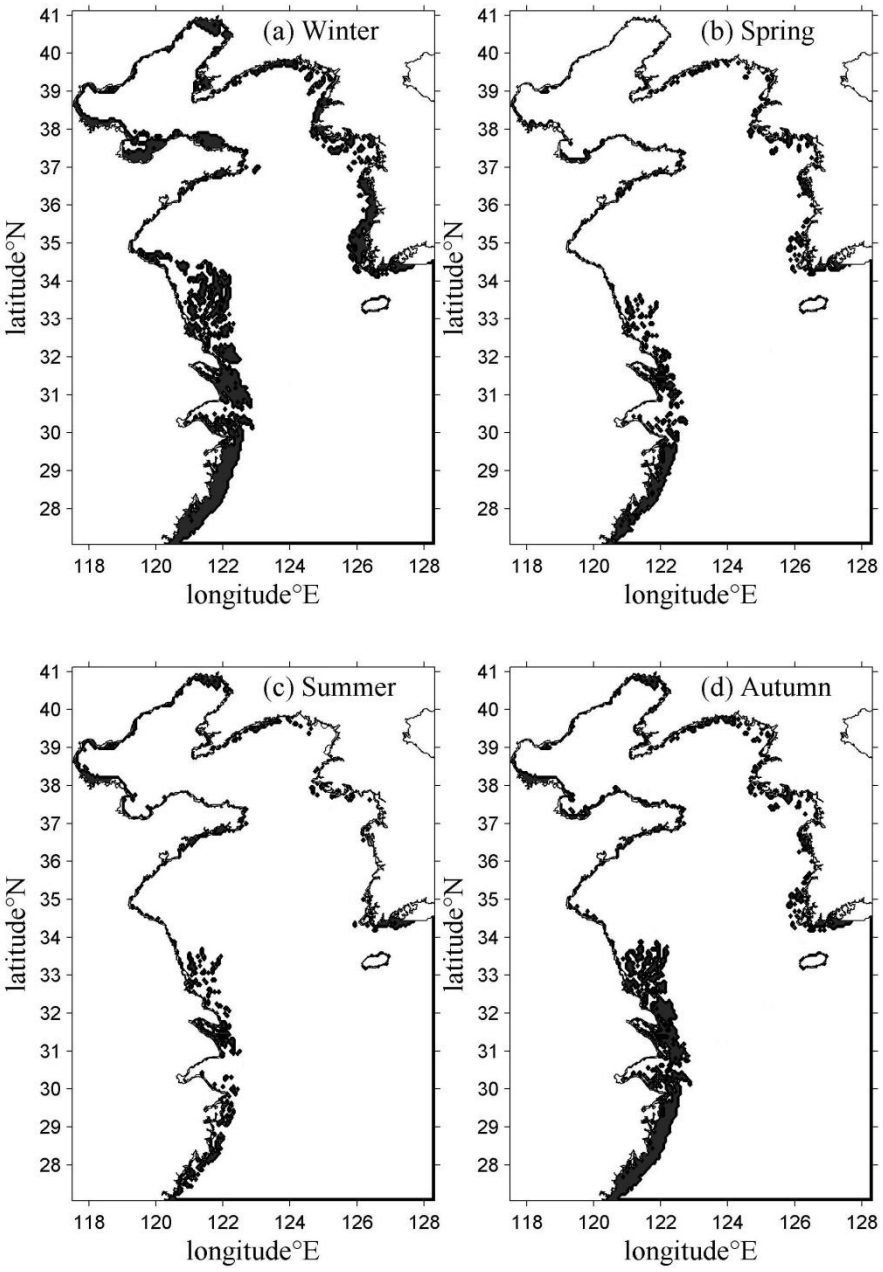

Fig. 5.44 The shaded area where wave induced bottom shear stress is larger than maximum tidal induced bottom shear stress

According the wind history recorded along the coast of China, storm happened most frequently in winter. Beaufort wind scale 6 (10.8-13.8m/s) and over happened every month, but most often in April (7 days a month). The typhoon with Beaufort wind scale 8 (17.2-20.7m/s) occurred once or twice every year in the East China Sea.

Fig. 5.45 showed that the wave effect can reach to the bottom of centre Yellow Sea under several winter storms under strong wind with 16m/s.

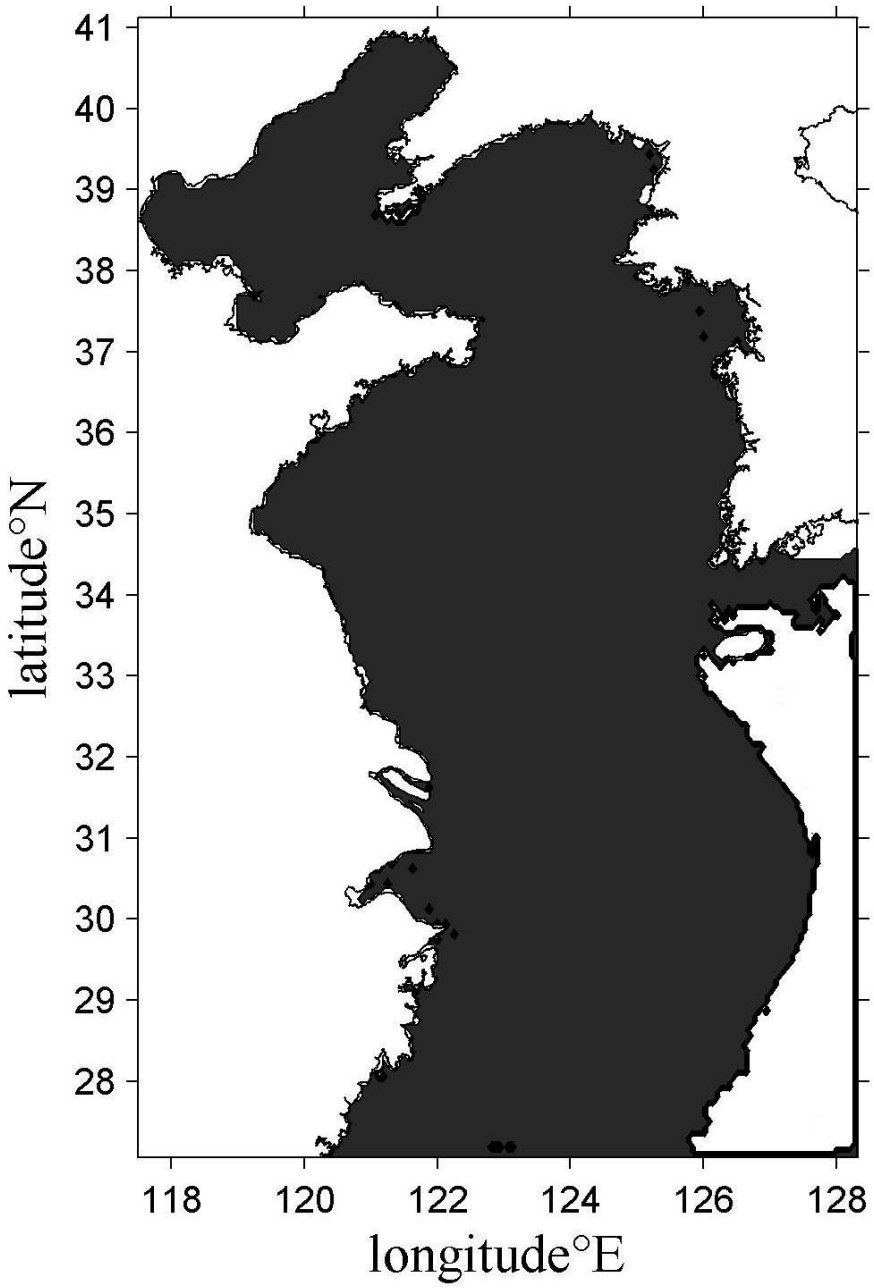

Fig. 5.45 The shaded area where wave induced bottom shear stress is larger than maximum tidal induced bottom shear stress under storm in winter

5.3.3 **Wave parameters under different sea level over the last 12,000 years**

Same with the tidal pattern under different sea level over the last 12, 000 years, the wave fields with sea water level -60,-30,-15 and 5 m are also calculated.

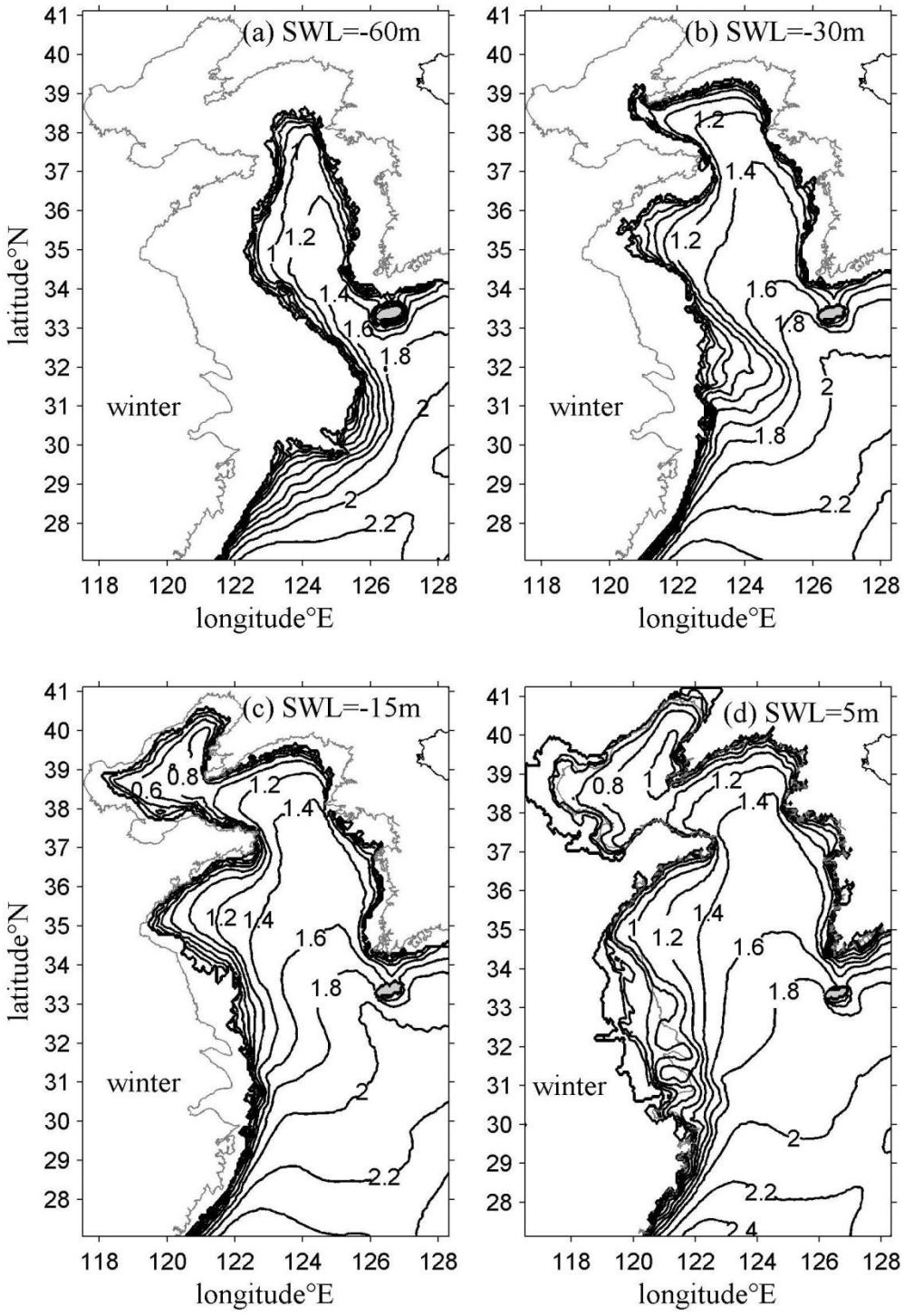

Fig. 5.46 Significant wave height (m) in winter when sea water level (a) -60m (b) -30m (c) -15m (d) 5m

The bathymetries are the same with corresponding tidal model experiments. The wind field is the present climatological monthly mean wind as lack of history wind

data. The significant wave height distributions of four seasons under different sea water level are shown as (Fig. 5.46-Fig. 5.49).

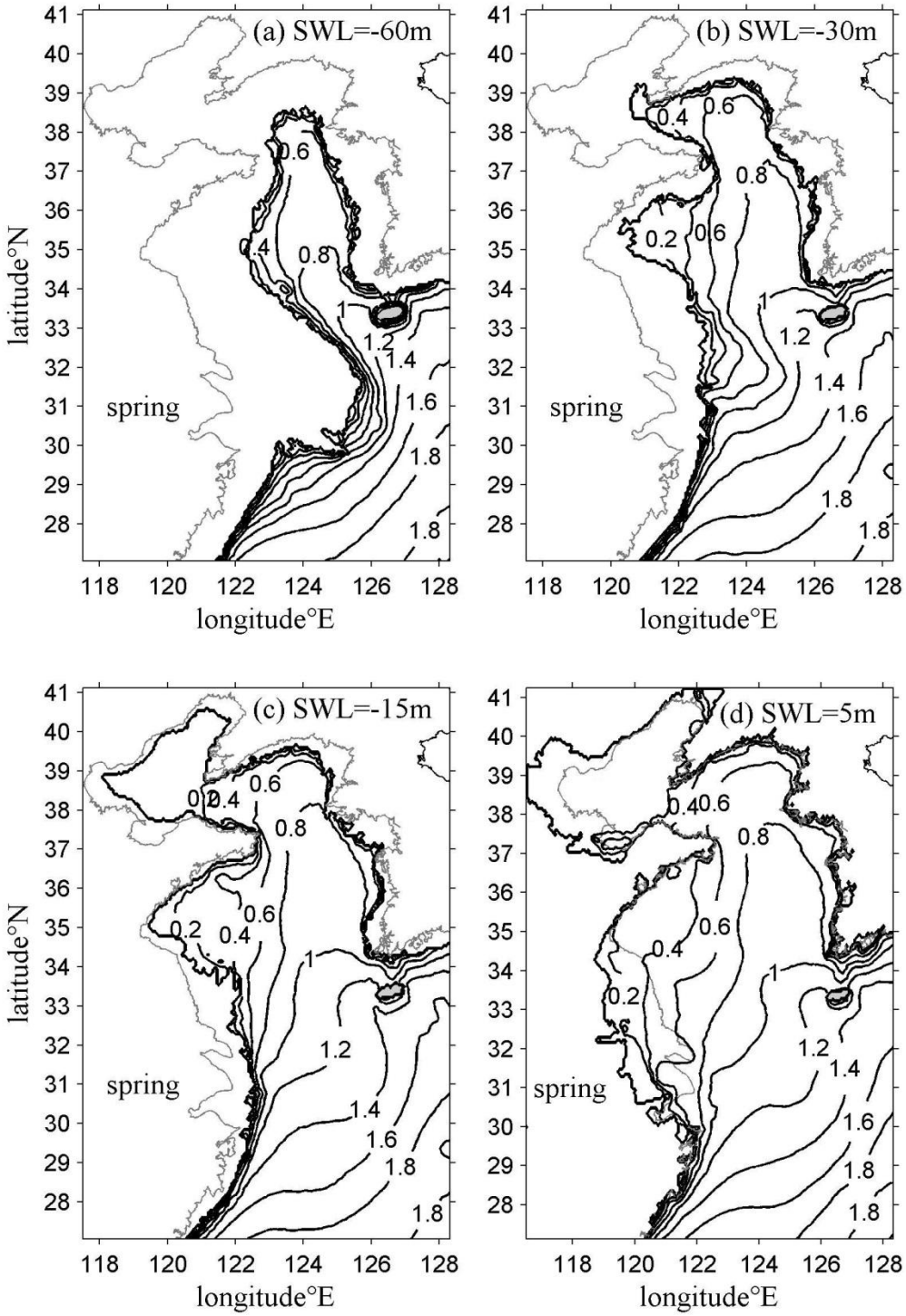

Fig. 5.47 Significant wave height (m) in spring when sea water level (a) -60m (b) -30m (c) -15m (d) 5m

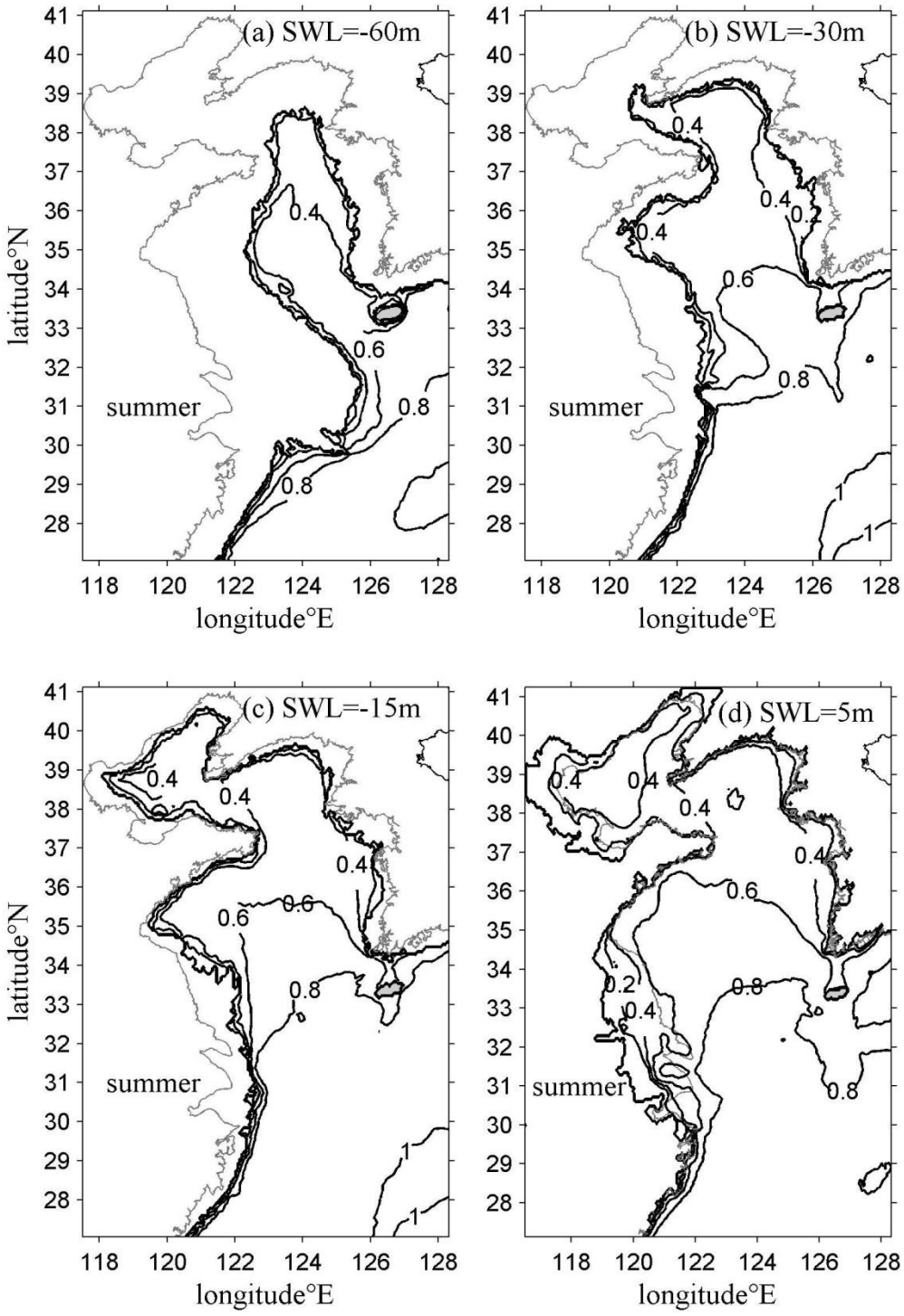

Fig. 5.48 Significant wave height (m) in summer when sea water level (a) -60m (b) -30m (c) -15m (d) 5m

Generally speaking, the wave height increased as the sea water level rise from the -60m to 5m in the same season. The height distribution pattern is similar with present state. The mean wave is largest in the winter and smallest in the summer.

However, although both waves and tidal current (section 5.1.3) were weaker when the sea level was low, the shoreline and shallow region at that time were closer to the Central Yellow Sea Mud (CYSM) area and the Huanghe River derived sediments and the resuspended sediments only need to travel a much shorter distance to reach CYSM. Therefore the deposition rate in the CYSM area is not necessary smaller at lower sea water level in spite of weaker dynamic conditions, as evidenced by the nearly constant deposition rate determined from the core analysis.

.

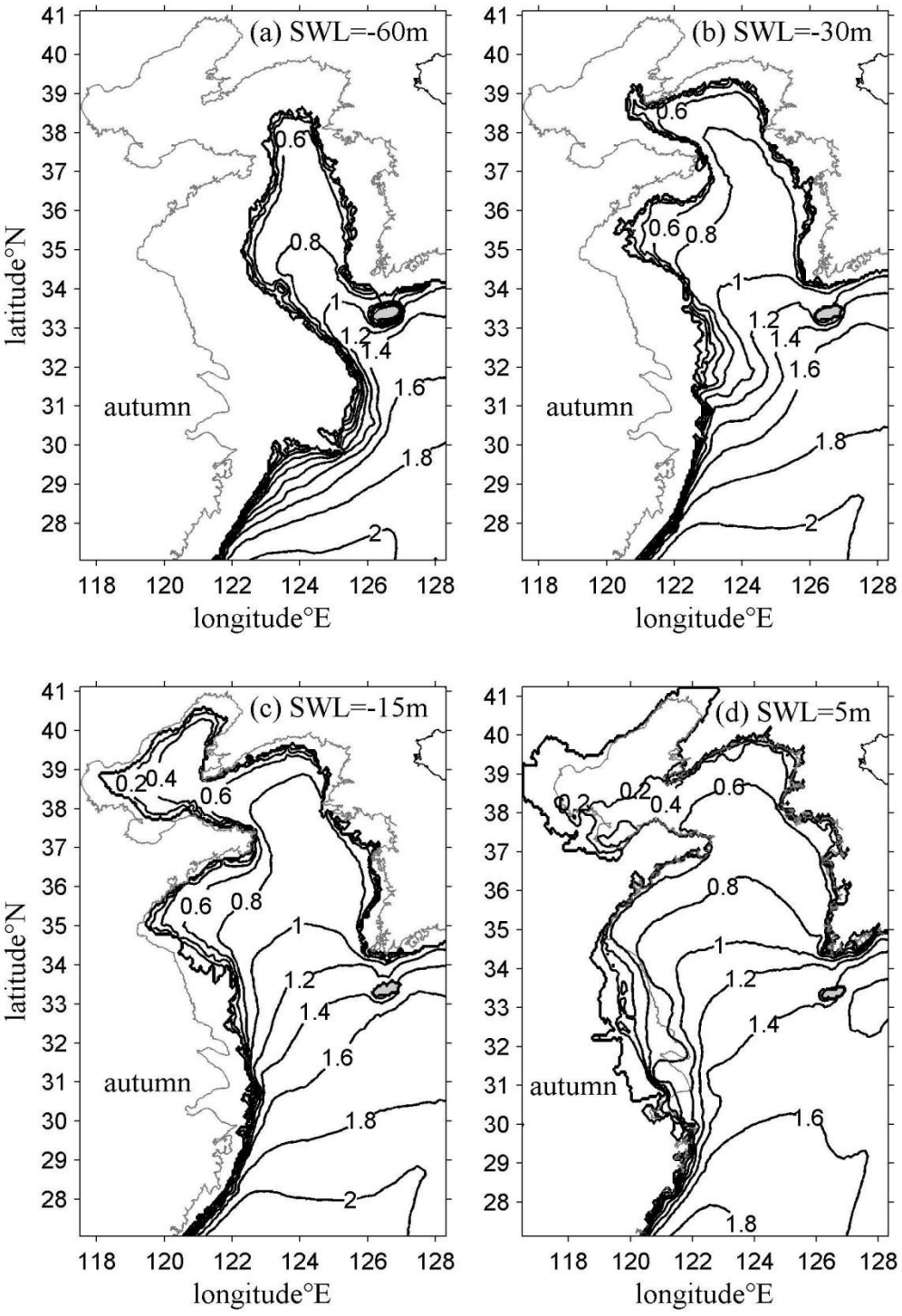

Fig. 5.49 Significant wave height (m) in autumn when sea water level (a) -60m (b) -30m (c) -15m (d) 5m

5.4 **Yellow Sea Cold Water Mass**

The circulation of YSCWM is studied by considering a cross-sectional area of 35°N latitude with 700 km lateral extent, orientated in a west-east direction. The resolution is 900m in the horizontal and 2m in the vertical. The Coriolis parameter f is set to be 1.0×10^{-4} corresponding to an approximate Yellow Sea latitude 35°N. In all calculations, the same idealised initial temperature distribution corresponding to a typical measured Yellow Sea cold water dome was applied for simplicity (Fig. 5.50).

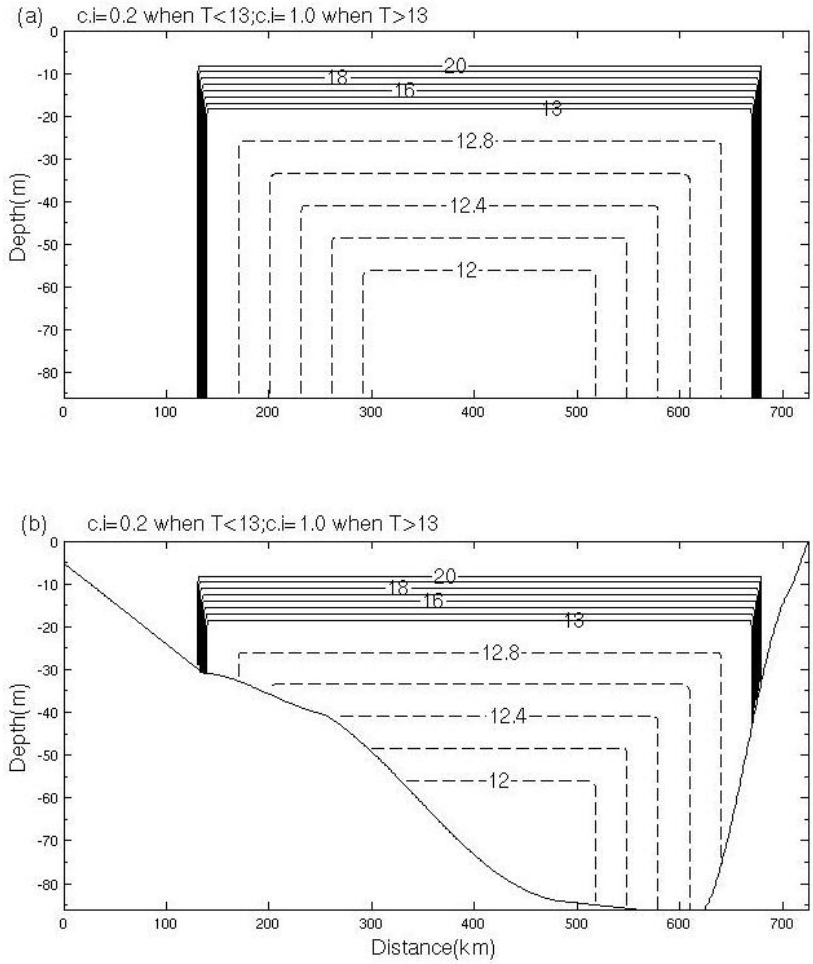

Fig. 5.50 Initial temperature field (T℃) contour interval c.i. (a) a flat bottom (b) real topography across 35 ℃N latitude

The temperature varies about 7°C within 15 km in the frontal area and within 15m in the vertical thermocline area. In all calculations, motion is induced by specifying an initial temperature distribution characteristic of the Yellow Sea cold water domes. In

order to investigate the influence of topography, a constant water depth (86m) was assumed as a comparison with real water depth across 35°N latitude. All the models start from rest.

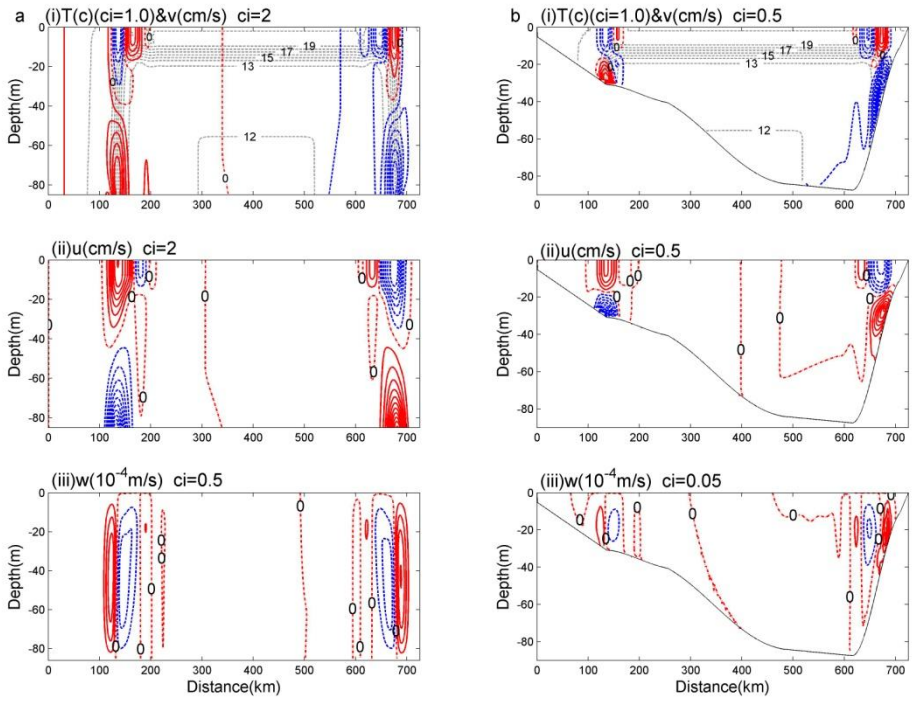

Fig. 5.51 a (i) Contours of temperature field (T℃) contour interval c.i (c.i.=1.0 ℃), along frontal velocity v (cm/s) (c.i.=4 cm/s), (ii) across frontal velocity u(cm/s) (c.i. = 4.0 cm/s), (iii) vertical velocity(10^{-4}m/s) ; b same as Fig. a only with real topography.(Note: solid red contour is positive value, dashed blue contour is negative, and dashed red is zero value)

Fig. 5.51a(i) show that the density field produces double cyclones in the surface layer: inner is a small anti-cyclonic (clockwise) (8-10cm/s) while outer is a stronger cyclonic (anti-clockwise) (15-20cm/s) circulation. Below the thermocline, there is an anti-cyclonic (clockwise) circulation, which is quite consistent with the pattern observed by Pang *et al.* (2004) based on 23 drifters data.

Fig. 5.51b shows similar circulation pattern but with smaller eddy velocity (5-8cm/s). The net circulation of the upper layer YSCWM is anticlockwise (cyclonic), which is mainly a quasi-geostrophic flow along tidal-induced temperature front. The

maximum velocity appears in the frontal area, and the current is very weak in the centre YSCWM. In the upper layer the water converges into the centre in total while in the bottom layer (below 20 m) the water diverges from the centre area (Fig. 5.51b (ii)). The vertical velocity near the centre of cold dome is positive, which means upwelling but the velocity scale is 10^{-7} m/s. The YSCWM circulation may provide an explanation to the phenomenon that suspended sediment are trapped and deposited near the front between YSCWM and the coastal water in the Subei coast.

The model result of cold water dome circulation is different from previous model studies in which simplified equations are used.

For example, the simplified equation in Li and Yuan (1992) is not suitable for the cold water dome margin (frontal area) where the temperature gradient in the *r'* coordinate under Polar coordinates is too large to be ignored. In detail, Equation (5.1) is the thermal equation, and then changed into Equation (5.3) according to Equation (5.2).

$$\frac{\partial T}{\partial t}+\frac{gaA_v}{f^2}\left\{\frac{\partial}{\partial z}\left(\frac{\partial T}{\partial r}\right)\frac{\partial T}{\partial r}+\frac{1}{r}\frac{\partial}{\partial r}\left(r\frac{\partial T}{\partial r}\Big|_z^0\right)\frac{\partial T}{\partial z}\right\}=\frac{\partial}{\partial z}\left(K_v\frac{\partial T}{\partial z}\right) \tag{5.1}$$

$$r'=r;z'=z/-H(r) \tag{5.2}$$

$$\begin{aligned}&\frac{\partial T}{\partial t}+\frac{gaA_v}{f^2}\left\{\left(\frac{\partial T}{\partial r'}-\frac{H'(r')}{H(r')}z'\frac{\partial T}{\partial z'}\right)\left(-\frac{1}{H(r')}\right)\frac{\partial}{\partial z'}\left(\frac{\partial T}{\partial r'}-\frac{H'(r')}{H(r')}z'\frac{\partial T}{\partial z'}\right)+\right.\\&\left.\frac{1}{r'}\left(\frac{\partial}{\partial r'}-\frac{H'(r')}{H(r')}z'\frac{\partial}{\partial z'}\right)\left[r'\left(\frac{\partial T}{\partial r'}-\frac{H'(r')}{H(r')}z'\frac{\partial T}{\partial z'}\right)\Big|_{z'}^0\right]\left(-\frac{1}{H(r')}\frac{\partial T}{\partial z'}\right)\right\}=\\&\frac{1}{H^2(r')}\frac{\partial}{\partial z'}\left(K_v\frac{\partial T}{\partial z'}\right)\end{aligned} \tag{5.3}$$

Then get the simplified Equation (5.4) by ignoring $\frac{\partial T}{\partial r\prime}$, which is small enough to be neglected at the centre of YSCWM, however, it is not the case at the thermal front where the temperature gradient is very large.

$$\frac{gaA_v}{f^2}\left\{\left(-\frac{H'(r')}{H(r')}z'\frac{\partial T}{\partial z\prime}\right)\left(-\frac{1}{H(r\prime)}\right)\frac{\partial}{\partial z\prime}\left(-\frac{H'(r')}{H(r')}z'\frac{\partial T}{\partial z\prime}\right)+\right.$$
$$\left.\frac{1}{r\prime}\left(\frac{\partial}{\partial r\prime}-\frac{H'(r')}{H(r')}z'\frac{\partial}{\partial z\prime}\right)\left[r'\frac{H'(r')}{H(r')}z'\frac{\partial T}{\partial z\prime}\right].\left(-\frac{1}{H(r')}\frac{\partial T}{\partial z\prime}\right)\right\}=\frac{1}{H^2(r\prime)}\frac{\partial}{\partial z\prime}\left(K_v\frac{\partial T}{\partial z\prime}\right) \quad (5.4)$$

Feng *et al.* (1992) used the equation for the study of thermocline in the open ocean to investigate the YSCWM circulation. In detail, Equation (5.5)-(5.10) are the basic equations,

$$-fv=\frac{1}{\rho_0}\frac{\partial p}{\partial x}+K_H\frac{\partial^2 u}{\partial x^2}+K_v\frac{\partial^2 u}{\partial z^2} \quad (5.5)$$

$$fu=K_H\frac{\partial^2 v}{\partial x^2}+K_v\frac{\partial^2 v}{\partial z^2} \quad (5.6)$$

$$\frac{\partial u}{\partial x}+\frac{\partial w}{\partial z}=0 \quad (5.7)$$

$$\frac{\partial p}{\partial z}=-\rho g \quad (5.8)$$

$$w\frac{\partial \rho_B}{\partial z}=K_{TH}\frac{\partial^2 \rho}{\partial x^2}+K_{Tv}\frac{\partial^2 \rho}{\partial z^2} \quad (5.9)$$

$$\rho=\rho_0(1-\alpha T) \quad (5.10)$$

Where ρ_B is the background density. K_{TH} and K_{Tv} are the horizontal and vertical heat turbulent coefficients.

And then apply the non-dimensional method and omitting the background pressure and temperature fields and yield the Equation (5.11)-(5.15) .

$$v = \frac{\partial p}{\partial x} - E\nabla^2 u \tag{5.11}$$

$$u = E\nabla^2 v \tag{5.12}$$

$$\frac{\partial u}{\partial x} + \frac{\partial w}{\partial z} = 0 \tag{5.13}$$

$$p_z = T \tag{5.14}$$

$$M^2 \sigma w = E\nabla^2 T \tag{5.15}$$

Where $\nabla^2 = \frac{\partial^2}{\partial x^2} + \frac{\partial^2}{\partial z^2}$, $\sigma = K_v / K_{Tv}$; E is the Ekman number, M is the non-dimensional buoyancy frequency.

The background density gradient is usually small enough to be neglected in the open ocean. However, that is not the case in the Yellow Sea Cold Water Mass, where the density induced horizontal advection is in the same scale as the vertical advection term in the density equation. Omitting the background pressure and temperature fields is not a proper way.

In addition, it's common to see that "upwelling exists at the central part of a cyclonic eddy", in the open sea and meteorology. In the shallow sea, however, it is not true anymore, simply because a horizontal isobaric surface does not exist as in the deep sea. Thus, the explanation of the genesis of Southern Yellow Sea centre mud patch related to the cyclonic eddy (Hu, 1984; Pang and Hu, 2002; Shi *et al.*, 2002) is not reliable.

5.5 **Sediment transport**

As the Huanghe River is the most important sediment source for the central south Yellow Sea Mud deposit, how much Huanghe River derived sediment can be transported to the South Yellow Sea is studied here.

The initial sediment thickness is set to zero. Following Lu *et al*.(2013), the source information of the Huanghe River used for the simulation is listed in Table 5.6, including the monthly variation of the runoff, sediment discharge and SSC. The runoff and suspended sediment have highest values in August and second highest values in September, while lowest in January and February. The sediment discharge in August is 49 times larger than that in January or February.

Table 5.6 Climatological monthly runoff (m^3/s), discharged SSC (in kg/m^3), and sediment discharge (kg/s) of the Huanghe River(Lu *et al.*, 2013)

	Jan	Feb	Mar	Apr	May	Jun	Jul	Aug	Sep	Oct	Nov	Dec
Runoff	454.7	368.8	603.0	579.6	564.0	517.1	1,430.7	2,242.8	2,086.6	1,875.8	1,134.0	649.9
Discharged SSC	4.42	5.45	9.08	12.10	11.75	15.05	34.22	44.31	35.64	22.41	14.33	7.83
Sediment discharge	2,012	2,012	5,475	7,014	6,629	7,784	48,959	99,369	74,357	42,032	16,250	5,090

The main parameter values used in the sediment transport model are as follows: The settling speed, Ws, is set to10^{-6}m/s. The critical shear stress of deposition is taken to be 0.15 N/m^2, the erosion rate is 0.5×10^{-6} kg $m^{-1}s^{-1}$(Lu *et al.*, 2013), Partheniades' formula is used to compute probability of deposition. The density of sediment is 1.36×10^3 kg/m^3. The bottom fiction and roughness coefficients are 0.0025 and 0.001, respectively. The hydrodynamic model is run for 6 model years from the initial state to spin-up. Thereafter, the coupled hydrodynamic-sediment transport model is run for another 8 years for the sediment transports to reach steady state.

The Bohai Strait section and the 37 ℃N section are selected to analyse fluxes of the Yellow River derived sediment, which represent the sediment transport from the BS to the North YS, from the North YS to the South YS, respectively. The flow vectors

normal to each of the cross sections multiplied by the SSC and the vertical layer thickness at the corresponding layer are used to compute the Suspended Sediment Flux (SSF). For convenience, the eastward velocity is defined as positive for Bohai Strait section and southward velocity is defined as positive for 37 °N section.

Across the Bohai Strait section, the eastward component of the velocity is multiplied by SSC, while across the 37 ° N section, SSF is computed using the southward component of the velocity.

Annual mean values of SSF across the Bohai Strait and the 37 ° N section are shown in Table 5.7.

Table 5.7 The model predicted annual mean SSF (kg/s) and their percentage of the total river discharge (%) at two sections

	Cross-section Bohai strait	Cross-section 37 °N	units
Annual mean fluxes	4280	1840	kg/s
% of the total discharge	16.2%	6.97%	%

The model results revealed roughly that 16% of the Huanghe River discharged sediment is transported out of Bohai Strait and nearly 7% will finally transported to the South Yellow Sea, which falls between the ranges of budget listed in Table 3.3 and close to the median.

Chapter 6 Conclusions and recommendations for future work

6.1 Conclusions

In this research a combined geological (mainly based on the core analysis) and hydrodynamic modeling (currents and waves) study is carried out in order to determine the key factors affecting the formation of mud deposits in the central Southern Yellow Sea. It has focused in particular on identifying the key processes to the formation of the deposits by considering separately the hydrodynamic forcing factors such as waves, currents and winds and the linkages between sediment supply, accumulation, and dynamics related to the formation of the deposits.

It is found that the fine sediments discharged from Huanghe River, the resuspended sediments of Old Huanghe Delta and Changjiang River derived sediment are the main sources for the mud deposit at the Southern Yellow Sea, a conclusion that appears to be supported by all sedimentological, mineralogical, and geochemical and hydrodynamic modelling evidence. Based on high-resolution Chirp sonar profiles combined with analysis of the available cores samples the average deposition rate at the Central Yellow Sea mud patch from the three sources is calculated to be about 3.6 $\times 10^{7}$ t a^{-1}.

As to the sediment movement processes, the tidal current is identified as the main agent for transporting the fine sediment to the mud patch in the central South Yellow Sea. According to the numerical model results the tidal currents are weakest in the central area of the Southern Yellow Sea and change into anti-clockwise northwards, while they are much stronger along the Shandong peninsula and Subei Coast. This current system is not only effective in carrying the sediments delivered to the sea from the Huanghe River but also capable of inducing resuspension of sediments of from

Old Huanghe Delta area and depositing them in the area with the weak tidal area in the southern Yellow Sea.

However tidal action alone is found to be insufficient to account for the volume of the deposit. Wind waves play an important role in generating and maintaining high concentration of suspended sediments, particularly at the Old Huanghe Delta. This sediment resuspension process at the Old Huanghe Delta is most active in winter storms and the current circulation, mainly caused by Asian Monsoon, can transport a large quantity of fine sediments from this area to the central SYS.

The existence of Yellow Sea Cold Water Mass circulation in summer, caused by density difference at Southern YS, is shown to produce counter-rotating cyclonic horizontal eddies in the surface layer: the inner one is anti-cyclonic (clockwise) and relatively weaker (8-10cm/s) while the outer one is a cyclonic (anti-clockwise) and much stronger (15-20cm/s). Below the thermocline, there is an anti-cyclonic (clockwise) circulation. This complex current eddy system has the effect of trapping suspended sediments and depositing them near the front between YSCWM and the coastal water in the Subei coast.

Under present hydrodynamic condition, the modelling results showed that approximately 16% (1.33×10^{8}t a^{-1}) of the Huanghe River-derived sediment is transported out of Bohai Strait of which around 44% (5.72×10^{7}t a^{-1}) will finally be transported to the South Yellow Sea, a volume which is fairly close to the sediment budget estimated by Alexander et al. (1991) based on ^{210}Pb sediment accumulation rate data which suggests that 9-15% of the annual Huanghe discharge is accumulating in the Yellow Sea.

Over the past 12k years the tidal current fields and wave distributions in the Yellow Sea have changed significantly due to the rise in sea-level rise. The number of amphidromic points of M2 and S2 increased from 2 to 4 while that of K1 and O1 increased from 1 to 2 as the sea level rose from -60m, -30m to -15m below the present sea level. The amplitudes of M2 and S2 in the Yellow Sea and Bohai Sea have become larger with co-phase lines showing anti-clockwise rotation as sea-level increased from -60m to it is now. The wave heights have also increased because the increase in water depth as the result of rising sea level. However, although both tidal current and waves were weaker when the sea level was low, the shoreline and shallow region at that time were closer to the Central Yellow Sea Mud (CYSM) area and the Huanghe River derived sediments and the resuspended sediments only need to travel a shorter distance to reach CYSM. Therefore the deposition rate in the CYSM area is not significantly affected by the water level changes as evidenced by the nearly constant deposition rate determined from the core analysis.

6.2 **Recommendations for future research**

Although the present study has extended current knowledge on the large-scale hydrodynamic processes and their relationships with the mud deposits, there remain a number of areas that require further research.

Among the most important is to quantify how much sediments of the Central Yellow Sea mud patch is from the Old Huanghe Delta. Although the present research has demonstrated that the Old Huanghe Delta is the second most important source of sediment for the CYSM, the actual amount is uncertain due to the difficulties in modeling the sediment transport processes over the long term and the lack of field measurements data, especially during winter storm.

Another research task that is worth pursuing is to refine further the grid spacing. The grid space used in the present model is around 5 km in the horizontal, which is reasonable for resolving the regional-scale processes but clearly insufficient to capture the detail dynamic process of the Cold Water Mass. To carry out such work using the 3D hydrodynamic model would require computational power far beyond that available for the present study.

For simplicity, a single storm with prescribed intensity and direction has been considered in the present research instead of using actual wave climate distribution. This will lead to inaccuracies in estimating wave induced shear stresses and amount of sediments transported.

Particle tracking method is to study where the particles discharged from rivers go, very helpful to investigate the source and path of the sediments, which is worth to be carried out in the future.

The effects of different physical processes to the CYSM need further study especially directly with sediment module.

Finally considering numerical models are imperfect abstractions of reality, and precise input data are rarely if ever available, for example, bed sediment size variation, fall velocity for mud flocs or wave climate, therefore, model outputs are inevitably subject to uncertainty. A more comprehensive numerical study is called for to quantify this uncertainly.

Reference

Ahmad, S. M., Anil Babu, G., Padmakumari, V. M., Dayal, A. M., Sukhija, B. S. & Nagabhushanam, P. 2005. Sr, Nd isotopic evidence of terrigenous flux variations in the Bay of Bengal: Implications of monsoons during the last ~34,000 years. *Geophysical Research Letters.*

Alexander, C. R., Demaster, D. J. & Nittrouer, C. A. 1991. Sediment accumulation in a modern epicontinental-shelf setting: The Yellow Sea. *Marine Geology,* 98 (1),51-72.

Allègre, C. J., Dupre, B., Négrel, P. & Gaillardet, J. 1996. Sr-Nd-Pb isotope systematics in Amazon and Congo River systems: Constraints about erosion processes. *Chemical Geology,* 131 (1-4),93-112.

Alpers, W., He, M. X., Zeng, K., Quo, L. F. & Li, X. M. Year. The distribution of internal waves in the East China Sea and the Yellow Sea studied by multi-sensor satellite images. *In:* IEEE International Geoscience and Remote Sensing Symposium, 2005 Seoul. 4784-4787.

Amos, C. L., Grant, J., Daborn, G. R. & Black, K. 1992. Sea Carousel—A benthic, annular flume. *Estuarine, Coastal and Shelf Science,* 34 (6),557-577.

Arakawa, A. & Lamb, V. R. 1977. Computational Design of the Basic Dynamical Processes of the UCLA General Circulation Model. *In:* JULIUS, C. (ed.) *Methods in Computational Physics: Advances in Research and Applications.* Elsevier.173-265.

Asahara, Y., Tanaka, T., Kamioka, H. & Nishimura, A. 1995. Asian continental nature of87Sr/86Sr ratios in north central Pacific sediments. *Earth and Planetary Science Letters,* 133 (1-2),105-116.

Bao, X., Gao, G. & Yan, J. 2001. Three dimensional simulation of tide and tidal current characteristics in the East China Sea. *Oceanologica Acta,* 24 (2),135-149.

Barnhardt, W. A., Belknap, D. F. & Kelley, J. T. 1997. Stratigraphic evolution of the inner continental shelf in response to late Quaternary relative sea-level change, northwestern Gulf of Maine. *Geological Society of America Bulletin,* 109 (5),612-630.

Battjes, J. A. & Janssen, P. a. E. M. Year. Energy Loss and Set-Up Due to Breaking of Random Waves. *In:* Proc. 16th Int. Conf. Coastal Engineering, ASCE,, 1978. 569-587.

Beardsley, R. C., Limeburner, R., Kim, K. & Candela, J. 1992. Lagrangian flow observations in the East China, Yellow and Japan Seas. *La Mer,* 30 (3),297-314.

Belderson, R. H. 1964. Holocene sedimentation in the western half of the Irish Sea. *Marine Geology,* 2 (1-2),147-163.

Bi, N., Yang, Z., Wang, H., Fan, D., Sun, X. & Lei, K. 2011. Seasonal variation of suspended-sediment transport through the southern Bohai Strait. *Estuarine, Coastal and Shelf Science,* 93 (3),239-247.

Boyer, T., Levitus, S., Garcia, H., Locarnini, R. A., Stephens, C. & Antonov, J. 2005. Objective analyses of annual, seasonal, and monthly temperature and salinity for the World Ocean on a 0.25 ° grid. *International Journal of Climatology,* 25 (7),931-945.

Burban, P.-Y., Xu, Y.-J., Mcneil, J. & Lick, W. 1990. Settling speeds of floes in fresh water and seawater. *Journal of Geophysical Research: Oceans,* 95 (C10),18213-18220.

Cavaleri, L. & Rizzoli, P. M. 1981. Wind wave prediction in shallow water: Theory and applications. *Journal of Geophysical Research: Oceans,* 86 (C11),10961-10973.

Chamley, H. 1997. Clay Mineral Sedimentation in the Ocean. *Soils and Sediments.* Springer Berlin Heidelberg.269-302.

Chen, D. 1992. *Marine Atlas Of Bohai Sea .Yellow Sea and East China Sea(Volume 4. HYDROLOGY),* Beijing, China Ocean Press.

Chen, H., X., Hua, F. & Yuan. L.Y. 2006. Seasonal Characteristics and Temporal Variations of Ocean Wave in the Chinese Offshore Waters and Adjacent Sea Areas. *Advances in Marine Science,* 24 (4),407-415.

Chen, Z., Li, J., Shen, H. & Zhanghua, W. 2001. Yangtze River of China: historical analysis of discharge variability and sediment flux. *Geomorphology,* 41 (2–3),77-91.

Chen, Z., Shi, X., Wang, X., Xin, C., Kong, F. & Yi, H. 2003. Geochemical changes in Core B10 in the southern Huanghai Sea and implications for variations in paleoenvironment and paleoclimate. *Acta Oceanologica Sinica,* 25 (1),69-77.

Cheng, Y. & Andersen, O. B. 2010. Improvement in global ocean tide model in shallow water regions. *OSTST.* Lisbon.

Cho, Y.-G., Lee, C.-B. & Choi, M.-S. 1999. Geochemistry of surface sediments off the southern and western coasts of Korea. *Marine Geology,* 159 (1–4),111-129.

Choi, B. H., Eum, H. M. & Woo, S. B. 2003. Modeling of coupled tide-wave-surge process in the Yellow Sea. *Ocean Engineering,* 30 (6),739-759.

Choi, B. H. & Lie, H. J. 1992. Physical oceanography program of the East China Sea and the East Sea (Japan Sea) dynamics in Korea. *Proceeding of PORSEC-92.* Okinawa.

Chough, S. K., Kim, J. W., Lee, S. H., Shinn, Y. J., Jin, J. H., Suh, M. C. & Lee, J. S. 2002. High-resolution acoustic characteristics of epicontinental sea deposits, central–eastern Yellow Sea. *Marine Geology,* 188 (3–4),317-331.

Chough, S. K., Lee, H. J., Chun, S. S. & Shinn, Y. J. 2004. Depositional processes of late Quaternary sediments in the Yellow Sea: A review. *Geosciences Journal,* 8 (2),211-264.

Collins, J. I. 1972. Prediction of shallow-water spectra. *Journal of Geophysical Research,* 77 (15),2693-2707.

Curran, K. J., Hill, P. S., Milligan, T. G., Mikkelsen, O. A., Law, B. A., Durrieu De Madron, X. & Bourrin, F. 2007. Settling velocity, effective density, and mass composition of suspended sediment in a coastal bottom boundary layer, Gulf of Lions, France. *Continental Shelf Research,* 27 (10-11),1408-1421.

De Haas, H., Boer, W. & Van Weering, T. C. E. 1997. Recent sedimentation and organic carbon burial in a shelf sea: The North Sea. *Marine Geology,* 144 (1-3),131-146.

Derry, L. A. & France-Lanord, C. 1996. Neogene Himalayan weathering history and river 87Sr/86Sr: Impact on the marine Sr record. *Earth and Planetary Science Letters,* 142 (1-2),59-74.

Dong, L. X., Guan, W. B., Chen, Q., Li, X. H., Liu, X. H. & Zeng, X. M. 2011. Sediment transport in the Yellow Sea and East China Sea. *Estuarine, Coastal and Shelf Science,* 93 (3),248-258.

Dou, G. R. 1999. Incipient motion of coarse and fine sediment. *Journal of Sediment Research,* 6,1-9.

Eldeberky, Y. & Battjes, J. A. 1996. Spectral modeling of wave breaking: Application to Boussinesq equations. *Journal of Geophysical Research: Oceans,* 101 (C1),1253-1264.

Feng, M., Hu, D. & Li , Y. 1992. A theoretical solution for the thermohaline circulation in the Southern Yellow Sea. *Chinese Journal of Oceanology and Limnology,* 10 (4),289-300.

Fralick, P. & Kronberg, B. 1997. Geochemical discrimination of clastic sedimentary rock sources. *Sedimentary Geology,* 113 (1),111-124.

Gailani, J., Ziegler, C. K. & Lick, W. 1991. The Transport ofSediments in the Fox River. *J. Great Lak es Res.,* 17,479-494.

Geyer, W. R., Signell, R. P., Fong, D. A., Wang, J., Anderson, D. M. & Keafer, B. A. 2004. The freshwater transport and dynamics of the western Maine coastal current. *Continental Shelf Research,* 24 (12),1339-1357.

Graham, A. G. C., Lonergan, L. & Stoker, M. S. 2010. Depositional environments and chronology of Late Weichselian glaciation and deglaciation in the central North Sea. *Boreas,* 39 (3),471-491.

Graham, D. I., James, P. W., Jones, T. E. R., Davies, J. M. & Delo, E. A. 1992. Measurement and Prediction of Surface Shear Stress in Annular Flume. *J Hydr Eng,* 118 (9),1270-1286.

Grant, W. D. & Madsen, O. S. 1979. Combined wave and current interaction with a rough bottom. *J. Geophys. Res.,* 84 (4 C),1797-1808.

GuilléN, J., JiméNez, J., Palanques, A., Gracia, V., Puig, P. & SáNchez-Arcilla, A. 2001. Sediment resuspension across a microtidal, low-energy inner shelf. *Cont. Shelf Res.,* 22 (2).

Guo, X. & Yanagi, T. 1998. Three-dimensional structure of tidal current in the East China Sea and the Yellow Sea. *Journal of Oceanography,* 54 (6),651-668.

Guo, X., Zhang, Y., Zhang, F. & Cao, Q. 2010. Characteristics and flux of settling particulate matter in neritic waters: The southern Yellow Sea and the East China Sea. *Deep-Sea Research Part II: Topical Studies in Oceanography,* 57 (11-12),1058-1063.

Harden, S. L., Demaster, D. J. & Nittrouer, C. A. 1992. Developing sediment geochronologies for high-latitude continental shelf deposits: a radiochemical approach. *Marine Geology,* 103 (1-3),69-97.

Hasselmann, S., Hasselmann, K., Allender, J. H. & Barnett, T. P. 1985. Computations and Parameterizations of the Nonlinear Energy Transfer in a Gravity-Wave Specturm. Part II: Parameterizations of the Nonlinear Energy Transfer for Application in Wave Models. *Journal of Physical Oceanography,* 15 (11),1378-1391.

Hawley, N. 1991. Preliminary Observations of Sediment Erosion from a Bottom Resting Flume. *Journal of Great Lakes Research,* 17 (3),361-367.

Holmedal, L. E. & Myrhaug, D. 2006. Boundary layer flow and net sediment transport beneath asymmetrical waves. *Continental Shelf Research,* 26 (2),252-268.

Holmedal, L. E., Myrhaug, D. & Eidsvik, K. J. 2004. Sediment suspension under sheet flow conditions beneath random waves plus current. *Continental Shelf Research,* 24 (17),2065-2091.

Holthuijsen, L. H. & De Boer, S. 1988. Wave forecasting for moving and stationary targets. *In:* SCHREFLER AND O.C. ZIENKIEWICZ, B., ROTTERDAM (ed.) *Computer modelling in Ocean Engineering.* The Netherlands.231-234.

Hu, B. Q., Yang, Z. S., Zhao, M. X., Saito, Y., Fan, D. J. & Wang, L. B. 2012. Grain size records reveal variability of the East Asian Winter Monsoon since the Middle Holocene in the Central Yellow Sea mud area, China. *Science China Earth Sciences,* 55 (10),1656-1668.

Hu, D. & Wang, Q. 2004. Interannual variability of the southern Yellow Sea Cold Water Mass. *Chinese Journal of Oceanology and Limnology,* 22 (3),231-236.

Hu, D. X. 1984. Upwelling and sedimentation dynamics I. The role of upwelling in sedimentation in the Huanghai Sea and East China Sea. *Chinese Journal of Oceanology and Limnology,* 2 (1),12-19.

Hu, D. X., Cui, M. C., Li, Y. X. & Qu, T. D. 1991. On the Yellow Sea cold water mass-related circulation. *YellowSeaResearch,* 4,79-88.

Hu, L., Shi, X., Guo, Z., Wang, H. & Yang, Z. 2013. Sources, dispersal and preservation of sedimentary organic matter in the Yellow Sea: The importance of depositional hydrodynamic forcing. *Marine Geology,* 335 (0),52-63.

Huang, D., Zhang, T. & Zhou, F. 2010. Sea-surface temperature fronts in the Yellow and East China Seas from TRMM microwave imager data. *Deep Sea Research Part II: Topical Studies in Oceanography,* 57 (11-12),1017-1024.

Isobe, A. 2008. Recent advances in ocean-circulation research on the Yellow Sea and East China Sea shelves. *Journal of Oceanography,* 64 (4),569-584.

Jackson, C. R. & Apel, J. R. 2004. *An atlas of internal solitary-like waves and their properties(second edition),* Global Ocean Associates report.

Janssen, P. a. E. M. 1989. Wave-Induced Stress and the Drag of Air Flow over Sea Waves. *Journal of Physical Oceanography,* 19 (6),745-754.

Janssen, P. a. E. M. 1991. Quasi-linear Theory of Wind-Wave Generation Applied to Wave Forecasting. *Journal of Physical Oceanography,* 21 (11),1631-1642.

Kershaw, P. J., Swift, D. J. & Denoon, D. C. 1988. Evidence of recent sedimentation in the eastern Irish Sea. *Marine Geology,* 85 (1),1-14.

Kim, D., Park, B. & Shin, I. 1998a. Paleoenvironmental changes of the Yellow Sea during the Late Quaternary. *Geo-Marine Letters,* 18 (3),189-194.

Kim, G., Yang, H.-S. & Church, T. M. 1999. Geochemistry of alkaline earth elements (Mg, Ca, Sr, Ba) in the surface sediments of the Yellow Sea. *Chemical Geology,* 153 (1–4),1-10.

Kim, G., Yang, H.-S. & Kodama, Y. 1998b. Distributions of transition elements in the surface sediments of the Yellow Sea. *Continental Shelf Research,* 18 (12),1531-1542.

Kim, J. M. & Kucera, M. 2000. Benthic foraminifer record of environmental changes in the Yellow Sea (Hwanghae) during the last 15,000 years. *Quaternary Science Reviews,* 19 (11),1067-1085.

Kineke, G. C. & Sternberg, R. W. 1995. Distribution of fluid muds on the Amazon continental shelf. *Marine Geology,* 125 (3-4),193-233.

Kineke, G. C., Sternberg, R. W., Trowbridge, J. H. & Geyer, W. R. 1996. Fluid-mud processes on the Amazon continental shelf. *Continental Shelf Research,* 16 (5-6),667-696.

Komen, G. J., Cavaleri, L., Donelan, M., Hasselmann, K., Hasselmann, S. & Janssen, P. a. E. M. 1994. *Dynamics and Modelling of Ocean Waves,* Cambridge University Press.

Komen, G. J. & Hasselmann, K. 1984. On the Existence of a Fully Developed Wind-Sea Spectrum. *Journal of Physical Oceanography,* 14 (8),1271-1285.

Krone, R. B. 1962. Flume Studies ofthe Transport ofSediment in Estuarial Processes. Berkeley: University of California.

Kuhrts, C., Fennel, W. & Seifert, T. 2004. Model studies of transport of sedimentary material in the western Baltic. *Journal of Marine Systems,* 52 (1-4),167-190.

Lan, X. H., Zhang, Z. X., Li, R. H. & Ding, D. 2010. Provenance Study of Sediments in Core NT2 of the South Yellow Sea. *ACTA SEDIMENTOLOGICA SINICA,* 28 (6),1182-1189.

Lee, H. J. & Chough, S. K. 1989. Sediment distribution, dispersal and budget in the Yellow Sea. *Marine Geology,* 87 (2-4),195-205.

Lee, H. J. & Chu, Y. S. 2001. Origin of inner-shelf mud deposit in the southeastern yellow sea: huksan mud belt. *Journal of Sedimentary Research,* 71 (1),144-154.

Lee, H. J., Jung, K. T., So, J. K. & Chung, J. Y. 2002. A three-dimensional mixed finite-difference Galerkin function model for the oceanic circulation in the Yellow Sea and the East China Sea in the presence of M2 tide. *Continental Shelf Research,* 22 (1),67-91.

Lee, J. C. & Jung, K. T. 1999. Application of eddy viscosity closure models for the M2 tide and tidal currents in the Yellow Sea and the East China Sea. *Continental Shelf Research,* 19 (4),445-475.

Lee, S. H. & Beardsley, R. C. 1999. Influence of stratification on residual tidal currents in the Yellow Sea. *Journal of Geophysical Research C: Oceans,* 104 (C7),15679-15701.

Li, C. X., Zhang, J. Q., Fan, D. D. & Deng, B. 2001. Holocene regression and the tidal radial sand ridge system formation in the Jiangsu coastal zone, east China. *Marine Geology,* 173 (1-4),97-120.

Li, H. & Yuan, Y. 1992. On the formation and maintenance mechanisms of the Cold Water Mass of the Yellow Sea. *Chinese Journal of Oceanology and Limnology,* 10 (2),97-106.

Liang, B., Li, H. & Lee, D. 2007. Numerical study of three-dimensional suspended sediment transport in waves and currents. *Ocean Engineering,* 34 (11-12),1569-1583.

Lim, D. I., Choi, J. Y., Jung, H. S., Rho, K. C. & Ahn, K. S. 2007. Recent sediment accumulation and origin of shelf mud deposits in the Yellow and East China Seas. *Progress In Oceanography,* 73 (2),145-159.

Lin, X. & Yang, J. 2011. An asymmetric upwind flow, Yellow Sea Warm Current: 2. Arrested topographic waves in response to the northwesterly wind. *Journal of Geophysical Research,* 116 (C4).

Lin, X., Yang, J., Guo, J., Zhang, Z., Yin, Y., Song, X. & Zhang, X. 2011. An asymmetric upwind flow, Yellow Sea Warm Current: 1. New observations in the western Yellow Sea. *Journal of Geophysical Research,* 116 (C4).

Liu, F., Chen, S., Peng, J. & Chen, G. 2011. Temporal variability of water discharge and sediment load of the Yellow River into the sea during 1950-2008. *Journal of Geographical Sciences,* 21 (6),1047-1061.

Liu, G., Wang, H., Sun, S. & Han, B. 2003. Numerical study on the velocity structure around tidal fronts in the yellow sea. *Advances in Atmospheric Sciences,* 20 (3),453-460.

Liu, J., Li, A. & Chen, M. 2010. Environmental evolution and impact of the Yellow River sediments on deposition in the Bohai Sea during the last deglaciation. *Journal of Asian Earth Sciences,* 38 (1-2),26-33.

Liu, J., Li, A., Chen, M., Xiao, S. & Wan, S. 2008a. Sedimentary changes during the Holocene in the Bohai Sea and its paleoenvironmental implication. *Continental Shelf Research,* 28 (10-11),1333-1339.

Liu, J., Milliman, J. & Gao, S. 2002. The Shandong mud wedge and post-glacial sediment accumulation in the Yellow Sea. *Geo-Marine Letters,* 21 (4),212-218.

Liu, J., Saito, Y., Wang, H., Yang, Z. & Nakashima, R. 2007a. Sedimentary evolution of the Holocene subaqueous clinoform off the Shandong Peninsula in the Yellow Sea. *Marine Geology,* 236 (3-4),165-187.

Liu, J., Saito, Y., Wang, H., Zhou, L. & Yang, Z. 2009. Stratigraphic development during the Late Pleistocene and Holocene offshore of the Yellow River delta, Bohai Sea. *Journal of Asian Earth Sciences,* 36 (4-5),318-331.

Liu, J., Wang, H., Li, S. Q. & Jin, X. M. 2004a. Postglacial transgressive sedimentary records of muddy sedimentary areas in the north of the South Yellow Sea. *Marine Geology & Quaternary Geology,* 24 (3),1-10.

Liu, J. F. & Sun, L. Y. 2000. Characteristic analysis of wind field and sea wave field in the western part of the N. Pacific Ocean. *Marine Forecast,* 17 (3),54-62.

Liu, J. P., Milliman, J. D., Gao, S. & Cheng, P. 2004b. Holocene development of the Yellow River's subaqueous delta, North Yellow Sea. *Marine Geology,* 209 (1–4),45-67.

Liu, J. P., Milliman, J. D., Gao, S. & Cheng, P. 2004c. Holocene development of the Yellow River's subaqueous delta, North Yellow Sea. *Marine Geology,* 209 (1-4),45-67.

Liu, J. P., Xu, K. H., Li, A. C., Milliman, J. D., Velozzi, D. M., Xiao, S. B. & Yang, Z. S. 2007b. Flux and fate of Yangtze River sediment delivered to the East China Sea. *Geomorphology,* 85 (3-4),208-224.

Liu, Z., Hu, D. & Chu, Z. 2008b. Observation of currents in the southern yellow sea in the summers of 2001 and 2003. *Journal of Ocean University of China,* 7 (1),17-26.

Lu, J., Qiao, F., Wang, X., Teng, Y., Jung, K. & Liu, Y. 2013. Modeling the Yellow River sediment flux and its deposition patterns under climatological conditions. *Ocean Dynamics,* 63 (6),709-722.

Lu, J., Qiao, F. L., Wang, X. H., Wang, Y. G., Teng, Y. & Xia, C. S. 2011. A numerical study of transport dynamics and seasonal variability of the Yellow River sediment in the Bohai and Yellow seas. *Estuarine, Coastal and Shelf Science,* 95 (1),39-51.

Macintyre, S., Lick, W. & Han Tsai, C. H. T. 1990. Variability of entrainment of cohesive sediments in freshwater. *Biogeochemistry,* 9 (3),187-209.

Macken, A., Giltrap, M., Foley, B., Mcgovern, E., Mchugh, B. & Davoren, M. 2009. An integrated approach to the toxicity assessment of Irish marine sediments. Application of porewater Toxicity Identification Evaluation (TIE) to Irish marine sediments. *Environment International,* 35 (1),98-106.

Madsen, O. S., Poon, Y.-K. & Graber, H. C. 1988. *SPECTRAL WAVE ATTENUATION BY BOTTOM FRICTION: THEORY*.

Mao, C., Chen, J., Yuan, X., Yang, Z. & Ji, J. 2011. Seasonal variations in the Sr-Nd isotopic compositions of suspended particulate matter in the lower Changjiang River: Provenance and erosion constraints. *Chinese Science Bulletin,* 56 (22),2371-2378.

Marshall, J., Adcroft, A., Hill, C., Perelman, L. & Heisey, C. 1997a. A finite-volume, incompressible navier stokes model for, studies of the ocean on parallel computers. *Journal of Geophysical Research C: Oceans,* 102 (C3),5753-5766.

Marshall, J., Hill, C., Perelman, L. & Adcroft, A. 1997b. Hydrostatic, quasi-hydrostatic, and nonhydrostatic ocean modeling. *Journal of Geophysical Research C: Oceans,* 102 (C3),5733-5752.

Marshall Mccabe, A. 1997. Geological constraints on geophysical models of relative sea-level change during deglaciation of the western Irish Sea Basin. *Journal of the Geological Society,* 154 (4),601-604.

Martin, J. M., Zhang, J., Shi, M. C. & Zhou, Q. 1993. Actual flux of the Huanghe (yellow river) sediment to the Western Pacific ocean. *Netherlands Journal of Sea Research,* 31 (3),243-254.

Mask, A. C., O'brien, J. J. & Preller, R. 1998. Wind-driven effects on the Yellow Sea Warm Current. *Journal of Geophysical Research,* 103 (C13),30713-30729.

Mehta, A. J. & Partheniades, E. 1975. An Investigation Of The Depositional Properties Of Flocculated Fine Sediments. *Journal of Hydraulic Research,* 13 (4),361-381.

Mei, C. C. 1983. *The applied dynamics of ocean surface waves,* New York, Wiley.

Meng, X. W., Du, D. W., Chen, Z. H. & Wang, X. Q. 2000. Factors controlling spatial variation of ~(87)Sr/~(86)Sr in the fine-grained sediments from the overbanks of the Yellow River and Yangtze River and its implication for provenance of marine sediments. *Geochimica,* 29,563-569.

Merino, J., Sanchez-Cabeza, J. A., Pujol, L., Leonard, K. & Mccubbin, D. 2000. Plutonium activity ratios in plankton: New evidence of hold-up time in Irish Sea sediments. *Journal of Radioanalytical and Nuclear Chemistry,* 243 (2),517-524.

Milliman, J. D., Beardsley, R. C., Zuo-Sheng, Y. & Limeburner, R. 1985. Modern Huanghe-derived muds on the outer shelf of the East China Sea: identification and potential transport mechanisms. *Continental Shelf Research,* 4 (1–2),175-188.

Milliman, J. D. & Meade, R. H. 1983. World-wide delivery of sediment to the oceans. *Journal of Geology,* 91 (1),1-21.

Milliman, J. D., Qin, Y.-S., Ren Mei, E. & Saito, Y. 1987. Man's influence on the erosion and transport of sediment by Asian Rivers: the Yellow River (Huanghe) example. *Journal of Geology,* 95 (6),751-762.

Moon, J. H., Hirose, N. & Yoon, J. H. 2009. Comparison of wind and tidal contributions to seasonal circulation of the Yellow Sea. *Journal of Geophysical Research C: Oceans,* 114 (8).

Morton, A. C. 1991. Geochemical studies of detrital heavy minerals and their application to provenance research. *In:* MORTON, A. C., TODD, S.P., HAUGHTON, P.D.W. (ed.) *Developments in sedimentary provenance studies.* Geol. Soc. Spec.31-45.

Naimie, C. E., Ann Blain, C. & Lynch, D. R. 2001. Seasonal mean circulation in the Yellow Sea - A model-generated climatology. *Continental Shelf Research,* 21 (6-7),667-695.

Nittrouer, C. A. & Wright, L. D. 1994. Transport of particles across continental shelves. *Reviews of Geophysics,* 32 (1),85-113.

Nohara, M., Yokota, S. & Saito, Y. Year. Sr-Nd isotopic and trace elements constrained on the origin of the sediments in the Yellow and East China Seas. *In:* SAITO, Y., IKEHARA, K., KATAYAMA,H., ed. Proceedings of an

International Workshop on Sedi-ment Transport and Storage in Coastal Sea-Ocean System, 1999 Tsukuba, Japan. 123-127.

Ozdemir, C. E., Hsu, T. J. & Balachandar, S. 2010. Simulation of fine sediment transport in oscillatory boundary layer. *Journal of Hydro-Environment Research,* 3 (4),247-259.

Pang, C. G. & Hu, D. X. 2002. Upwelling and sedimentation dynamics III: Coincidence of upwelling areas with mud patches in north hemisphere shelf seas. *Chinese Journal of Oceanology and Limnology,* 20 (2),101-106.

Pang, C. G., Liang, J., Hu, D., Wang, F., Chen, Y., Bai, H. & Bai, X. 2004. Surface circulation patterns observed by drifters in the Yellow Sea in summer of 2001, 2002 and 2003. *Chinese Journal of Oceanology and Limnology,* 22 (3),209-216.

Parchure, T. & Mehta, A. 1985. Erosion of Soft Cohesive Sediment Deposits. *Journal of Hydraulic Engineering,* 111 (10),1308-1326.

Park, S. & Chu, P. C. 2006. Thermal and haline fronts in the Yellow/East China Seas: Surface and subsurface seasonality comparison. *Journal of Oceanography,* 62 (5),617-638.

Park, S. C., Lee, H. H., Han, H. S., Lee, G. H., Kim, D. C. & Yoo, D. G. 2000. Evolution of late Quaternary mud deposits and recent sediment budget in the southeastern Yellow Sea. *Marine Geology,* 170 (3-4),271-288.

Park, Y. A. & Khim, B. K. 1992. Origin and dispersal of recent clay minerals in the Yellow Sea. *Marine Geology,* 104 (1–4),205-213.

Pawlowicz, R., Beardsley, B. & Lentz, S. 2002. Classical tidal harmonic analysis including error estimates in MATLAB using T_TIDE. *Computers & Geosciences,* 28 (8),929-937.

Piotrowicz, S. R., Hogan, C. A., Shore, R. A. & Pszenny, A. a. P. 1981. Variability in the distribution of weak acid leachable Cd, Cr, Cu, Fe, Ni, Pb, and Zn in the sediments of the georges bank/gulf of maine region. *Environmental Science and Technology,* 15 (9),1067-1072.

Revel, M., Cremer, M., Grousset, F. E. & Labeyrie, L. 1996. Grain-size Sr-Nd isotopes as of paleo-bottom current strength, Northeast Atlantic Ocean. *Marine Geology,* 131 (3-4),233-249.

Ribbe, J. & Holloway, P. E. 2001. A model of suspended sediment transport by internal tides. *Continental Shelf Research,* 21 (4),395-422.

Risien, C. M. & Chelton, D. B. 2008. A Global Climatology of Surface Wind and Wind Stress Fields from Eight Years of QuikSCAT Scatterometer Data. *Journal of Physical Oceanography,* 38 (11),2379-2413.

Rollinson, H. & Data, U. G. 1993. *Evaluation, Presentation, Interpretation,* New York, Longman.

Saito, Y., Yang, Z. & Hori, K. 2001. The Huanghe (Yellow River) and Changjiang (Yangtze River) deltas: a review on their characteristics, evolution and sediment discharge during the Holocene. *Geomorphology,* 41 (2–3),219-231.

Scully, M. E. & Friedrichs, C. T. 2003. The influence of asymmetries in overlying stratification on near-bed turbulence and sediment suspension in a partially mixed estuary. *Ocean Dynamics,* 53 (3),208-219.

Seelig, W. N. Year. Effects of breakwaters on waves: laboratory tests of wave transmission by overtopping. *In:* Proc. Conf. Coastal Structures, 1979. 941-961.

Seifert, T., Fennel, W. & Kuhrts, C. 2009. High resolution model studies of transport of sedimentary material in the south-western Baltic. *Journal of Marine Systems,* 75 (3-4),382-396.

Shi, X., Chen, C., Liu, Y., Ren, H. & Wang, H. 2002. Trend analysis of sediment grain size and sedimentary process in the central South Yellow Sea. *Chinese Science Bulletin,* 47 (14),1202-1207.

Smith, J. D. & Mclean, S. R. 1977. SPATIALLY AVERAGED FLOW OVER A WAVY SURFACE. *J Geophys Res,* 82 (12),1735-1746.

Snyder, R. L., Dobson, F. W., Elliott, J. A. & Long, R. B. 1981. Array measurements of atmospheric pressure fluctuations above surface gravity waves. *Journal of Fluid Mechanics,* 102,1-59.

Su, J. L. 1998. Circulation Dynamics of the China Seas North of 18℃N. *In:* ROBINSON, A. R. & BRINK, K. (eds.) *The Sea. The Global Coastal Ocean: Regional Studies and Syntheses.* John Wiley & Sons. Inc.,pp 483-506.

Takahashi, S. & Yanagi, T. 1995. A numerical study on the formation of circulations in the Yellow Sea during summer. *La Mer,* 33 (3),135-147.

Tang, Y., Zou, E. & Lie, H. 2000. Some features of circulation in the southern Huanghai Sea. *Acta Oceanol. Sin.,* 22 (1),1-16.

Taylor, S. R. & Mclennan, S. M. 1985. *The continental crust: its composition and evolution,* Oxford, Blackwell.

Teixeira, M., Warn-Varnas, A., Apel, J. & Hawkins, J. 2006. Analytical and observational studies of internal solitary waves in the Yellow Sea. *Journal of Coastal Research,* 22 (6),1403-1416.

Tsai, C. H. & Lick, W. 1988. Resuspension of sediments from Long Island Sound (U.S.A.). *Water Science and Technology,* 20 (6-7),155-164.

Wang, H., Yang, Z., Saito, Y., Liu, J. P., Sun, X. & Wang, Y. 2007a. Stepwise decreases of the Huanghe (Yellow River) sediment load (1950–2005): Impacts of climate change and human activities. *Global and Planetary Change,* 57 (3-4),331-354.

Wang, H. X., Zhang, X. J., Lan, X. H., Zhang, Z. X., Lin, Z. H. & Zhao, G. T. 2007b. Geochemistry Characteristics of Sediment and Provenance Relations of Sediments in Core NT1 of the South Yellow Sea. *Journal of China University of Geosciences,* 18 (4),287-298.

Wang, J. T. 1990. REE GEOCHEMISTRY OF SURFICIAL SEDIMENTS FROM THE YELLOW SEA OF CHINA. *Geochimica,* 10,44-53.

Wang, X., Chen, Y., Lei, J., Wu, M. & Zhao, Y. 1983. REE geochemistry of sea-floor sediments of the continental shelf of the East China Sea. *Geochemistry,* 2 (4),318-327.

Wang, Y., Li, G., Zhang, W. & Dong, P. 2013. Sedimentary environment and formation mechanism of the mud deposit in the central South Yellow Sea during the past 40k years. *Marine Geology,* (in press).

Ward, L. G., Zaprowski, B. J., Trainer, K. D. & Davis, P. T. 2008. Stratigraphy, pollen history and geochronology of tidal marshes in a Gulf of Maine estuarine system: Climatic and relative sea level impacts. *Marine Geology,* 256 (1-4),1-17.

Wei, J., Shi, X., Li, G. & Liang, R. 2003. Clay mineral distributions in the southern Yellow Sea and their significance. *Chinese Science Bulletin,* 48 (1),7-11.

Whitham, G. B. 1974. *Linear and nonlinear waves,* New York, Wiley.

Wright, L. D. & Nittrouer, C. A. 1995. Dispersal of river sediments in coastal seas: Six contrasting cases. *Estuaries,* 18 (3),494-508.

Xia, C., Qiao, F., Yang, Y., Ma, J. & Yuan, Y. 2006. Three-dimensional structure of the summertime circulation in the Yellow Sea from a wave-tide-circulation coupled model. *Journal of Geophysical Research,* 111 (C11).

Xia, C., Qiao, F., Zhang, M., Yang, Y. & Yuan, Y. 2004. Simulation of double cold cores of the 35°N section in the Yellow Sea with a wave-tide-circulation coupled model. *Chinese Journal of Oceanology and Limnology,* 22 (3),292-298.

Xiang, R., Yang, Z., Saito, Y., Fan, D., Chen, M., Guo, Z. & Chen, Z. 2008. Paleoenvironmental changes during the last 8400 years in the southern Yellow Sea: Benthic foraminiferal and stable isotopic evidence. *Marine Micropaleontology,* 67 (1-2),104-119.

Xing, F., Wang, Y. P. & Wang, H. V. 2011. Tidal hydrodynamics and fine-grained sediment transport on the radial sand ridge system in the southern Yellow Sea. *Marine Geology,* 291-294,192-210.

Xing, L., Zhao, M., Zhang, H., Zhao, X., Zhao, X., Yang, Z. & Liu, C. 2012. Biomarker evidence for paleoenvironmental changes in the southern Yellow Sea over the last 8200 years. *Chinese Journal of Oceanology and Limnology,* 30 (1),1-11.

Xu, D., Yuan, Y. & Liu, Y. 2003. The baroclinic circulation structure of Yellow Sea Cold Water Mass. *Science in China, Series D: Earth Sciences,* 46 (2),117-126.

Xu, K., Milliman, J. D., Li, A., Paul Liu, J., Kao, S.-J. & Wan, S. 2009. Yangtze- and Taiwan-derived sediments on the inner shelf of East China Sea. *Continental Shelf Research,* 29 (18),2240-2256.

Yanagi, T. & Inoue, K. 1994. Tide and tidal current in the Yellow/East China Seas. *La Mer,* 32 (3),153-165.

Yanagi, T. & Inoue, K. I. 1995. A numerical experiment on the sedimentation processes in the Yellow Sea and the East China Sea. *Journal of Oceanography,* 51 (5),537-552.

Yanagi, T. & Takahashi, S. 1993. Seasonal variation of circulations in the East China Sea and the Yellow Sea. *Journal of Oceanography,* 49 (5),503-520.

Yang, S. & Youn, J. S. 2007. Geochemical compositions and provenance discrimination of the central south Yellow Sea sediments. *Marine Geology,* 243 (1-4),229-241.

Yang, S. Y., Jiang, S. Y., Ling, H. F., Xia, X. P., Sun, M. & Wang, D. J. 2007. Sr-Nd isotopic compositions of the Changjiang sediments: Implications for tracing sediment sources. *Science in China, Series D: Earth Sciences,* 50 (10),1556-1565.

Yang, S. Y., Jung, H. S., Choi, M. S. & Li, C. X. 2002. The rare earth element compositions of the Changjiang (Yangtze) and Huanghe (Yellow) river sediments. *Earth and Planetary Science Letters,* 201 (2),407-419.

Yang, S. Y., Jung, H. S., Lim, D. I. & Li, C. X. 2003. A review on the provenance discrimination of sediments in the Yellow Sea. *Earth-Science Reviews,* 63 (1-2),93-120.

Yang, Y., Qiao, F., Xia, C., Ma, J. & Yuan, Y. 2004. Wave-induced mixing in the Yellow Sea. *Chinese Journal of Oceanology and Limnology,* 22 (3),322-326.

Yang, Z. G. 1993. The sedmentary sequence and palaeogeographic changes of the South Yellow Sea since the Olduvai Subchron. *Acta Geologica Sinica* 47 (4),357-366.

Yang, Z. S. & Liu, J. P. 2007. A unique Yellow River-derived distal subaqueous delta in the Yellow Sea. *Marine Geology,* 240 (1-4),169-176.

Yuan, D. & Hsueh, Y. 2010. Dynamics of the cross-shelf circulation in the Yellow and East China Seas in winter. *Deep-Sea Research Part II: Topical Studies in Oceanography,* 57 (19-20),1745-1761.

Yuan, D., Zhu, J., Li, C. & Hu, D. 2008. Cross-shelf circulation in the Yellow and East China Seas indicated by MODIS satellite observations. *Journal of Marine Systems,* 70 (1-2),134-149.

Yuan, Y. C., Su, J. L. & Zhao, J. S. 1982. A single layer model of the continental shelf circulation on the northwest shelf of the East China Sea. *La Mer,* 20,131-135.

Zhao, Y., Qin, Z., Li, F. & Chen, Y. 1990. On the source and genesis of the mud in the central area of the South Yellow Sea. *Chinese Journal of Oceanology and Limnology,* 8 (1),66-73.

Zhao, Y. Y., Jiang, R. H. & Yan, M. C. 1995. Abundance of chemical elements in continental shelf sediment of China. *Geo-Marine Letters,* 15 (2),71-76.

Zhao, Y. Y., Park, Y. A., Qin, Y. S., Choi, J. Y., Gao, S., Li, F. Y., Cheng, P. & Jiang, R. H. 2001. Material source for the Eastern Yellow Sea Mud: evidence of mineralogy and geochemistry from China-Korea Jonit investigations. *The Yellow Sea,* 7 (1),22-26.

Zhu, Y. & Chang, R. 2000. Preliminary Study of the Dynamic Origin of the Distribution Pattern of Bottom Sediments on the Continental Shelves of the Bohai Sea, Yellow Sea and East China Sea. *Estuarine, Coastal and Shelf Science,* 51 (5),663-680.

Zhuang, L. H., Chang, F. M., Li, T. G. & Yan, J. 2002. Foraminiferal Faunas and Holocene sedimentation rates of core EY02-2 in the south Yellow Sea. *Marine Geology and Quaternary Geology,* 22 (4),7-14.